Luís Miguel do Rosário Irio

Mestre em Engenharia Electrotécnica e de Computadores

Interference Characterization in Multiple Access Wireless Networks

Dissertação para obtenção do Grau de Doutor em

Engenharia Electrotécnica e de Computadores

Orientador: Rodolfo Alexandre Duarte Oliveira,
Prof. Auxiliar com Agregação,
Universidade Nova de Lisboa

Júri

Presidente: Paulo da Costa Luís da Fonseca Pinto
Arguentes: Nuno Miguel Gonçalves Borges de Carvalho
Marco Alexandre Cravo Gomes
Vogais: Francisco António Bucho Cercas
Luís Filipe Lourenço Bernardo
Rodolfo Alexandre Duarte Oliveira

FACULDADE DE
CIÊNCIAS E TECNOLOGIA
UNIVERSIDADE NOVA DE LISBOA

Dezembro, 2019

Interference Characterization in Multiple Access Wireless Networks

To my admirable wife, and my dear daughter.

ACKNOWLEDGEMENTS

Firstly, I would like to express my sincere gratitude to my supervisor and mentor Professor Rodolfo Oliveira. Your contagious passion about science inspired me throughout my young research career. I have learned a lot from you. Thank you for your guidance, continuous support and motivation. I am forever thankful for believing me and by giving me the opportunity to interact with prestigious scientists.

Recognizing the help of a great scientist, a special word goes to Daniel Benevides da Costa, from whom I have learned a lot since the last year. Daniel has shown me the fundamental, what really matters, and I am very grateful for that.

I would also like to thank Professor Luis Bernardo, Professor Rui Dinis and Professor Paulo Pinto for all the scientific contributions and help.

An acknowledgement is also due to the Faculdade de Ciências e Tecnologia da Universidade Nova de Lisboa, and research centers Instituto de Telecomunicações (IT) and Centre of Technology and Systems (CTS-UNINOVA) for the institutional support.

I also acknowledge the indispensable financial support provided by Fundação para a Ciência e Tecnologia (FCT) under the research grant SFRH/BD/108525/2015 and research projects Opportunistic-CR (PTDC/EEA-TEL/115981/2009), ADIN (PTDC/EEI-TEL/2990/2012), MANY2COMWIN (EXPL/EEI-TEL/0969/2013), CoSHARE (LISBOA-01-0145-FEDER-0307095 - PTDC/EEI-TEL/30709/2017), and InfoCent-IoT (POCI-01-0145-FEDER-030433).

I would also like to say thank you to my dear lab colleagues: António Furtado, Slaviša Tomić, Filipe Ribeiro, Miguel Luís, João Guerreiro, David Borges, Amineh Mazandarani, and Akashkumar Rajaram.

I would like to express my deepest gratitude to my parents for their love and for the huge efforts conducted in order to provide me the best education. A special word to my little sister. Your love was essential during many periods. My huge gratitude words also go to all my family.

Lastly, I would like to thank to Erica, my wife, for her love and indubitable friendship. A special word for her parents and brother.

This work is dedicated to my beloved wife, Erica, and my lovely daughter, Leonor. They gave me the indispensable strength, in the form of love, that unconditionally supported me during this journey. Thank you for everything.

ABSTRACT

Contrarily to the point to point wireless link approach adopted in several wireless networks, where a dedicated channel is usually supporting an exclusive-use wireless link, in the last years several wireless communication systems have followed a different approach. In the so called "multiple access wireless networks", multiple transmitters share the same communication channel in a simultaneous way, supporting a shared-use of the wireless link. The deployment of multiple access networks has also originated the emergence of various communication networks operating in the same geographical area and spectrum space, which is usually referred to as wireless coexistence. As a consequence of the presence of multiple networks with different technologies that share the same spectral bands, robust methods of interference management are needed. At the same time, the adoption of in-band Full-duplex (IBFDX) communication schemes, in which a given node transmit and receive simultaneously over the same frequency band, is seen as a disruptive topic in multiple access networks, capable of doubling the network's capacity.

Motivated by the importance of the interference in multiple access networks, this thesis addresses new approaches to characterize the interference in multiple access networks. A special focus is given to the assumption of mobility for the multiple transmitters. The problem of coexistence interference caused by multiple networks operating in the same band is also considered. Moreover, given the importance of the residual self-interference (SI) in practical IBFDX multiple access networks, we study the distribution of the residual SI power in a wireless IBFDX communication system. In addition, different applications of the proposed interference models are presented, including the definition of a new sensing capacity metric for cognitive radio networks, the performance evaluation of wireless-powered coexisting networks, the computation of an optimal carrier-sensing range in coexisting CSMA networks, and the estimation of residual self-interference in IBFDX communication systems.

Keywords: Interference Modeling, Performance Analysis, Wireless Mobile Networks.

RESUMO

Contrariamente à abordagem de uma ligação ponto a ponto em redes sem fios, em que a ligação faz utilização exclusiva de um canal dedicado, nos últimos anos vários sistemas de comunicação sem fios adotaram uma abordagem diferente. Nas denominadas “redes sem fios de acesso múltiplo”, vários transmissores partilham o mesmo canal de comunicação, partilhando a mesma ligação sem fios com outros nós transmissores. O desenvolvimento de várias redes de acesso múltiplo também permitiu o surgimento de várias redes que operam na mesma área geográfica e na mesma banda do espetro, geralmente denominada por coexistência sem fios. Como consequência da presença de várias redes com diferentes tecnologias que partilham as mesmas bandas, são necessários métodos robustos de gestão de interferência. Ao mesmo tempo, a adoção de esquemas de comunicação *in-band Full-duplex* (IBFDX), onde um determinado nó transmite e recebe simultaneamente na mesma frequência, é visto como um tópico disruptivo em redes de acesso múltiplo, capaz de duplicar a capacidade da rede.

Motivada pela importância da interferência em redes de acesso múltiplo, esta tese aborda novas técnicas de modelação para caracterizar a interferência em redes de acesso múltiplo. É dada especial atenção à interferência causada por vários transmissores móveis. O problema da interferência coexistente, causada por várias redes operando na mesma banda também é considerado. Além disso, dada a importância da auto-interferência residual em cenários práticos de acesso múltiplo IBFDX, é ainda estudada a distribuição da sua potência. Por fim, diferentes aplicações são propostas para os modelos desenvolvidos na caracterização da interferência, incluindo a definição de uma nova métrica para a capacidade de deteção em redes de rádio cognitivos, a avaliação do desempenho de redes coexistentes sem fios, o cálculo do valor ótimo para o *carrier-sensing range* em redes coexistentes, e ainda a estimação da auto-interferência residual em sistemas IBFDX.

Palavras-chave: Modelação de Interferência, Avaliação de Desempenho, Redes Móveis Sem fios.

CONTENTS

LIST OF FIGURES

LIST OF TABLES

LIST OF SYMBOLS

General Symbols

$\approx$	Approximately equal to
$\cos(x)$	Cosine of the angle x
$\delta(.)$	Dirac delta function
$\Gamma(\cdot)$	Gamma function
$\Gamma(p,x)$	Incomplete Gamma function
$\mathfrak{Im}\{z\}$	Imaginary part of the complex number z
$\mathcal{N}(\mu,\sigma^2)$	Normal distribution with mean μ and variance σ^2
$\mathfrak{Re}\{z\}$	Real part of the complex number z
$\sim$	Distributed according to
$\sin(x)$	Sine of the angle x
$\tan(x)$	Tangent of the angle x
$U(a,b)$	Continuous Uniform distribution on the interval $[a, b]$
$\mathrm{Exp}(\lambda)$	Exponential distribution with rate parameter λ
$\mathrm{E}[X]$	Expectation with respect to the random variable X
$\mathrm{Gamma}(k,\theta)$	Gamma distribution with a shape k and a scale θ
$\log_b(x)$	Base-b logarithm of x; when b is omitted it denotes the natural algorithm
$\mathrm{Nakagami}(m,\Omega)$	Nakagami distribution with a shape m and a spread Ω
$\mathrm{P}[X]$	Probability of X
$\mathrm{Var}[X]$	Variance with respect to the random variable X
${}_2\mathrm{F}_1$	Gauss Hypergeometric function

$f_X(\cdot)$	Probability density function of the random variable X
j	Imaginary unit
$K_y(\cdot)$	Modified Bessel function of the second kind with order y
$M_X(s)$	Moment-generating function of the random variable X
x^*	Optimal value of x

General PHY-layer Symbols (when η is omitted only a single network is considered)

(x_{N_c}, y_{N_c})	Cartesian coordinates of the position of the node N_c
$\lambda_{\eta,l}$	Node's spatial density of the annulus l of the network η
λ_η	Node's spatial density of the network η
τ_η	Individual transmission probability adopted by the transmitters of the network η
υ	Number of different coexisting networks
Υ_η	Network η, where $\eta = 1, ..., \upsilon$
$\wp$	Path-loss coefficient
$I_{\eta,l,i}$	Interference power caused by node i located in the annulus l
$I_{\eta,l}$	Interference power caused by transmitters located in the annulus l
I_η	Aggregate interference caused by network Υ_η
I_{agg}	Aggregate interference
n_η	Number of transmitters of the network η
N_c	Receiver Node
P_{Tx_η}	Transmitted power
X_{max}	Length of the network area
Y_{max}	Width of the network area

Random Waypoint Mobility Model

$\mathrm{E}[S]$	Expected distance traveled between two random points
$\mathrm{E}[V]$	Average velocity of the nodes
$\mathrm{E}[V_{wp}]$	Average velocity of the nodes without considering pause
T_p	Pause time of the mobile nodes

V_{max}	Maximum velocity of the nodes
V_{min}	Minimum velocity of the nodes

Spatial Circular Model (when η is omitted only a single network is considered)

ρ	Width of an annulus
A_{η}	Area of the circular region
$A_{\eta,l}$	Area of the l-th annulus
L_{η}	Total number of annuli
$R_{\eta,l+1}$	Radius of the outer l-th annulus circle
$R_{\eta,l}$	Radius of the inner l-th annulus circle

Wireless-powered Communications

c^{*}	Optimal time allocation ratio
γ_0	Signal-to-noise ratio decision threshold
γ_d	Signal-to-noise ratio
$\mathscr{R}$	Data communication rate
$\sigma_{n_d}^2$	Variance of the zero-mean Additive White Gaussian Noise
ς	Energy conversion efficiency
c	Time splitting factor
d_1	Distance between the nodes N_{Tx} and N_{Rx}
E_h	Energy harvested
h_1	Channel coefficient from the transmitter N_{Tx} to the receiver N_{Rx}
n_d	Noise signal at the receiver
N_{Rx}	Receiver node
N_{Tx}	Harvester/transmitter node
$P_{N_{Tx}}$	Transmission power for information transfer
P_{out}	Outage probability of the transmission
R_{τ}	Throughput of the communication channel
T	Total duration of the time-switching cycle

x_c	Normalized information signal transmitted by N_{Tx}
$y_{N_{Rx}}$	Signal received by the node N_{Rx}

Residual Self-Interference Model

$(1-\epsilon)$	Self-interference Channel's gain error
Δ_T	Sample period
$\hat{\mathbf{h}}_{si}(t)$	Estimate of the self-interference channel
$\mathbf{h}_{si}(t)$	Impulse response of the self-interference channel
ω_c	Angular carrier frequency
$\phi(t)$	Oscillator's phase-noise
σ_x^2	Variance of the self-interference signal
σ_{pn}^2	Variance of the oscillator's phase noise
τ_c	Estimated delay of the self-interference channel
Ξ	Phase cancellation error
f_c	Carrier frequency
h_c	Estimated gain of the self-interference channel
K_{dB}	Ratio between the signal power received in the direct path and the power from the other paths
$P_{y_{r_{si}}}$	Residual self-interference power
$x_{si}(t)$	Self-interference signal
$y_{r_{si}}(t)$	Residual/uncancelled self-interference signal

Cognitive Radio Network Model

γ	Decision threshold
ε	Sensing efficiency
ζ	Spectral efficiency of the band
A_{SR}	Area of the SU's sensing region
k	Number of PUs located inside the SU's sensing region
n	Total number of PUs

$n-k$	Number of PUs located outside the SU's sensing region
P_I	Probability of a PU being located within the sensing region
$P_{I_{off}}$	Probability of not occurring any activity caused by the PUs
$P_{O_{SFA}}$	Probability of not occurring the SFA effect
P_{off}	Probability of the communication channel being available
W	Channel's bandwidth

Carrier Sense Multiple Access Network Model

γ_{cs}	Carrier-sensing threshold
C_{cs}	Carrier-sensing metric
P_{acc}	Medium access probability
R_{cs}	Carrier-sensing range
${R^*}_{cs}$	Optimal carrier-sensing range

ACRONYMS

AC Analog Cancellation.

ACI Adjacent Channel Interference.

ADC Analog-to-Digital Converter.

AI Antenna Isolation.

AWGN Additive White Gaussian Noise.

BPP Binomial Point Process.

CCI Co-Channel Interference.

CDF Cumulative Distribution Function.

CDMA Code Division Multiple Access.

CF Characteristic Function.

CLT Central Limit Theorem.

CMOS Complementary metal-oxide-semiconductor.

CRN Cognitive Radio Network.

CSMA Carrier Sense Multiple Access.

DC Digital Cancellation.

DL Downlink.

ENOB Effective number of bits.

FFT Fast Fourier Transform.

GEV Generalized Extreme Value.

IBFDX In-Band Full-Duplex.

IPP Inhomogeneous Poisson Process.

IQ In-Phase/Quadrature.

LOS Line of Sight.

LT Laplace Transform.

MAC Medium Access Control.

MAI Multiple Access Interference.

MGF Moment Generating Function.

MIMO Multiple-input multiple-output.

MLE Maximum Likelihood Estimation.

MXC Mixed-signal Cancellation.

OFDM Orthogonal Frequency Division Modulation.

PDF Probability Density Function.

PHY Physical-(layer).

PMF Probability Mass Function.

PN Phase Noise.

PPP Poisson Point Process.

PU Primary User.

PWM Probability Weighted Moments.

RC Resistor–capacitor.

RD Random Direction.

RF Radio Frequency.

RV Random Variable.

RW Random Walk.

RWP Random Waypoint.

RX Receiver.

SC Sensing Capacity.

SCM Spatial Circular Model.

SFA Spatial False Alarm.

SI Self-Interference.

SIC Self-Interference Cancellation.

SNR Signal-to-Noise Ratio.

SS Spectrum Sensing.

SU Secondary User.

TX Transmitter.

UL Uplink.

WPC Wireless-powered Communications.

CHAPTER 1

INTRODUCTION

1.1 Motivation and Scope

In recent years, rapid advances in wireless technology coupled with advances in chip technology have increased the number of possible wireless applications, devices, and services. Nowadays, wireless communications are a well-established technology that has been adopted in a plethora of applications and scenarios, and plays an increasingly important role in our lives.

A wireless network is typically composed of multiple transmitters and receivers, spatially scattered over some geographical region, in which each transmitter-receiver pair communicates by establishing a wireless link, whose performance is constrained by propagation effects (e.g., path loss, fading or shadowing).

Contrarily to the point to point wireless link approach adopted in several wireless networks, where a dedicated channel is usually supporting an exclusive-use wireless link, in the last years several wireless communication systems have followed a different approach. In the so called "multiple access wireless networks", multiple transmitters share the same communication channel in a simultaneous way, supporting a shared-use of the wireless link. There are currently several protocols developed by different standards organizations that can be categorized as multiple access wireless networks. These include but not limited to Wi-Fi/IEEE 802.11, LoRa, and IEEE 802.15.4. The non-exclusive use of the channel by multiple nodes is usually implemented through multiple access techniques, including random channel access in the time domain. Consequently, multiple transmissions may occur at the same time over the same frequency band, which effectively impacts on the receiver's performance.

The deployment of multiple access networks has also originated the deployment of various communication networks operating in the same geographical area and spectrum space, which is usually referred to as wireless coexistence. In wireless coexisting networks, the spectrum access mechanisms should be designed to ensure interference management and medium access control mechanisms (e.g. ALOHA and Carrier Sense Multiple Access (CSMA)) that limit the interference to the users of the coexisting networks. Thus, interference is a crucial topic in both multiple access wireless networks and coexisting networks, since the networks' performance is limited by the competition of multiple transmitters/interferers [HG09].

The modeling of the interference is an important action to characterize the networks' performance, but can also be used in the analysis and design of the communication systems, the development of interference mitigation techniques, RF planning, and the control of electromagnetic emissions, among many others [Win+09]. Consequently, the interest in characterizing the distribution of the aggregate interference in large multiple access wireless networks has increased with the emergence of different types of wireless networks. Examples of these networks include wireless sensor networks, ad hoc networks, and cognitive radio networks. Despite the increasing interest on the analysis of these networks in recent years, the characterization of the interference in such multiple access networks has not been studied extensively. The primary reason for this is the high complexity associated to the modeling task. Particularly, in a network where nodes are randomly distributed and randomly transmitting in the same channel, there might not exist a closed-form expression for the distribution of the interference. Owing to the mathematical complexity involved in the interference modeling task, analytical results on the distribution of the interference exist only for a few particular classes of networks.

Motivated by the importance of the interference in multiple access networks, this thesis addresses new approaches to characterize the multiple access interference. As the interference is determined by the location of the network nodes, the key challenge is to characterize the relationship between the network topology and the interference. Recognizing that the coexistence increases the interference modeling complexity, we are also motivated to study the intrinsic stochastic features of each coexisting network in the interference analysis, including but not limited to different spatial distribution of the nodes, different transmission power, and different medium access patterns.

Another disruptive topic in multiple access networks is the use of in-band Full-duplex (IBFDX) communication schemes, in which a given node transmit and receive simultaneously over the same frequency band. In IBFDX systems the signal being transmitted interferes with the desired received signal at the same terminal [Dua12], which is known as self-interference (SI). When a terminal adopts IBFDX communications in a multiple access network, the capacity of the communication system can be doubled, compared to half-duplex communication systems [Dua12]. However, to simultaneously transmit and receive, a terminal must separate its own transmission from the received signal. Any residual SI will increase the receiver's noise floor, reducing the capacity of the terminal. IBFDX communications' performance is limited by the amount of SI suppression. Thus, the knowledge of the residual SI distribution is crucial to design efficient SI estimation methods, that allow the cancellation of the residual SI in a proper way.

Knowing the importance of the SI characterization in practical IBFDX multiple access networks, this thesis derives the distribution of the residual SI power in a wireless IBFDX communication system, focusing on the channel estimation errors, considering different SI channels, and taking into account low and high channel gain dynamics.

In a nutshell, in multiple access networks or in IBFDX communication schemes, the interference is intrinsically harmful, because it decreases the performance of the wireless communication system. Consequently, the understanding of the stochastic properties of the interference is crucial to improve the performance of such wireless systems and is the main motivation for the the work presented in this thesis.

1.2 Research Question and Hypothesis

This section states the research question and its respective hypothesis. The research question is stated as follows:

Considering a distributed network, where nodes access to a given channel according to a local policy, i.e. without being controlled by a central node, and admitting nodes' mobility according to a known mobility model, how can we characterize the aggregate interference caused to a receiver due to the multiple transmissions of the mobile nodes or due to the adoption of IBFDX communications? Furthermore, how the interference characterization can be used in real-time to provide accurate estimates of the interference power and to solve different analytical problems in multiple access networks?

The research question can be addressed by the following hypothesis:

The characterization of the aggregate interference can be achieved through a specific modeling methodology that combines the stochastic properties of the node's mobility with the stochastic description of the propagation effects influencing each node's transmission. Moreover, departing from the proposed interference models, it is expected to derive low computational estimation methods able to accurately estimate the distribution of the interference with the smallest amount of information.

1.3 Objectives

The proposed thesis aims to develop novel interference modeling methodologies capable of supporting the performance analysis of challenging topics in advanced wireless networks, such as the operation in mobile scenarios, the adoption of IBFDX communications, and the coexistence operation of multiple networks. The goal is to develop highly accurate models requiring low computational power.

The main objectives to be achieved in this thesis are summarized as follows:

- Develop a model to characterize the aggregate interference caused to a receiver in mobility scenarios, where the transmitter nodes of a multiple access network are mobile;
- Propose a scheme to estimate interference in mobile scenarios;

- Evaluate the accuracy of the proposed models and estimation schemes in mobile scenarios;
- Derive expressions for the distribution of the residual SI power for low and high channel gain dynamics;
- Evaluate the impact of the fading channel on the distribution of the residual SI power;
- Study the phase noise (PN) effect on the distribution of the residual SI power;
- Characterize the aggregate interference caused to a fixed receiver by multiple nodes belonging to different coexisting networks;
- Demonstrate different applications where the interference characterization can be employed;
- Disseminate the results in relevant scientific conferences and journals.

1.4 Contributions

The major contribution of this thesis is the design of novel non-Gaussian modeling approaches for the aggregate interference in multi-access static and mobile wireless networks, including the SI when IBFDX communications are adopted.

Departing from the spatial distribution of the nodes moving according to a random mobility model, the expectation of the aggregate interference power was characterized in [Iri+15b] by considering only the path loss effect. The Moment Generating Function (MGF) of the aggregate interference received by a fixed central node when the interfering nodes move according to a random mobility model was also derived, providing a theoretical approximation for the aggregate interference distribution only considering the path loss effect [Iri+15a]. Assuming a time-varying wireless channel due to slow and fast fading, and considering the dynamic path loss due to the mobility of the nodes, [IO15a] presented two different methodologies to estimate the interference, based on a maximum likelihood estimator (MLE) and a probability weighted moments (PWM) estimator. The simulation results confirmed that the distribution of the aggregated interference may be accurately approximated by a generalized extreme value (GEV) distribution [IO15a; Iri+16; IO16]. The MGF of the aggregate interference was also derived considering shadowing and fast fading propagation effects [Iri+18b], presenting a theoretical approximation for the aggregate distribution at any location of the simulation area (instead of the center of the simulation only). The contributions enumerated so far are presented in Chapter 3.

Considering the possibility of adopting IBFDX communications, we worked to understand the stochastic properties of the residual SI power, and a preparatory study related with the identification of hypothetical distributions of the residual SI power was presented in [IO18]. Using the simulated data, we observed that known distributions are not capable of approximating the distribution of the residual SI in an accurate way [IO18]. On the other hand, we have analyzed the impact of the up- and down-conversion oscillator's PN on the residual SI [Iri+18a]. To characterize the residual SI in a theoretical way, we have derived closed form expressions for the approximation of the residual SI power distribution, when Rician and Rayleigh fading SI channels are considered

[IO19a]. Moreover, the distribution of the residual SI power is derived for low and high channel gain dynamics, by considering a time-invariant and a time-variant channel, respectively [IO19a]. The contributions related with IBFDX communications are presented in Chapter 4.

Given the multi-access nature of the interferers considered in the proposed models, we use and extend the aggregate interference models to study the coexistent interference, when two or more different networks operate in the same spectrum. Considering the scenario where two unlicensed networks cause interference to a primary network, we show that the distribution of the aggregate interference caused to a licensed user of the primary network is characterized by an α-μ distribution [Iri+19b]. Extending this contribution, we propose two different methods to characterize the aggregate interference caused to a licensed user. The contributions described are presented in Chapter 5.

Having characterized the interference in Random Waypoint (RWP) networks, the residual SI in IBFDX, and the interference caused by multiple coexisting networks, we move on to different application scenarios where the interference models can be employed. Thus, using the knowledge of aggregate interference distribution in mobility networks, we have defined a new sensing capacity (SC) metric for cognitive radio networks (CRNs) with multiple mobile primary users (PUs) [IO15b; IO17]. The second application investigated the performance of wireless-powered communications (WPC) when the energy is harvested from multiple static and/or mobile wireless coexisting networks. Benefiting from the derivation of coexistence interference, the distribution of the harvested energy from multiple energy sources belonging to different coexisting networks was studied. Admitting that the harvester node acts as a transmitter after the energy harvesting period, we derived the outage probability and studied the throughput achieved by the harvester node, identifying the optimal energy harvesting time allocation having into account the mobility of the mobile networks. The third application derived a method to compute the optimal carrier-sensing range in a CSMA network. To investigate the optimal carrier-sensing range we have defined an utility function that takes into account the medium access probability of the node, and the carrier-sensing range. The optimal carrier-sensing range is identified for two different scenarios, considering the cases when the coexisting networks are spatially overlapped or non-overlapped. The fourth application derived a method to estimate the residual SI power in a IBFDX system. Considering the case when the channel gain is time-varying, admitting a Rician fading SI channel, we derive a estimation method for the distribution of the residual SI with a set of samples. These contributions are presented in Chapter 6.

The list of publications during the PhD period are as follows:

Journal Papers:

[Iri+19a] L. Irio, R. Oliveira and D. B. da Costa, "**Highly Accurate Approaches for the Interference Modeling in Coexisting Wireless Networks.**", *IEEE Communications Letters*, Jun. 2019.

[IO19a] L. Irio and R. Oliveira, "**Distribution of the Residual Self-Interference Power in In-Band Full-duplex Wireless Systems.**", *IEEE Access*, Apr. 2019.

[Iri+18b] L. Irio, A. Furtado, R. Oliveira, L. Bernardo and R. Dinis, “**Interference Characterization in Random Waypoint Mobile Networks.**”, *IEEE Transactions on Wireless Communications*, Nov. 2018

[Iri+16] L. Irio, D. Oliveira and R. Oliveira, “**Interference Estimation in Wireless Mobile Random Waypoint Networks.**”, *Telfor Journal*, 2016.

[Iri+15a] L. Irio, R. Oliveira and L. Bernardo, “**Aggregate Interference in Random Waypoint Mobile Networks.**”, *IEEE Communications Letters*, Mar. 2015.

[Fur+16] A. Furtado, L. Irio, R. Oliveira, L. Bernardo and R. Dinis, “**Spectrum Sensing Performance in Cognitive Radio Networks with Multiple Primary Users.**", *IEEE Transactions on Vehicular Technology*, Feb. 2015.

Conference Papers:

[Iri+19b] L. Irio, R. Oliveira and D. B. da Costa, “**Interference Analysis for Secondary Coexistence in Licensed Networks**”, *IEEE Global Communications Conference (GLOBECOM)*, Waikoloa, United States, Dec. 2019.

[IO19b] L. Irio and R. Oliveira, “**Modeling the Interference Caused to a LoRaWAN Gateway Due to Uplink Transmissions**”, *11th International Conference on Ubiquitous and Future Networks (ICUFN)*, Zagreb, Croatia, Jul. 2019.

[IO18] L. Irio and R. Oliveira, “**On the Impact of Fading on Residual Self-Interference Power of In-Band Full-Duplex Wireless Systems**”, *14th International Wireless Communications & Mobile Computing Conference (IWCMC)*, Limassol, Cyprus, Jun. 2018.

[Iri+18a] L. Irio, R. Oliveira and LB. Oliveira, “**Characterization of the Residual Self-Interference Power in Full-Duplex Wireless Systems.**”, *IEEE International Symposium on Circuits and Systems (ISCAS 2018)*, Florence, Italy, May 2018.

[Rib+18] A. Ribeiro, L. Irio and R. Oliveira, “**The Impact of Phase-Noise on the Communication System Receivers.**”, *2018 International Young Engineers Forum (YEF-ECE)*, Caparica, Portugal, May 2018.

[IO17] L. Irio and R. Oliveira, “**Impact of Mobility in Spectrum Sensing Capacity.**”, *International Conference on Cognitive Radio Oriented Wireless Networks (CROWNCOM 2017)*, Lisbon, Portugal, Sep. 2017.

[IO16] L. Irio and R. Oliveira, “**Real-Time Estimation of the Interference in Random Waypoint Mobile Networks.**”, *Doctoral Conference on Computing, Electrical and Industrial Systems (DoCEIS 2016)*, Caparica, Portugal, Apr. 2016.

[IO15a] L. Irio and R. Oliveira, “**Interference Estimation in Wireless Mobile Random Waypoint Networks.**”, *Telecommunications Forum (Telfor 2015)*, Belgrade, Serbia, Nov. 2015.

[Iri+15b] L. Irio, A. Furtado, R. Oliveira, L. Bernardo and R. Dinis, "**Path Loss Interference in Mobile Random Waypoint Networks.**", *European Wireless (EW 2015)*, Budapest, Hungary, May 2015.

[IO15b] L. Irio and R. Oliveira, "**Sensing Capacity of Cognitive Radio Mobile Ad Hoc Networks.**", *IEEE Wireless Communications and Networking Conference (WCNC 2015)*, New Orleans, USA, Mar. 2015.

[Fur+14b] A. Furtado, M. Luís, L. Irio, R. Oliveira, R. Dinis and L. Bernardo, "**Detection of Licensed Users' Activity in a Random Access Ultra Wideband Cognitive System.**", *IEEE International Conference on Ultra-Wideband (ICUWB 2014)*, Paris, France, Sep. 2014.

[Fur+14a] A. Furtado, L. Irio, R. Oliveira, L. Bernardo and R. Dinis, "**Characterization of the Spatial False Alarm Effect in Cognitive Radio Networks.**", *International Conference on Computer Communications and Networks (ICCCN 2014)*, Shanghai, China, Aug. 2014.

[Bra+14] B. Branco, F. Ganhão, L. Irio, L. Bernardo, R. Dinis, R. Oliveira, P. Amaral and P. Pinto, "**SC-FDE Femtocell Energy Saving using IB-DFE Interference Cancellation Techniques.**", *International Conference on Telecommunications (ICT 2014)*, Lisbon, Portugal, May 2014.

1.5 Document Structure

This thesis comprises seven chapters (introduction, five core chapters and conclusion), which are organized in several sections and subsections. Figures, tables, and equations, presented throughout these chapters are numbered as $(x.y)$, where x refers to the chapter number and y to the respective order number.

The outline and the original contributions of each chapter are as follows:

- Chapter 2 provides an extensive literature review. This chapter is divided into three sections. The first section presents the current path loss models, describes the fading effects in a mobile communication channel and shows the different probability distributions to characterize the fading channel in a statistical approach. The second section starts by introducing the different types of interference occurring in a wireless system, and then describes the different methods to characterize the aggregate interference in multiple access wireless networks. Section 2.3 introduces the SI problem, presents the SI cancellation techniques, and shows how it is possible to describe the Residual SI.

- Chapter 3 characterizes the wireless interference of a mobile network, when the nodes move according to the RWP model and considering the path loss, fast fading and shadowing effect. Two different estimators are also proposed to quickly estimate the distribution of the aggregate interference power. Results from several simulations are compared with the theoretical characterization, evaluating the accuracy of the proposed approaches.

- Chapter 4 develops a theoretical analysis of the residual SI power, which represents the amount of uncanceled SI due to channel estimation errors at the analog cancellation (AC) process. Specifically, closed form expressions are derived for the approximation of the residual SI power distribution, when Rician and Rayleigh fading SI channels are considered. The distribution of the residual SI power is also derived for low and high channel gain dynamics, by considering the cases when the SI channel gain is time-invariant and time-variant. In addition, this chapter presents different simulation results to show the influence of the channel dynamics on the distribution of the SI power.
- Chapter 5 presents two different methods to characterize the aggregate interference power caused by multiple networks coexisting in the same channel. The first method, described in Section 5.4, approximates the aggregate interference by assuming that the interference caused by the transmitters located on a given annulus of the spatial region can be approximated by a Gamma distribution. The second method presented in Section 5.5, proposes a highly accurate approximation based on the $\alpha-\mu$ distribution, which holds for the entire spatial region of each coexisting network. The accuracy of both methods are assessed through simulations in Section 5.6.
- Chapter 6 shows different applications of the interference models presented in Chapters 3, 4, and 5. Section 6.1 characterizes the SC of CRNs considering multiple mobile PUs. Section 6.2 evaluates the impact of WPC when energy is harvested from multiple static and/or mobile wireless coexisting networks. Section 6.3 derives a method to compute the optimal carrier-sensing range in a CSMA network. In Section 6.4 it is presented a method to estimate the residual SI power in a IBFDX system.
- Chapter 7 presents the conclusions of this thesis as well as some directions for future work.
- Appendix A details the mathematical derivation used to support the Poisson approximation in the spatial circular model (SCM).

CHAPTER 2

LITERATURE REVIEW

This chapter presents an overview of the literature and is divided into three sections. Section 2.1 recaps the basics of path loss models, reviews the fading effects in a mobile communication channel and shows the different probability distributions that characterize the fading channel in a statistical approach. Section 2.2 introduces the different types of interference that can be experienced in a wireless system, and summarizes the main methods proposed so far to characterize the aggregate interference in multiple access wireless networks. Section 2.3 revisits the SI problem in IBFDX communication systems, presenting a brief overview of the main cancellation techniques and methods that help to model the Residual SI.

2.1 Propagation Effects

2.1.1 Path Loss Models

A signal transmitted via a radio channel is affected by path loss (signal power attenuation), which depends on the distance between transmitting and receiving radio antennas. Path loss is also influenced by terrain contours, environment (urban or rural, vegetation), propagation medium (dry or moist air), the height and location of antennas and the frequency of the signal.

We define the path loss of the channel as the ratio of transmit power to receive power,

$$P_L = \frac{P_{Tx}}{P_{Rx}}, \tag{2.1}$$

where P_{Tx} and P_{Rx} denote the transmitted and received power in Watts $[W]$, respectively.

The path loss may also be expressed in decibels (dB) as follows

$$P_L[dB] = 10\log_{10}\left(\frac{P_{Tx}}{P_{Rx}}\right). \tag{2.2}$$

Free Space Model

In the free space propagation model it is assumed that a radio wave travels in free space, with a direct line of sight (LOS) from the transmitter (TX) to the receiver (RX) without being affected by any obstacles. This scenario predicts that the received power falls off inversely proportional to the square of the distance d (in meters) between the transmit and receive antennas. Friis free space equation is given by [Rap01],

$$P_{Rx} = P_{Tx} G_{Tx} G_{Rx} \left(\frac{\lambda}{4\pi d} \right)^2, \tag{2.3}$$

where G_{Tx} is the TX antenna gain, G_{Rx} is the receiver antenna gain and λ is the wavelength in meters.

From (2.3), expressions that describe the mean path loss in linear and logarithmic scales, may easily be found as

$$P_L = \frac{1}{G_{Tx} G_{Rx}} \left(\frac{\lambda}{4\pi d} \right)^{-2}, \tag{2.4}$$

and

$$P_L[dB] = -10 \log_{10} \left[G_{Tx} G_{Rx} \left(\frac{\lambda}{4\pi d} \right)^2 \right]. \tag{2.5}$$

In (2.4) it can be seen that the mean path loss, P_L, increases with the square of the distance d. In the logarithmic domain given by (2.5), this corresponds to a 20 dB decrease in the received power P_{Rx} per decade increment of the antenna separation distance d.

Two-Ray Model

The two-ray propagation model considers a direct path and a reflected path from the surface of the earth. In this case, the received signal consists of two components: the transmitted signal propagating trough free space (LOS component) and the transmitted signal reflected off the ground (reflected component). On an ideal reflecting surface many reflections occur, but only one ray has the angle of incidence, such that the reflection is reaching the receiving antenna. For this specific case, the following expressions in the linear and logarithmic domains, respectively, are derived as [Rap01]

$$P_L = \frac{1}{G_{Tx} G_{Rx}} \left(\frac{h_{Tx} h_{Rx}}{d^2} \right)^{-2}, \tag{2.6}$$

$$P_L[dB] = -10 \log_{10} \left[G_{Tx} G_{Rx} \left(\frac{h_{Tx} h_{Rx}}{d^2} \right)^2 \right], \tag{2.7}$$

where h_{Tx} and h_{Rx} denote the height of the transmitting and receiving antennas (in meters). In (2.6) it can be seen that the mean path loss, P_L, increases with the fourth power of the antenna separation distance d.

Log-distance Model

The majority of propagation models indicate that the average received power decreases logarithmically with distance, both in outdoor or indoor radio channels. Therefore, a very common approach to find simple models for different environments is to incorporate linear regression in the logarithmic domain. The Log-distance model for a specific environment may be obtained as follows [Rap01]

$$P_L[dB] = P_L(d_0) + 10\wp\log_{10}\left(\frac{d}{d_0}\right), \tag{2.8}$$

where $\wp$ is the path loss exponent and d_0 is the close-in reference distance. The average path loss at the close-in reference distance, $P_L(d_0)$, may be obtained using the free space model (see equation (2.5)), or from field measurements at distance d_0. Typical values for d_0 in macro, micro and picocells are 1 km, 100 m and 1 m, respectively. The reference distance should always be in the far field of the antenna, to avoid near-field effects. Table 2.1 shows typical path loss exponents for different radio environments [Rap01].

Table 2.1: Path Loss Exponents for different environments [Rap01].

Environment	**Path Loss Exponent, $\wp$**
Free space	2
Urban area cellular radio	2.7 to 3.5
Shadowed urban cellular radio	3 to 5
In building LOS	1.6 to 1.8
Obstructed in building	4 to 6
Obstructed in factories	2 to 3

2.1.2 Fading

In wireless communications, the term small-scale fading, or simply fading, refers to the rapid fluctuations of the received signal power. Fading is caused by refraction, reflection, diffraction, scattering and attenuation of radio waves. Fading effects in a mobile communication channel can be classified as [Rap01]:

- Fading effects due to multipath time delay spread;
- Fading effects due to Doppler spread.

2.1.2.1 Fading effects due to multipath time delay spread

Multipath fading is the propagation phenomenon that results in radio signals reaching the receiving antenna by two or more paths. These multipath components have different amplitudes, phases, angles of arrival and time delays. Multipath propagation causes time dispersion, and consequently the time spreading provokes fading, causing the degradation of the transmission. The time spreading due to multipath may be quantified using the following parameters [Rap01]:

- Delay spread (T_m): The delay spread is a fundamental parameter in the characterization of the multipath fading, which characterizes the time between the first and the last received component.
- Coherence bandwidth (B_c): The coherence bandwidth is related to the inverse of delay spread. Within the coherence bandwidth, B_c, all frequency components of the transmitted signal are similarly affected, i.e., they experience the same attenuation and linear phase shift.

Fading due to multipath may be classified as [Rap01]:

- Flat fading: Occurs when the symbol time duration, T_s, is greater than the delay spread, T_m (i.e. $T_s > T_m$). In this case all multipath components of a transmitted symbol arrive within the symbol duration and the channel exhibits flat fading. In the frequency domain, a transmitted signal experience flat fading if the radio channel is linear over a coherence bandwidth, B_c, that is greater than the bandwidth, B_s, of the transmitted signal (i.e. $B_c > B_s$).
- Frequency selective fading: Occurs when the delay spread, T_m is greater than the symbol time duration, T_s (i.e. $T_s < T_m$). In this case the received multipath components of a symbol arrive outside the symbol duration and intersymbol interference (ISI) distortion is introduced. In the frequency domain, the bandwidth of transmitted signal (B_s) is greater than the coherence bandwidth (B_c) of the channel (i.e. $B_c < B_s$). Consequently, different frequency components of the signal experience different fading and the channel introduces frequency selective fading, i.e., the channel does not affect the signal's spectral components equally.

Figure 2.1 shows the classification of small-scale fading due to multipath delay spread.

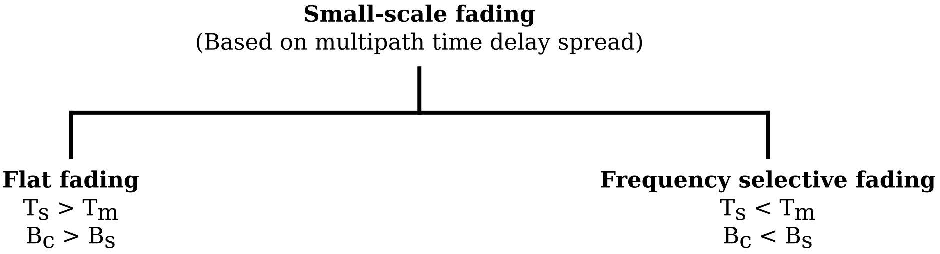

Figure 2.1: Classification of small-scale fading according to multipath delay spread.

2.1.2.2 Fading effects due to Doppler spread

Considering that exists relative motion between the transmitter and the receiver, the multipath propagation phenomena will be a time varying function. Coherence time and Doppler spread may be used to quantify the nature of the channel [Rap01]:

- Coherence time (T_c) : Coherence time, T_c, is the time duration over which the channel impulse response is time invariant. Signals separated in time by the coherence time have independent fading.

- Doppler spread (B_D): When a pure sinusoidal tone of frequency f_c is transmitted in multipath environment, the received signal spectrum, called Doppler spectrum, will have components in the range $f_c - f_D$ to $f_c + f_D$, due to Doppler shift, f_D. The Doppler spread is the width of the Doppler spectrum.

Small-scale fading based on Doppler spread can be classified as [Rap01]:

- Slow fading: Occurs when the coherence time of the channel, T_c, is greater than the symbol time duration, T_s (i.e. $T_c > T_s$). The channel exhibits slow fading if the channel impulse response changes at a rate much slower than the transmitted symbol time. In the frequency domain, the signal bandwidth is greater then the Doppler spread (i.e. $B_s > B_D$), and in that case the effects of Doppler spread are negligible at the receiver.

- Fast fading: Happens when the coherence time duration T_c, in which the channel has a correlated behavior, is shorter than the symbol time duration T_s (i.e. $T_c < T_s$). In this case the channel impulse response changes rapidly within the symbol time duration. In the frequency domain, the signal bandwidth is less than the Doppler spread (i.e. $B_s < B_D$). The signal distortion due to fast fading increases with increasing Doppler spread relative to the bandwidth of the transmitted signal. In practice, fast fading only occurs for very low data rates.

Figure 2.2 shows the classification of small-scale fading due to Doppler spread.

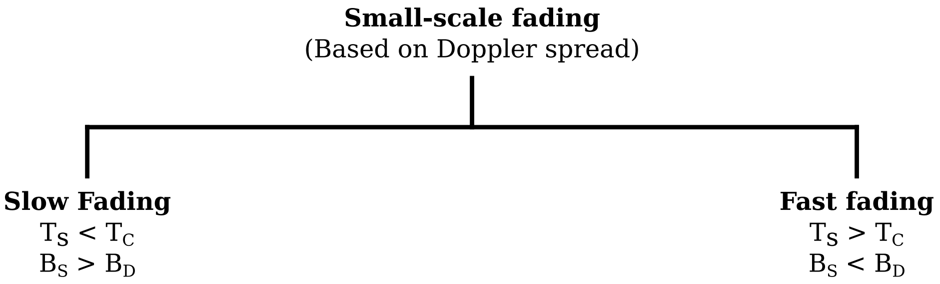

Figure 2.2: Classification of small-scale fading according to Doppler spread.

2.1.2.3 Modeling fading channels

Depending on the nature of the radio propagation environment, there are several probability distributions to characterize the fading channel in a statistical approach [SA05].

Rayleigh model

Rayleigh distribution is used to model multipath fading, when all the multipath components arrive at the receiver with identical signal amplitude (without a dominant path) [SA05].

To derive the statistical characteristics of the received signal that is due to the superposition of partial waves, it is assumed that the received signal is defined as [Gol05]

$$r(t) = \Re\mathfrak{e}\left\{\left[\sum_{n=0}^{N} \alpha_n(t) e^{-j\phi_n(t)}\right] e^{j2\pi f_c t}\right\} = r_I(t)\cos(2\pi f_c t) + r_Q(t)\sin(2\pi f_c t), \tag{2.9}$$

where α_n is the amplitude of n^{th} multipath component, N is the number of multipath components, ϕ_n is the relative phase, and f_c is the carrier frequency.

The In-phase/Quadrature (IQ) components are given by [Gol05]

$$r_I(t) = \sum_{n=0}^{N} \alpha_n(t)\cos(\phi_n(t)) \tag{2.10}$$

and

$$r_Q(t) = \sum_{n=0}^{N} \alpha_n(t)\sin(\phi_n(t)). \tag{2.11}$$

For a large number of multipath components, N, according to Central Limit Theorem, the IQ components are Gaussian distributed random variables (RVs).

If IQ components are zero-mean Gaussian variables, distributed according to $\mathcal{N}(0, \sigma^2)$, then the signal envelope is Rayleigh distributed [PS07]. Signal envelope in relation to IQ components can be written as [Gol05],

$$z(t) = |r(t)| = \sqrt{r_I(t)^2 + r_Q(t)^2}, \tag{2.12}$$

and the Rayleigh distributed signal envelope can be written as [SA05]

$$P_Z(z) = \frac{z}{\sigma^2} e^{-\frac{z^2}{2\sigma^2}}. \tag{2.13}$$

Rician model

In contrast to Rayleigh fading, if the channel has a fixed line of sight component, which can represent the dominant multipath signal component, the multipath fading may be approximated by a Rician distribution [Gol05]. Then in-phase ($r_I(t)$) and quadrature phase ($r_Q(t)$) components are not zero-mean random variables, and the signal envelope should be characterized by the superposition of a LOS component and a complex Gaussian component. The probability density function (PDF) of Rician fading envelope can be written as [Gol05]

$$P_Z(z) = \frac{z}{\sigma^2} e^{-\frac{z^2+A^2}{2\sigma^2}} I_0\left(\frac{Az}{\sigma^2}\right), \tag{2.14}$$

where the parameter A denotes the peak amplitude of the dominant signal and $I_0(.)$ is the modified Bessel function of the first kind and zero-order. Note that, when the amplitude of the dominant signal decreases ($A \rightarrow 0$), the Rician distribution is equivalent to a Rayleigh distribution [Rap01].

Nakagami-m model

Nakagami-m fading is a more generalized way of modeling small-scale fading and can be transformed into a Rayleigh or a Rician fading model through the assignment of appropriate parameter values in the distribution [Gol05]. The Nakagami-m fading distribution is given by [Nak60]

$$P_Z(z) = \frac{2m^m z^{2m-1}}{\Omega^m \Gamma(m)} e^{-\frac{mz^2}{\Omega}}, \tag{2.15}$$

where the signal amplitude is denoted by $z \geq 0$, m is the Nakagami-m fading parameter, which ranges from $1/2$ to ∞, Ω is the average fading power ($\mathbf{E}(z^2)$), and $\Gamma(.)$ is the Gamma function. The parameter m, that determines severity of fading can be expressed as [PS07]

$$m = \frac{\mathbf{E}^2[z^2]}{\mathbf{E}[(z^2 - \mathbf{E}[z^2])^2]}, m \geq \frac{1}{2}. \tag{2.16}$$

By setting $m = 1$, (2.15) reduces to a Rayleigh distribution [PS07]. Finally, the Nakagami-m distribution frequently gives the best fit to land-mobile and indoor-mobile multipath propagation environment [SA05].

Lognormal shadowing model

Slow variations around the mean signal level due to the shadowing from hills, buildings or other large obstacles is commonly referred to as shadowing. The most common model for this additional attenuation is the Lognormal shadowing model, where the amplitude of the attenuation (z) follows a standard Lognormal distribution given by [SA05],

$$p(z) = \frac{\xi}{\sqrt{2\pi}\sigma_{z_{dB}}\psi} e^{\left[-\frac{\left(10\log_{10} z - \mu_{z_{dB}}\right)^2}{2\sigma^2_{z_{dB}}}\right]}, z > 0, \tag{2.17}$$

where $\xi = 10 \ln 10$, $\mu_{z_{dB}}$ is the mean of $z_{dB} = 10 \log_{10} z$ in dB and $\sigma_{z_{dB}}$ is the standard deviation of z_{dB}, also in dB.

2.2 Interference in wireless networks

The interference experienced in a wireless system may be classified in different types:

- Self-interference;
- Multiple access interference (MAI);
- Co-channel interference (CCI);
- Adjacent channel interference (ACI).

Self-interference

The SI is caused when a node transmits and receives simultaneously in the same frequency band. If not canceled, the transmitted signal is jointly received with the signal to decode from other transmitter(s). Usually, the transmitted signal power is few orders of magnitude larger than the received signal power from other nodes. Thus, when a node transmits and receives simultaneously in the same channel, the received signal is overshadowed by the transmitted signal of the node itself [Rii+11].

Multiple access interference

Multiple access interference (MAI) is a type of interference caused by multiple transmitting nodes using the same frequency allocation at the same time to a single receiver. The MAI can represent a significant problem if the power level of the desired signal to decode is significantly lower than the power level of the aggregate interference caused by the multiple nodes that are simultaneously transmitting [MP02].

Co-channel interference

The CCI is the interference mutually caused by the links that reuse the same wireless channel, which is due to the frequency reuse in cellular networks. In cellular systems CCI is also known as inter-cell interference. The frequency spectrum is a precious resource that is divided into non-overlapping spectrum bands that are assigned to different cells. However, after certain geographical distance, the frequency bands are reused, i.e. a given spectrum band is reassigned to several distant cells. Thus, signals at the same frequencies (co-channel signals) arrive at the receiver from the undesired transmitters located (far away) in some other cells and cause underperformance on the receiver side [YP03].

Adjacent channel interference

Adjacent channel interference (ACI) is the interference between links that communicate geographically close to each other using neighboring frequency bands. ACI is mainly due to electronic impairments, which may cause inadequate filtering, improper tuning or poor frequency control [Nac+08].

2.2.1 Multiple access interference modeling

In a wireless network composed of several spatially distributed nodes, different issues affect the nodes' communication, such as the wireless propagation effects, network interference and thermal noise. The propagation effects include path loss, shadowing and multipath fading. The network interference is due to the aggregation of signals radiated by other transmitters, which involuntarily affect the receiving nodes in the network. The thermal noise is due to the thermal agitation of electrons in the circuitry and is typically modelled as Additive White Gaussian Noise (AWGN) [Win+09].

Interfering nodes (transmitters) are defined as the set of terminals that are transmitting within the frequency band of interest, during the time interval of interest (e.g., a symbol or packet time), and hence are effectively contributing to the interference.

The modeling of network interference in wireless networks plays an important role in several applications, ranging from localization [Pah+02], security [GN08], spectrum sensing [Rab+11] and others. The importance of characterizing the interference generated by a wireless network has increased with the emergence of spectrum sharing, cognitive radio, and the needs introduced by multiple access networks (e.g. carrier sensing and medium access probability).

A model for aggregate interference should consider the following physical parameters, which play an important role at different domains [Win+09]:

- the spatial distribution of the interferers scattered in the network;
- the transmission characteristics of the interferers, such as modulation, power and synchronization;
- the propagation characteristics of the medium, such as path loss, shadowing and multipath fading.

Spatial distribution of the nodes

The spatial distribution of the nodes (interferers) in wireless networks impacts on the characterization of the aggregate interference, particulaly when no power control schemes are adopted. The location and number of the nodes can be modeled by a deterministic or stochastic spatial distribution. Deterministic distributions of the nodes are applicable if the exact locations and number of nodes are known or if the nodes are located according to a specific structure. Deterministic models include square, triangular, and hexagonal lattices in the two-dimensional plane [HG09]. However, it is more convenient to model the distribution of the nodes stochastically. The stochastic model most commonly used to approximate the spatial distribution of the nodes of a wireless network is the Poisson Point Process (PPP) [HA07; Hea+13; PW07; Win+09].

Considering the spatial distribution of the nodes modeled as a homogeneous Poisson process in the two-dimensional infinite plane, the probability of finding n nodes located in a region R depends only on the total area A_R of the region and, is given by [PP02]

$$P\{n \quad \text{in} \quad R\} = \frac{(\lambda A_R)^n}{n!} e^{-\lambda A_R}, \tag{2.18}$$

where λ is the spatial density of the nodes, in nodes per unit area.

Nodes' mobility

In several real world scenarios the nodes are moving, which introduces the need for a mobility model in a simulation environment. Several mobility models have been investigated in the last years, with a diversity of different approaches and solutions.

One of the most adopted mobility model in research on wireless networks is the RWP mobility model [Bet+03; Bet+04]. In a RWP mobility scenario n nodes move in a region defined by the area $X_{max} \times Y_{max}$. Each node is initially placed in a random position (x,y). The position is sampled from the uniform distributions represented by $x \sim U(0, X_{max})$ and $y \sim U(0, Y_{max})$. (x, y) represents the starting point. The ending point, (x', y'), is also uniformly chosen as the starting point (i.e. $x' \sim U(0, X_{max})$ and $y' \sim U(0, Y_{max})$). A node uniformly chooses the velocity $V \sim U(V_{min}, V_{max})$ to move from the starting point to the ending point. After reaching the ending point (x', y'), a node randomly chooses a pause duration (T_p), and remains stopped at the ending point during this period of time. After elapsing T_p, a node uniformly chooses a new velocity value to move to another ending point uniformly chosen. After reaching the ending point a node repeats the same cycle as many times as required. Each node moves independently from other nodes.

Another frequently used approach is the random direction (RD) model [Bet01]. A node moving according to the RD model is generally described by a stochastic process. Each node has an initial direction $\phi(t = 0)$ which is chosen from a uniform distribution (i.e. $\phi \sim U(0, 2\pi)$). A node chooses a direction angle ϕ_i and then moves with speed V_i for a certain movement time T_i. After pausing for a period of time T_p it starts over. Similar to the RWP model, each node moves independently from other nodes.

A different approach is the random walk (RW) mobility model. This mobility model is strongly connected to Brownian motion. Its main application is in modeling the movement of users in a cellular network. Here, a node located in a certain cell is able to move to a predefined number of neighboring cells. In each time step the node stays within its cell with a given probability or moves to one of the neighboring cells with a given transition probability. This process is usually modeled via a Markov chain [CS01; Jab+98].

2.2.1.1 Characterization of the aggregate interference

In [HG09], the authors derive results for the interference characterization in wireless networks. The total aggregate interference can be seen as the summation of the received power of each active transmitter. Specifically, in [HG09] the total interference power received by the node N_c located in the centre of an annulus l (see figure 2.3) is expressed by

$$I = \sum_{i=1}^{n_l} I_i, \tag{2.19}$$

where I_i is the interference caused by the i-th node, and n_l is the total number of nodes located in the annulus.

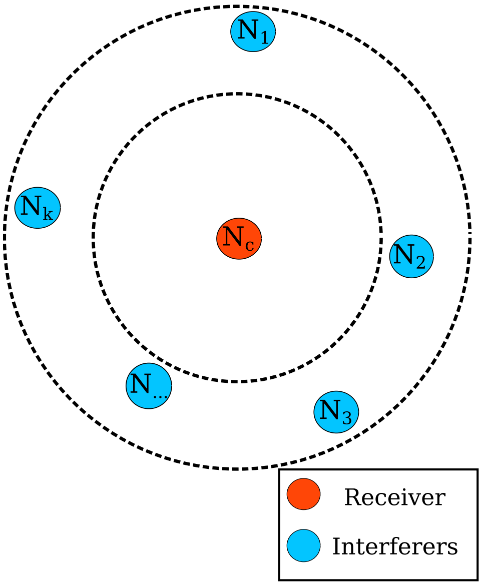

Figure 2.3: Aggregate interference caused to N_c by the hypothetical transmitters $\{N_1, N_2, ..., N_k\}$ located in the interference region.

The interference power I_i is given by

$$I_i = P_{Tx} \psi_i r_l^{-\wp}, \tag{2.20}$$

where P_{Tx} is the transmitted power level of the i-th node, ψ_i represents the fading and shadowing gain observed in the channel between the RX and node i. r_l represents the distance between the i-th interferer and the RX. $\wp$ represents the path loss coefficient.

Attenuation models

Another important factor affecting the characterization of the aggregate interference is the distance-dependent attenuation model. The relevant models may be categorized into two categories: singular (unbounded) and non-singular (bounded) models. In singular models, the function that is used to reflect the distance-dependent attenuation goes to infinity when the distance between the receiver and the interferer is zero. On the other hand, the non-singular models avoid this singularity by not allowing the interferer to be placed close to the receiver, or by using a function that does not have a singularity at zero. The following distance-dependent attenuation models are usually considered [GH08; HG09]:

- Singular model: $g(x) = |r_l|^{-\wp}$;
- Non-singular model: $g(x) = (1 + |r_l|^{\wp})^{-1}$.

[SS90] characterizes the aggregate interference of a wireless network assuming that the spatial distribution of interferers follows a PPP and use singular distance-dependent attenuation model. Under these assumptions, the characteristic function (CF) of the aggregate interference is obtained in a closed-form expression, and through the CF the authors conclude that the aggregate interference power is an alpha-stable RV . Other works investigate the aggregate interference in wireless networks using PPP and non-singular models [Lic+10; Vu+09].

The authors in [GH08] show that when the path loss model is singular, the interference can be approximated by an heavy tail distribution, irrespective of the fading distribution, and when the path loss model is bounded, the interference tail can be approximated by the tail of fading distribution. However these results are only observed for non-mobile networks.

Guard zone

In wireless networks, it is necessary to suppress transmissions of the nodes close to the desired receiver in order to improve the receiver's capacity. The exclusion zone around the receiver is also known as the guard zone, which usually represented by a disc around the receiver, within which no interfering transmitters are allowed [HA07].

The guard zone of node N_c, $b(N_c, D)$, is a disc of radius D around N_c, as illustrated in Figure 2.4. In this example, the guard zone around the receiver N_c indicates that the node N_1 must avoid transmitting while the $\{N_2, N_3, ..., N_k\}$ outside the receiver's guard zone are allowed to transmit.

The guard zone of radius D encircling the receiver limits the aggregate interference by inhibiting the nearby dominant interferers within the disc $b(N_c, D)$. Therefore, there is a tradeoff between interference suppression and the spatial reuse of the band, which can be modified by appropriately choosing the guard zone size in order to maximize spatial reuse [HA07].

Gaussianity of the distribution of the aggregate interference

The most common approach to model the interference is approximating the distribution of the aggregate interference as a Gaussian random variable, since the aggregate interference can be considered as the sum of a large number of independent interference signals, and thus the central limit theorem (CLT) applies. However, some observations in literature suggest that this Gaussian approximation is not valid, particularly when there are dominant interferers, due to the near-far effect [Win+09].

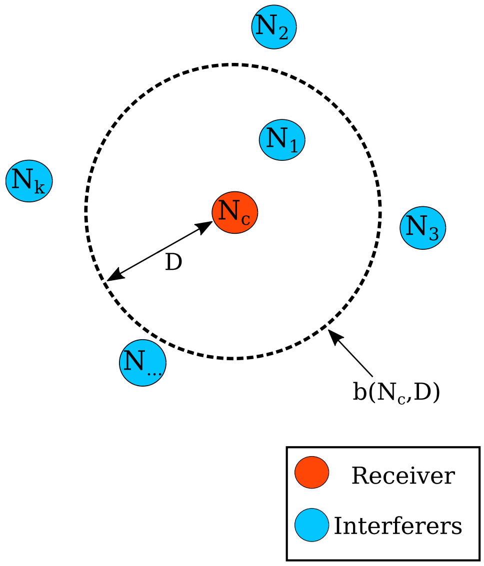

Figure 2.4: Example of a guard zone in a simple network.

The authors in [CH01] consider the interference in a code division multiple access (CDMA) network and show that the distribution of the aggregate interference from users in other cells is Gaussian distributed if there is a large number of interfering users in the vicinity of the receiving cell. The authors in [EE99] also consider the aggregate interference in a CDMA network and show that the distribution of the aggregate interference converges to a Gaussian distribution when the average number of interferers in a cell goes to infinity. It is indicated in [GH08],*"the Gaussian distribution is a bad approximation for the distribution of the aggregate interference when the node density is low"*. Based on simulation results, [HA07] shows that the Gaussian approximation could be acceptable when there is a wide-enough exclusion region (with no interferers) around the receiver. In [AY10], the authors studied the Gaussian convergence of the distribution of the aggregate interference and showed that an increase in the size of the exclusion region, and consequently in the number of interferers, brings the distribution of the aggregate interference closer to the Gaussian distribution. Increasing the active node density has a similar effect. However, the convergence is faster with the increase in the size of the exclusion region compared with the increase of the density of active nodes (transmitters). In contrast, channel fading causes divergence from Gaussianity. Shadow fading typically causes more divergence, as compared with multipath fading [AY10].

In most mobile scenarios, the aggregate interference can not be modeled by a Gaussian distribution. However, a different conclusion is taken in [Zha+13], which considers a mobile ad hoc network where the nodes move according to the RD model. The PDF of the distance between any pair of nodes is used to characterize the aggregate interference due to path loss. Since a static receiver is assumed in the RD model, the distances between interferers and the receiving node can be regarded as independent RVs, and the CLT applies. In this case, a Gaussian modeling approach can be used.

Non-Gaussian modeling approaches

In the majority of wireless scenarios the characterization of the aggregate interference is a complex task and most of the times the aggregate interference can not be approximated by a Gaussian distribution. Several works characterize the aggregate interference in non-Gaussian conditions [Gul+12; PW10; Win+09]. In [Gul+12] the interference caused by multiple nodes is modeled by an alpha stable distribution. While no mobility is assumed, the authors consider random transmission durations, which can also be interpreted with respect to the varying user mobility. The static and highly mobile network models are included as special cases in the network model by appropriately choosing the random transmission duration distribution. Thus, the authors observed that the temporal dependence in interference increases as the user mobility decreases and/or the total transmission time increases.

Mainly due to the complexity of non-Gaussian modeling approaches, aggregate interference modeling in mobile scenarios has received limited attention. The use of statistical information related with the mobility of the interferers in the interference modeling was only carried out in two works [GH14; Yar+08]. In [Yar+08] the interference is caused by static nodes and the mobility of the terminals only causes a time-varying displacement with respect to the different cells. [GH14] assumes that interferers may move according to the RWP mobility model, but only the contribution from the nearest interferer to the receiver is considered, neglecting the contribution of the nodes farther away.

Methods to characterize the aggregate interference

In the current literature, it is often assumed that the wireless networks have a random network topology. However, only particular combinations of spatial node distributions, path loss models and receiver locations have been characterized in terms of the PDF of the aggregate interference [ElS+13]. For example, a finite number of interferers together with certain fading distributions, such as Rayleigh, Lognormal or Gamma, allow exploiting a vast amount of literature on the sum of RVs [Alo+01; HB05; Kar+06; Meh+07; Mos85]. In the general case, the PDF is unknown and aggregate interference is typically characterized through the Laplace Transform (LT), the CF or the Moment Generating Function (MGF) [ElS+13].

In the literature, there are two main techniques adopting the LT, the CF, or the MGF in order to characterize the aggregate interference [ElS+13]:

Technique 1: Inversion

In this technique, the LT, the CF, or the MGF is inverted to obtain the PDF of the interference [Pin+09; Win+09]. Due to the complex nature of the expressions for the LT, the CF, or the MGF, usually the PDF of the aggregate interference cannot be obtained in closed form. This technique is only useful for very special cases of PPP where the expressions for the LT, the CF, or the MGF are invertible or match the LT, the CF, or the MGF of a known distribution [Pin+09; Win+09]; otherwise, inversion is done numerically [Ina+09].

Technique 2: Resort to the Approximation of the PDF of the Aggregate Interference

In this technique, the PDF of the aggregate interference power is approximated by one of the known PDFs. The parameters of the approximate PDF are obtained via the LT, the CF, or the MGF. For instance, if the PDF of the aggregate interference is approximated by the Gamma distribution, then the mean and the standard deviation will be obtained from LT, the CF, or the MGF of the aggregate interference. This method is often referred to as the moment-matching method [BS98]. In the literature, different papers used different PDFs according to the particularities of the problem and the results are usualy verified via simulations. In [HA07], the aggregate interference was approximated via a Gaussian distribution. In [Rab+11], the PDF of aggregate interference power was approximated by a truncated stable distribution.

Based on the methods mentioned above, the aggregate interference in a Poisson field of interferers was first studied in [SS90]. This work assumes that the transmitted power is fixed, and no fading is considered. The technique described in [SS90] consists of two steps:

1. The authors first consider a finite network, a disk of radius a centered at the origin, and subject to a fixed number of nodes located in the finite disk (which can be stated as a conditional probability). The nodes' locations are considered as being independent and identically distributed.
2. Then the authors de-condition on the (Poisson) number of nodes and let the disk radius go to infinity.

Step 1: Consider that the interference (I_a) from the nodes located within distance a of the origin ($b(o,a)$) is given by

$$I_a = \sum_{x \in \Phi \cap b(o,a)} g(|x|), \tag{2.21}$$

where Φ is a point process of interferers and $g(x)$ is the path loss law. Let φ be the CF of I_a, i.e.

$$\varphi_{I_a}(w) \triangleq \mathbf{E}(e^{jwI_a}). \tag{2.22}$$

Conditioning on having k nodes in the disk of radius a, by the law of total expectation,

$$\varphi_{I_a}(w) = \mathbf{E}\Big(\mathbf{E}\Big(e^{jwI_a} | \Phi(b(o,a)) = k\Big)\Big). \tag{2.23}$$

Given that there are k points in $b(o,a)$, the distribution of their locations is that of k independent and identically distributed points with uniform 2-D distribution. If R is the distance to the origin of a point that is uniformly distributed in $b(o,a)$, then the probability density of R is given by

$$f_R(r) = \begin{cases} \dfrac{2r}{a^2} & 0 < r < a \\ 0 & \text{otherwise} \end{cases} \tag{2.24}$$

and the CF of the k independent RVs is the product of the k individual CFs, we have

$$\mathbf{E}\left(e^{jwI_a}|\Phi(b(o,a))=k\right)=\left(\int_0^a \frac{2r}{a^2}e^{jwg(r)}dr\right)^k. \tag{2.25}$$

Step 2: The probability of finding k nodes in $b(o,a)$ is given by the Poisson distribution, thus the CF of I_a is given by

$$\varphi_{I_a}(w)=\sum_{k=0}^{\infty}\frac{(\lambda\pi a^2)^k e^{-\lambda\pi a^2}}{k!}\mathbf{E}\left(e^{jwI_a}|\Phi(b(o,a))=k\right). \tag{2.26}$$

Replacing (2.25) in (2.26), summing over k, and interpreting the sum as the Taylor expansion of the exponential function, we obtain

$$\varphi_{I_a}(w)=\exp\left(\lambda\pi a^2\left(-1+\int_0^a \frac{2r}{a^2}e^{jwg(r)}dr\right)\right). \tag{2.27}$$

Integrating by parts, substituting $r\rightarrow g^{-1}(x)$, where $g^{-1}(x)$ is the inverse of g, and letting $a\rightarrow\infty$ in order to find the total interference power at the origin (I), we have

$$\varphi_I(w)=\exp\left(j\lambda\pi w\int_0^{\infty}(g^{-1}(x))^2 e^{jwx}dx\right). \tag{2.28}$$

To get more concrete results, the path loss law should be specified. For the standard power law $g(x)=r^{-\wp}$, where $\wp$ is the path loss coefficient, we obtain

$$\varphi_I(w)=\exp\left(j\lambda\pi w\int_0^{\infty}x^{-2/\wp}e^{jwx}dx\right). \tag{2.29}$$

For $\wp\leq 2$, the integral diverges and for $\wp>2$, (2.29) becomes

$$\varphi_I(w)=\exp\left(-\lambda\pi\Gamma(1-2/\wp)w^{2/\wp}e^{-j\pi/\wp}\right), w\geq 0, \tag{2.30}$$

where $\Gamma(.)$ is the Gamma function. For $\wp=4$,

$$\varphi_I(w)=\exp\left(-\lambda\pi^{3/2}\exp(-j\pi/4)\sqrt{w}\right). \tag{2.31}$$

This case is of particular interest, since it is the only one where a closed-form expression for the PDF exists,

$$f_I(x)=\frac{\pi\lambda}{2x^{3/2}}\exp\left(-\frac{\pi^3\lambda^2}{4x}\right), \tag{2.32}$$

which is the so-called Lévy distribution.

An unifying framework that characterizes the network interference in a wireless environment subject to path loss, shadowing, and multipath fading is presented in [Win+09]. [Win+09] assumes that the nodes are scattered according to a spatial PPP and that each interferer contributes with the term P_i to the aggregate interference power. P_i represents an arbitrary quantity associated with interferer i and can incorporate various propagation effects such as multipath fading or shadowing, R_i denotes the distance between the origin and the interferer i, and $2b$ is the path loss coefficient, with $b = 1$ corresponding to free-space propagation. Therefore, the aggregate interference power at the origin generated by all nodes scattered in the infinite plane is given by

$$I = \sum_{i=0}^{\infty} \frac{P_i}{R_i^{2b}}, \tag{2.33}$$

for $b > 1$. Then, the CF $\varphi_I(w) = \mathbf{E}(e^{jwI})$ is given by

$$\varphi_I(w) = \exp\left(-\gamma |w|^{\alpha} \left[1 - j\beta \operatorname{sign}(w) \tan\left(\frac{\pi\alpha}{2}\right)\right]\right), \tag{2.34}$$

where

$$\alpha = \frac{1}{b}, \tag{2.35}$$

$$\beta = 1, \tag{2.36}$$

$$\gamma = \pi\lambda C_{1/b}^{-1} \mathbf{E}\left(P_i^{1/b}\right), \tag{2.37}$$

and

$$C_\alpha = \begin{cases} \dfrac{1-\alpha}{\Gamma(2-\alpha)\cos(\pi\alpha/2)}, & \alpha \neq 1 \\ \\ \frac{2}{\pi}, & \alpha = 1 \end{cases}, \tag{2.38}$$

with $\Gamma(.)$ denoting the Gamma function and λ the spatial density of the interfering nodes. [Win+09] concludes that the CF in (2.34) follows a skewed stable distribution, expressed as

$$I = S\left(\alpha = \frac{1}{b}, \beta = 1, \gamma = \pi\lambda C_{1/b}^{-1} \mathbf{E}\left(P_i^{1/b}\right)\right). \tag{2.39}$$

Using a binomial point process (BPP) to scattering a fixed (and finite) number of nodes in a given area, [SH07] obtains the MGF of the interference in closed-form, caused by N nodes transmitting to a central base station and utilizes the MGF to compute the cumulants of the interference. In [SH07], the interference (I) at the center, due to the k nodes in the annulus between the inner radius A and outer radius B, is given as a sum of the received signal strengths from the individual nodes,

$$I = \sum_{i=1}^{k} I_i(g_i, r_i) = \sum_{i=1}^{k} g_i r_i^{-\wp}, \tag{2.40}$$

where r_i is the Euclidean distance from the i-th node to the base station, g_i is the fading state on that link, and $\wp$ is the path loss exponent. The conditional MGF, is represented in a product form and is given by

$$M_{I|k}(s) = \mathbf{E}\left[e^{-s(I_1(g_1,r_1)+I_2(g_2,r_2)+\ldots+I_k(g_k,r_k))}\right] = \prod_{i=1}^{k} M_i(s). \tag{2.41}$$

The MGF of the interference in closed-form is given in [SH07], and the n-th cumulant of the interference is defined as

$$C_n = (-1)^n \frac{d^n}{ds^n} \ln M_I(s)|_{s=0}. \tag{2.42}$$

[Rab+11] proposed a new statistical model for the aggregate interference of a cognitive radio network, accounting for the sensing procedure, spatial density of the secondary users and environment-dependent conditions such as path loss, shadowing, and channel fading. This work considers that the secondary users are spatially scattered according to an homogeneous PPP in a two-dimensional plane and the victim primary user is assumed to be located at the center of the region. [Rab+11] first expresses the CF of the cognitive interference, from which derives the cumulants. Lastly, using these cumulants [Rab+11] shapes the cognitive network interference as a symmetric truncated-stable RV.

[GS08] developed a statistical model for the aggregate interference in spectrum-sensing cognitive wireless networks, taking into account the random variations in the number, location and transmitted power of the cognitive radios as well as the propagation characteristics. The normalized aggregate interference at the primary receiver was considered as

$$I = \sum_{i \in \Phi} x_i r_i^{-\wp}, \tag{2.43}$$

where x_i represents the distance-independent frequency-flat channel fading, r_i is the distance between the cognitive radio i and the primary receiver, Φ is a homogeneous spatial Poisson point process of intensity $\lambda(r, x)$ and $\wp$ is the path loss coefficient. Applying Campbell's theorem [Kin93] the CF of I, denoted by φ_I, was derived in [GS08]. The derived CF is usually numerically inverted to compute the exact PDF of the aggregate interference. However, [GS08] is not following this approach. Instead, the authors derive exact and possibly closed-form expressions for the cumulants of the aggregate interference. The n-th cumulant of I was obtained from the CF φ_I, being given by

$$k_n = \frac{1}{j^n}\left[\frac{d^n \ln\varphi_I}{dw^n}\right]_{w=0}. \tag{2.44}$$

Using the closed-form expressions of k_n under the various fading distributions (Lognormal shadowing and Nakagami-m fading), [GS08] approximates the distribution of the aggregate interference by the Edgeworth Expansion approximation, the Shifted Lognormal approximation and the Lognormal approximation.

Contrarily to the works mentioned above, [GH14] characterizes the interference in a mobile random network. [GH14] assumes that interferers may move according to the RWP mobility model and the interference is evaluated in a finite network without fading and in a finite network with multi-path fading. This work only considers the interference from the nearest interferer to the receiver, neglecting the contribution of the nodes farther away. For the example, without fading, the interference power is approximated by

$$I \approx I_1 = R_1^{-\wp}, \tag{2.45}$$

where I_1 is the interference from the nearest interferer, R_1 is the distance between the origin and the nearest interferer and $\wp$ is the path loss exponent.

Table 2.2 provides a taxonomy for the literature according to the network type, propagation characteristics, distribution of the nodes, and the technique adopted to model the aggregate interference. Note that if the same reference appears in different categories of the taxonomy, this means that the reference uses all the selected techniques. The taxonomy in Table 2.2 also shows the popularity of each distribution of the nodes. Analyzing the Table 2.2, we concluded that the PPP is the most adopted model used to characterize the nodes' distribution in the literature, because of its simplicity. On the other hand, we observe that the CF is the most common technique to characterize the aggregate interference.

Table 2.2: Taxonomy of the literature based on the network type, propagation characteristics, distribution of the nodes, and the technique used to obtain the aggregate interference.

			Gaussian	**Non Gaussian**			
Network Type	**Propagation**	**Distribution of Nodes**	CLT	MGF	CF	LT	Cumulants
Ad hoc	Path Loss	PPP	-	-	[SS90]	-	-
		BPP	-	-	-	-	-
		RD	[Zha+13]	-	-	-	-
		RWP	-	[Iri+15a]	-	-	-
	Path Loss & Fading	PPP	[AY10]	-	[PW10; Win+09]	[GH08; Hea+13]	-
		BPP	-	[SH07]	-	-	[SH07]
		RD	-	-	-	-	-
		RWP	-	-	-	[GH14]	-
Cognitive	Path Loss	PPP	[Men+05]	-	-	-	-
		BPP	-	-	-	-	-
		RD	-	-	-	-	-
		RWP	-	-	-	-	-
	Path Loss & Fading	PPP	[BJ10]	-	[GS08; Rab+11; Win+09]	-	[GS08; Rab+11]
		BPP	-	-	-	-	-
		RD	-	-	-	-	-
		RWP	-	-	-	-	-

2.3 Self-Interference

The SI is caused by the fact that a single node simultaneously transmits and receives over the same frequency band. Thus, a node can cause interference to itself when the receiving antenna is receiving a signal from a neighbor plus the signal simultaneously transmitted in the same band.

Current wireless communication systems, including but not limited to cellular and local area networks, are half-duplex communication systems, meaning that the available resources are divided either in time domain or in frequency domain. Consequently, transmission and reception occur either at different times or in different frequency bands. Recently, a different approach has been investigated where the wireless terminals transmit and receive simultaneously over the same frequency band [Hei+15; Kim+15; Zha+15], which is known as In-Band Full-Duplex (IBFDX) communications [Cho+10a; Wan+15]. The SI is generated in IBFDX systems, and Figure 2.3 shows a IBFDX node equipped with a receiving antenna and a transmitting antenna. The transmitted signal is received by the receiving antenna. The "Direct Path Self-Interference" is the component received in LOS, while the "Multipath Self-Interference" represents the multiple reflections of the transmitted signal that are received by the same node.

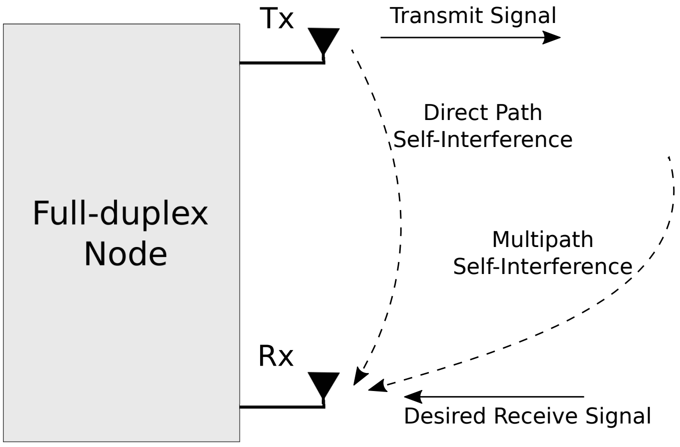

Figure 2.5: SI problem in a IBFDX system.

By using IBFDX communications, the capacity of the communication link may be increased up to twice the amount of half-duplex communication systems [Goy+15; Kim+14; XZ14]. However, to simultaneously transmit and receive, a terminal must separate its own transmission from the received signal, which is usually referred to as SI rejection or cancellation, posing several challenges at different levels, ranging from circuit design to signal processing. Thus, the success of IBFDX communications relies on the performance of SI cancelation techniques.

2.3.1 Self-Interference Rejection Techniques

In IBFDX communications, the transmitter's signal must be reduced to an acceptable level at the RX located in the same node. Any residual SI will increase the RX noise floor, thus reducing the capacity of the RX channel. IBFDX communications' performance is limited by the amount of SI suppression, which may be achieved by two different methods:

- Antenna Isolation (AI) [For+14; Lau+14], to prevent the radio frequency (RF) signal generated by the local TX from leaking into the RX;
- Self-interference Cancellation (SIC) [AE15a; Kor+14b; Lee13], to subtract any remaining SI from the RX path using knowledge of the TX signal and channel estimation.

SI is reduced by both passive (AI) and active techniques (SIC). As shown in Figure 2.6, the reduction in the strength of SI signal ($x_{si}(t)$) via passive methods occurs in a first stage. An active AC operates on the received signal in a second phase, after the passive suppression, and it is performed in analog domain before the received signal passes through the Analog-to-Digital Converter (ADC). The digital cancellation (DC) is the final step of reduction of SI. The cancelling signal is generated by processing the SI signal $x_{si}(t)$. At the receiver, the received signal y_{signal} can be different from the signal of interest denoted by x_{signal}, since the residual SI ($y_{r_{si}}(t)$) and the AWGN thermal noise ($z_n(t)$) can be significantly higher.

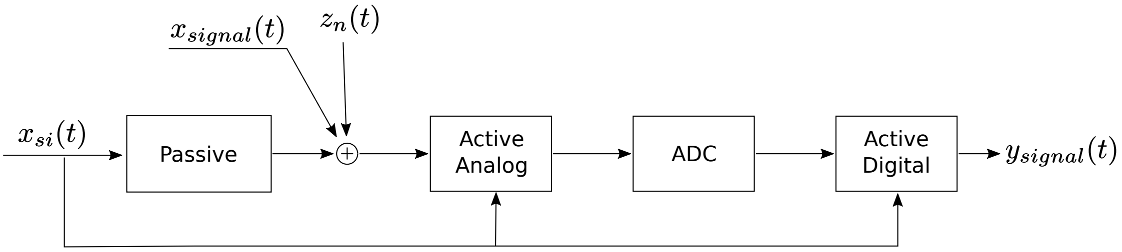

Figure 2.6: SI reduction methods (adapted from [Sah+13]).

Antenna Isolation

The RX's AI is achieved by suppressing interference through path-loss attenuation, placing absorptive material between the transmitting and receiving antennas, or increasing the antennas distance.

The simplest method to suppress the SI is the antenna separation technique, increasing the antennas distance to further increase the attenuation. Considering a IBFDX node equipped with a TX and RX antenna, a larger separation distance between the two antennas causes a higher suppression of the SI signal due to the path loss effect. In the IBFDX designs presented in [DS10] and [Cho+10b], the only AI mechanism utilized is the physical separation of transmit and receive antennas. However, physical separation of the antennas depends on the geometric dimension of the terminals [For+14].

Another approach is to exploit the antenna radiation pattern, carefully placing the receive antenna in radiation null points of the transmit antenna. For example, in [Cho+10b] the IBFDX node uses an extra antenna in addition to the existing receive and transmit antennas. In this work, the signal transmitted in the extra antenna is delayed in relation to the original transmitted signal, in order to be add at the RX antenna. The authors show that the SI signal is mitigated when the extra antenna is positioned at $d + \lambda/2$ from the receive antenna, where d denotes the distance between the RX and the transmit antenna, and λ represents the wavelength of the transmitted signal. The problem is that the radiation null points occur not just at the receive antenna but in the entire coverage zone, consequently the isolation comes at the expense of coverage.

The placement of shielding plates between the TX and RX sides, and the use of orthogonal polarized transmit and receive antennas constitute another suppression technique as described in [Eve+14]. Adopting absorptive shielding and cross-polarization techniques together with mechanisms of directional isolation, [Eve+14] shows that the passive suppression techniques can significantly improve the performance of IBFDX systems. However, some fundamental limitations are encountered, that can be solved by the active cancellation techniques.

Self-Interference Cancellation

The SIC performance depends on the accuracy with which the transmitted signal can be copied, modified and subtracted. The signal to be subtracted is usually a modified copy of the transmitted one, obtained using the predicted channel path between the points where signals are sampled and subtracted. Three different active SIC architectures are reported in the literature:

- Analog-domain cancellation [Bha+13; Pur+09];
- Digital-domain cancellation [AE15a; Cho+10a; Li+18];
- Mixed-signal cancellation (MXC) [Dua12; MLN16; Sah+12].

AC is the active cancellation performed in analog domain before converting the received signal in the ADC. AC can be done either at the analog baseband or at the carrier RF.

Most of the active analog cancellers cancel SI at RF [Sah+13], and the canceling signal may be generated by processing the SI signal prior to the up-conversion stage (pre-mixer cancellers), or after the SI signal being up-converted (post-mixer cancellers). In Figure 2.7, a post-mixer analog canceller is depicted, which reduces the SI signal by generating a canceling path after the up-conversion stage (RF_{up}) that is added to the received signal. The SI signal $x_{si}(t)$ is up-converted to the carrier frequency and transmitted over the SI channel h_I.

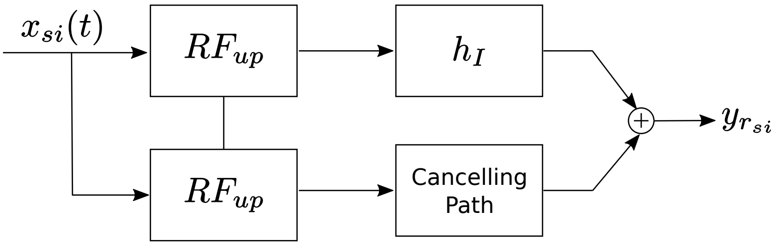

Figure 2.7: Block diagram representation of the post-mixer canceller.

Contrarily, the pre-mixer analog canceller shown in Figure 2.8 generates the canceling path before the up-conversion stage (RF_{up}). In both cases (pre-mixer and post-mixer), the performance is limited by the phase noise PN of the oscillators used in the up/down conversion [Sah+12; Sah+13]. AC presents several challenges, which may include the non-linear effects of power

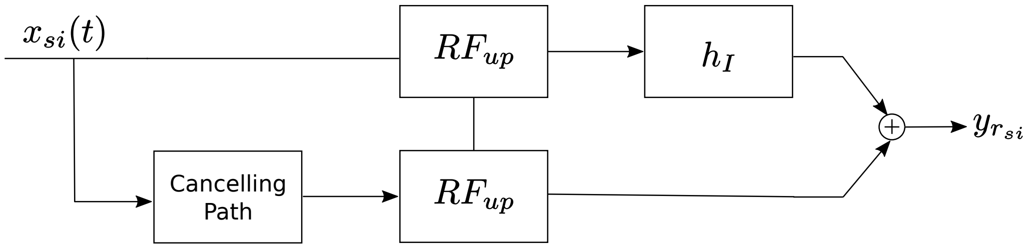

Figure 2.8: Block diagram representation of the pre-mixer canceller.

amplifiers [Kor+14a; LM14], the IQ imbalance [LM14; Sak+14], and the phase noise of both TX and RX [AE15b; Sah+13; Syr+14].

Power amplifiers show significant nonlinearity only when they are operated in their non-linear regime. IQ imbalance does not vary significantly with time and can be calibrated. Regarding PN, it is directly related to the quality of the oscillators used in the up/down frequency conversion. Consequently, AC is mainly limited by the quality of the oscillators, and recent results obtained with commercial oscillators in classical AC schemes show that the SI is at least 15 dB higher than the thermal noise, which is mainly due to the impact of the phase noise in the oscillators' performance [Dua12; Sah+12].

AC schemes can provide up to 40-50 dB cancellation [Bha+13], exhibiting higher performance, due to the fact that the cancellation signal includes all TX impairments. However, it requires processing the cancellation signal in the analog RF domain, increasing hardware costs and complexity. Since the transmitted signal may suffer different propagation effects, a terminal cannot simply cancel the SI by subtracting its transmitted signal from the received one. Rather, DC must be employed to account for the estimated effects of the propagation channel [AE15a; Kor+14b].

In DC schemes the signals are processed in the digital domain, making use of all digital benefits, including the SI wireless channel awareness, through adequate channel estimation techniques. However, DC cannot remove all the SI in the analog RX chain, mainly because the dynamic range of the ADCs limits the amount of suppressed SI, due to the limited effective number of bits (ENOB) [CSM13; Kor+14a]. Commercial ADCs have improved significantly in sampling frequency but only marginally in ENOB.

DC can provide up to 30-35 dB cancellation in practice [Dua+14], being limited by a noisy estimate of the SI channel and noisy components of the self-interferer that cannot be cancelled [Day+12; Rii+11]. Consequently, the SI is usually reduced before the DC through the adoption of an AC technique [Deb+14; Lee13]. By using the two types of cancellation, the channel unaware AC technique suppresses a significant amount of direct-path SI, while the channel aware DC technique may suppress the remaining SI [BK14].

In MXC schemes, both AC and DC are considered. The digital TX signal is processed and converted to analog RF, where subtraction occurs [Dua12; Sah+12], and it is processed after the AC [MLN16; Sah+12]. This requires a dedicated additional upconverter, which limits the cancellation of current MXC schemes to 35 dB [Sah+12]. To achieve an overall SI suppression close to 100 dB above the noise floor, both AC and DC must be used in a MXC scheme [Dua12].

2.3.2 Residual Self-Interference Modelling

IBFDX systems require strong SI cancellation and suppression. However, perfect cancellation/-suppression is not possible in practice and a residual SI is always found. The residual SI is mainly due to estimation errors occurring during the time domain cancellation [Dua+12], and has been addressed in various works in the literature [IO18; Iri+18a; Kor+14a; Li+17; ML16; Nad+17; Sam+17; Sho+17].

[Kor+14a] has identified the quantization-noise, the phase-noise in the local oscillator, and the channel estimation error, as being the main causes of incomplete SI cancellation in different IBFDX schemes. [ML16] has analyzed nonlinear distortion effects occurring in the TX power amplifier and also due to the quantization noise of the ADCs in the RX chain.

The uncertainty associated with the residual SI channel was studied in [Li+17], which has proposed a block training scheme to estimate both communication and residual SI channels in a two-way relaying communication system. The residual SI channel was also studied in [Nad+17], showing that the channel can be modeled as a linear combination of the original signal and its derivatives. The authors adopt a Taylor series approximation to model the channel with only two parameters, and a new SI cancellation scheme based on the proposed channel model is also described.

[Sam+17] investigated the detrimental effects of phase noise and in-phase/quadrature imbalance in IBFDX OFDM transceivers, showing that more sophisticated digital-domain SI cancellation techniques are needed to avoid severe performance degradation. [Sam+17] derives a closed-form expression for the average residual SI power and describes its functional dependence on the parameters of the radio-frequency impairments.

The residual SI was also characterized in [Sho+17] for a multi-user multiple-input multiple-output (MIMO) setup considering IBFDX multi-antenna nodes and assuming the availability of perfect channel state information. The authors show that for the MIMO scenario the residual SI can be approximated by a Gamma distribution assuming time-invariant channels.

[IO18] investigated if the residual SI power can be accurately approximated by known distributions. The paper shows that Weibull, Gamma and Exponential distributions fail to approximate the residual SI power in an accurate way. This observation was only based on Monte Carlo simulation results, from which the parameters of the known distributions were obtained using a fitting tool based on the Maximum Likelihood Estimation method.

Based on experimental results reported in [Dua+12], the distribution of the SI channel differs according to the applied cancellation/suppression technique. Specifically, [Dua+12] reports that before applying active cancellation the SI channel has a strong LOS component and the magnitude of the residual SI can be modeled as a Rician distribution with large K-factor. After applying active cancellation the LOS component is efficiently suppressed, hence, the magnitude of residual SI can be modeled as a Rician distribution with smaller K-factor.

CHAPTER 3

INTERFERENCE IN MOBILE NETWORKS

3.1 Introduction

Interference plays an important role in the future generation of wireless communication systems because the traditional single transmitter and receiver model is being progressively replaced by a different approach, where multiple nodes may transmit simultaneously for a single or even multiple receivers. As mentioned in the previous chapter, in the majority of wireless scenarios the characterization of the aggregate interference is a complex task, and due to the complexity of non-Gaussian modeling approaches, aggregate interference modeling in mobile scenarios have received limited attention.

This chapter characterizes the wireless interference of a mobile ad hoc network, where the nodes move according to the RWP model. The interferers are assumed to be located within an interference region, which is defined as a circular region centered in a fixed node located at a given point of the mobility scenario. The distribution of the interference is analyzed taking into account the stochastic nature of the path loss due to the mobility of the nodes, as well as fast fading and shadowing effects. The derivation of the CF of the aggregate interference is used in two different estimators, which successfully characterize the interference using only a small set of samples. Finally, the theoretical approach is validated through simulations, which confirm its effectiveness.

Chapter Contents

- **Section 3.2**: This section starts introducing the network scenario considered in the chapter. Then, the spatial distribution of the nodes for the square/rectangular scenario is derived. Finally, the section ends up describing the approximation of the inhomogeneous Poisson process (IPP) by multiple homogeneous PPPs with specific densities.

- **Section 3.3**: Derives a theoretical approximation for the aggregate interference distribution of the nodes located within an annulus, and the distribution of the aggregate interference when multiple annuli are considered.

- **Section 3.4**: Based on the models proposed in Section 3.3, this section describes two different estimation methodologies for the aggregate interference.
- **Section 3.5**: This section evaluates the proposed models, through the comparison of numerical and simulated results.
- **Section 3.6**: This section summarizes the achieved results.

3.2 System Description

In the analysis presented in this chapter we consider that nodes move according to the RWP mobility model [JM96]. In a RWP mobility scenario n nodes move in a region defined by the area $X_{max} \times Y_{max}$. Each node is initially placed in a random position (x, y). The position is sampled from the Uniform distributions represented by $x \sim U(0, X_{max})$ and $y \sim U(0, Y_{max})$. (x, y) represents the starting point. The ending point (x', y') is also uniformly chosen as the starting point (*i.e.* $x' \sim U(0, X_{max})$ and $y' \sim U(0, Y_{max})$). A node uniformly chooses the velocity $V \sim U(V_{min}, V_{max})$ to move from the starting point to the ending point. After reaching the ending point (x', y'), a node remains stopped at the ending point during the pause time, T_p. After elapsing T_p, a node uniformly chooses a new velocity value to move to another ending point uniformly chosen. After reaching the ending point a node repeats the same cycle as many times as required.

Considering that $\mathrm{E}[S]$ represents the expected distance between two random points and $\mathrm{E}[V_{wp}]$ represents the expected velocity of the nodes without considering pause, the expected velocity of the nodes considering pause is given by [Bet+03]

$$\mathrm{E}[V] = \left(\frac{\mathrm{E}[S]}{(\mathrm{E}[V_{wp}])^{-1}\mathrm{E}[S] + T_p} \right), \tag{3.1}$$

where $\mathrm{E}[V_{wp}] = \left(\frac{V_{max} - V_{min}}{\ln\left(\frac{V_{max}}{V_{min}}\right)} \right)$ is the expected velocity of the nodes for a null pause time ($T_p = 0$).

The scenario considered is depicted in Figure 3.1. A fixed node N_c is located at position (x_{N_c}, y_{N_c}), $x_{N_c} \sim U(0, X_{max})$ and $y_{N_c} \sim U(0, Y_{max})$, which operates as a fixed receiver of the mobile transmitting nodes. The main objective of this chapter is the characterization of the aggregate interference caused to N_c by the hypothetical transmitters (n) located within the interference region, i.e. the mobile transmitters located in the annulus bounded by the smaller circle of radius R_i^1 and the larger circle of radius R_o^L.

In multiple access networks, such as IEEE 802.11, IEEE 802.15.4 or LoRa, the nodes randomly access the channel. The proposed model considers random channel access by assuming that the transmitters access the channel with probability τ.

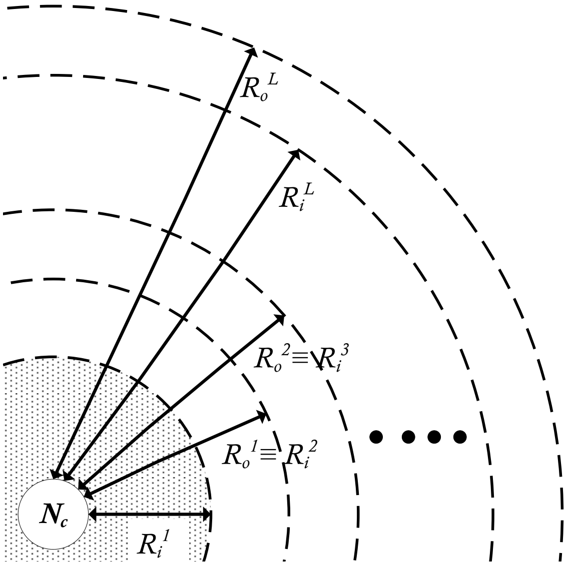

Figure 3.1: Aggregate interference caused to N_c due to the hypothetical mobile interferers located in the interference region with area $A = \pi\left((R_o^L)^2 - (R_i^1)^2\right)$.

3.2.1 Characterization of the Nodes' Distribution

The area $A = \pi\left((R_o^L)^2 - (R_i^1)^2\right)$ of the annulus in Figure 3.1 can be obtained via calculus by dividing the annulus up into an infinite number of annuli of infinitesimal width $d\chi$ and area $2\pi\chi$ $d\chi$ and then integrating from $\chi = R_i^1$ to $\chi = R_o^L$, i.e. $A = \int_{R_i^1}^{R_o^L} 2\pi\chi\, d\chi$. Using the Riemann sum, A can be approximated by the sum of the area of a finite number (L) of annuli of width ρ,

$$A \approx \sum_{l=1}^{L} A_l, \tag{3.2}$$

where $A_l = \pi\left((R_o^l)^2 - (R_i^l)^2\right)$ denotes the area of the annulus l. $R_o^l = (R_i^1 + l\rho)$ and $R_i^l = (R_i^1 + (l-1)\rho)$ represent the radius of the larger and smaller circles of the annulus l, respectively.

The number of nodes located in a specific annulus $l \in \{1,...,L\}$, represented by the RV X_l, is approximated by a Poisson process, being its Probability Mass Function (PMF) for a finite domain given by [PP02]

$$P(X_l = k) = \frac{\dfrac{(\lambda_l A_l \tau)^k}{k!} e^{-\lambda_l A_l \tau}}{\displaystyle\sum_{i=0}^{n} \frac{(\lambda_l A_l \tau)^i}{i!} e^{-\lambda_l A_l \tau}}, k = 0, 1, ..., n, \tag{3.3}$$

where λ_l is the nodes' spatial density in the annulus and n is the total number of mobile nodes.

The spatial PDF of the moving nodes in two dimensions x and y (denoted as $f_{X,Y}(x,y)$) is approximated by (see [Bet+03, Theorem 3.]),

$$f_{XY}(x,y) = \quad (p_s f_{init}(x,y) + p_p(1-p_s) + (1-p_s)(1-p_p) f_m(x,y))/a^2, \tag{3.4}$$

where $X, Y \in [0, a]$ with $a = X_{max} = Y_{max}$, p_s represents the probability that a node remains static for the entire simulation time, p_p is the probability that a node is resting at a randomly chosen time instant, p_s and $f_{init}(x,y)$ represents the initial spatial node distribution which is a Uniform distribution. The probability p_p is given as follows

$$p_p = \frac{(V_{max} - V_{min})T_p}{\ln\left(\frac{V_{max}}{V_{min}}\right)\mathrm{E}[S] + (V_{max} - V_{min})T_p}. \tag{3.5}$$

The asymptotically stationary PDF of the location of the nodes, $f_m(x,y)$, is given by [Bet+03],

$$\begin{aligned} &f_m(x,y) = \\ &= \begin{cases} f_m^*(x,y) & 0 < x \leq \frac{a}{2}, 0 < y \leq x \\ f_m^*(y,x) & 0 < x \leq \frac{a}{2}, x \leq y \leq \frac{a}{2} \\ f_m^*(a-y,x) & 0 < x \leq \frac{a}{2}, \frac{a}{2} \leq y \leq a-x \\ f_m^*(x,a-y) & 0 < x \leq \frac{a}{2}, a-x < y \leq a \\ f_m^*(a-x,y) & \frac{a}{2} \leq x < a, 0 < y \leq a-x \\ f_m^*(y,a-x) & \frac{a}{2} \leq x < a, a-x \leq y \leq \frac{a}{2} \\ f_m^*(a-y,a-x) & \frac{a}{2} \leq x < a, \frac{a}{2} \leq y \leq x \\ f_m^*(a-x,a-y) & \frac{a}{2} \leq x < a, x \leq y < a \\ 0, & \text{otherwise} \end{cases}, \end{aligned} \tag{3.6}$$

with

$$\begin{aligned} f_m^*(x,y) = &\frac{6y}{a} + \frac{3}{4}\left(\frac{a^2 - 2ax + 2x^2}{a^2}\right)\left(\frac{y}{y-a} + \frac{y^2}{(x-a)x}\right) + \frac{3y}{2a}\left[\left(\frac{2x}{a} - 1\right)\left(\frac{y}{a} + 1\right)\ln\left(\frac{a-x}{x}\right) + \right. \\ &\left. + \left(\frac{a^2 - 2ax + 2x^2 + ay}{a^2}\right)\ln\left(\frac{a-y}{y}\right)\right]. \end{aligned}$$

Knowing the spatial PDF defined in (3.4), the Bernoulli RV Z_a^l represents the hypothetical location of a node within the annulus l, and the event of a node being located within the annulus occurs with probability

$$\begin{aligned} P_l = P(Z_a^l = 1) = &\int_{(x_{N_c} - R_o^l)}^{(x_{N_c} + R_o^l)} \int_{\left(y_{N_c} - \sqrt{(R_o^l)^2 - (x - x_{N_c})^2}\right)}^{\left(y_{N_c} + \sqrt{(R_o^l)^2 - (x - x_{N_c})^2}\right)} f_{XY}(x,y)\,dy\,dx - \\ - &\int_{(x_{N_c} - R_i^l)}^{(x_{N_c} + R_i^l)} \int_{\left(y_{N_c} - \sqrt{(R_i^l)^2 - (x - x_{N_c})^2}\right)}^{\left(y_{N_c} + \sqrt{(R_i^l)^2 - (x - x_{N_c})^2}\right)} f_{XY}(x,y)\,dy\,dx. \end{aligned} \tag{3.7}$$

Consequently, the nodes' spatial density observed in the annulus l, λ_l, which is a missing parameter in (3.3), can be approximated by the expected number of nodes ($n\ P_l$) located in the area A_l, being represented by

$$\lambda_l \approx \frac{n\ P_l}{A_l}. \tag{3.8}$$

More details of the approximation (3.8) used in the Poisson PMF are given in Appendix A.

At this point, we highlight that the spatial distribution of the nodes ($f_{XY}(x,y)$) brings the specific aspects of the mobility of the nodes into the proposed model. In this way, the specifics of the RWP model and its parameterization are taken into account in $f_{XY}(x,y)$, as described in [Bet+03].

Finally, (3.3) can be used to approximate the distribution of the number of nodes located within each annulus l that approximate the area A. Because the area A may be composed by L areas, representing the area of each annulus l, in what follows we assume that the distribution of the number of nodes located within each annulus l is given by a Poisson process (with PMF represented in (3.3)). But since the density of nodes within each annulus varies, each annulus has its specific density (λ_l). In this way, we approximate the IPP describing the number of nodes in the area A through multiple homogeneous PPP (L) with specific densities.

To validate the proposed methodology, different values of λ_l were sampled from several simulations of a mobile scenario parameterized according the data contained in Table 3.1. The mobility of the nodes was simulated during 3000 s, which was enough to obtain a spatial distribution of the moving nodes close to the steady state distribution computed with (3.4). The results collected in 1000 simulations run with different random generator seeds, as well as the numerical results obtained with (3.8), are illustrated in Figure 3.2. The x-axis of the figure represents the radial distance from node N_c, which was positioned in the center of the simulated area, i.e. $x_{N_c} = y_{N_c} = 500$ m. Three different mobility scenarios were considered. The scenarios were parameterized with the common parameters presented in Table 1 and considering different pause durations (T_p) for each one. An average speed (E[V]) of 10.82 m/s was achieved for a pause time $T_p = 0$ s, E[V] = 3.52 m/s for $T_p = 100$ s and E[V] = 1.5 m/s for $T_p = 300$ s. Each marker in the figure represents the λ_l value adopted in each annulus (y-axis), being the width of each annulus (ρ) equal to 20 m ($R_i^1 = 0$ m, $R_o^1 = 20$ m, $R_i^2 = 20$ m, $R_o^2 = 40$ m, etc.). The x-axis represents the radial distance from the transmitter node N_c, being each λ_l value represented at the radial distance $R_i^l + \rho/2$. As can be shown, the proposed approximation for λ_l in (3.8) closely follows the results obtained by simulation. Consequently λ_l can be used to approximate the intensity of the IPP. Due to the spatial distribution of the nodes, we may observe that λ_l decreases as l increases. We can also observe that by increasing T_p the distribution of nodes becomes closer to a Uniform distribution (e.g. for E[V] = 1.50 m/s the different λ_l values become more similar).

Table 3.1: Parameters adopted in the simulations.

X_{max}	1000 m	Y_{max}	1000 m	Simul. Time	3000 s
V_{min}	5 m/s	V_{max}	20 m/s	τ	1
R_i^1	0 m	ρ	20 m	L	23
n	100	p_s	0	E[S]	≈ 521.4 m[Bet+03]

The assumption of the nodes being distributed according to a Poisson process within each annulus l was successfully validated. Figure 3.3 presents the results obtained through simulation

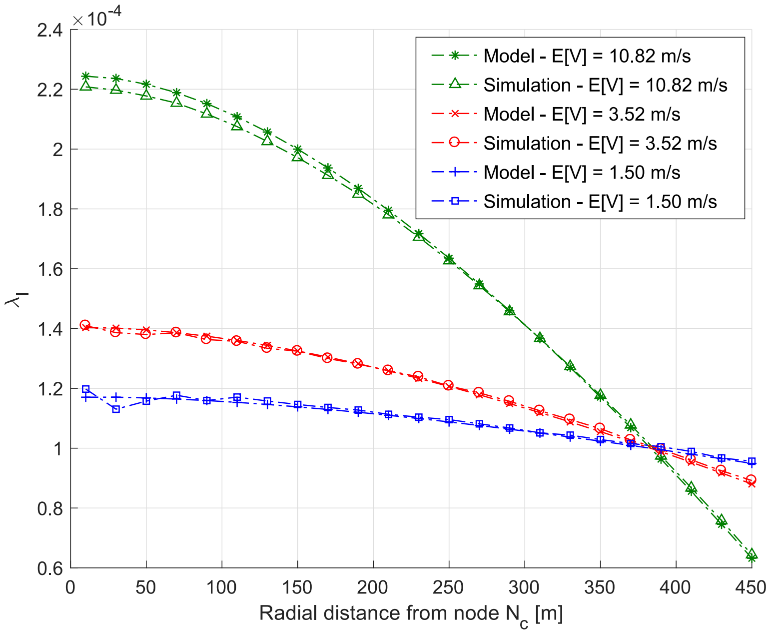

Figure 3.2: Validation of λ_l for $R_i^1 = 0$ m, $\rho = 20$ m and $L = 23$. The mobility scenario was parameterized according the data in Table 3.1.

and through the PMF in (3.3) for the mobility scenario considered in Figure 3.2 when $\mathrm{E}[V] = 10.82$ m/s. The λ_l values used in (3.3) were the ones computed and represented in Figure 3.2 for the same mobility scenario ($\mathrm{E}[V] = 10.82$ m/s). Different cumulative distribution functions CDFs are represented for the annulus $l = 2$ (R_i^2=20 m, R_o^2=40 m), $l = 4$ (R_i^4=60 m, R_o^4=80 m), $l = 16$ (R_i^{16}=300 m, R_o^{16}=320 m) and $l = 23$ (R_i^{23} =440 m, R_o^{23}=460 m). As can be seen the Poisson distribution accurately approximates the distribution of the number of the nodes within each annulus.

3.3 Characterization of the Aggregate Interference

The characterization of the aggregate interference assumes that the interference is sampled periodically. Consequently, different values of mobility of the nodes (e.g. $\mathrm{E}[V]$) lead to different aggregate interference values (e.g. average aggregate interference) when the sampling period is maintained constant. In this section we start to characterize the interference caused to N_c by the nodes located within a generic annulus l (Subsection 3.3.1). Finally, we study the interference caused by the nodes located within L annuli (Subsection 3.3.2), providing an efficient method to compute the distribution of the aggregate interference power (Subsection 3.3.3).

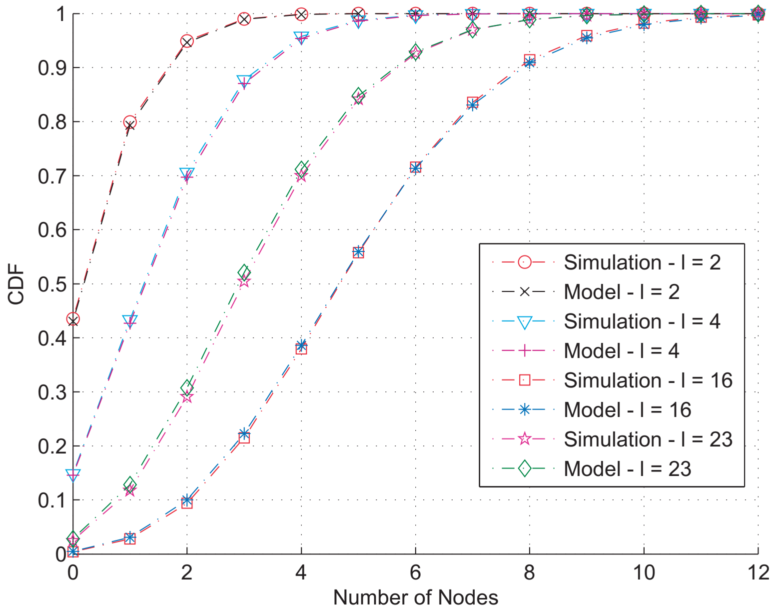

Figure 3.3: Validation of $P(X_l \leq k)$ for the mobility scenario $\mathrm{E}[V] = 10.82$ m/s considered in Figure 3.2.

3.3.1 Interference due to interferers located within the annulus l

The total interference power received/sampled by the node N_c located in the center of an annulus l is expressed by

$$I = \sum_{i=1}^{n_l} I_i, \tag{3.9}$$

where I_i is the interference caused by the i-th node, and n_l is the total number of nodes located in the annulus. The interference power I_i is given by

$$I_i = P_{Tx}\psi_i r_l^{-\wp}, \tag{3.10}$$

where P_{Tx} is the transmitted power level of the i-th node[1], ψ_i is an instant value of the fading and shadowing gain observed in the channel between the receiver and node i. r_l represents the distance between the i-th interferer and the receiver. The values r_l and ψ_i represent instant values of the RVs R_l and Ψ_i, respectively. $\wp$ represents the path-loss coefficient. It should be pointed out that no power control is applied.

In the next steps we derive the MGF of the aggregate interference due to path loss. To characterize the distribution of Ψ_i the small-scale fading (fast fading) and shadowing (slow fading) effects must be considered. The amplitude of the small-scale fading effect is assumed to be distributed according to a Rayleigh distribution, which is represented by

$$f_\zeta(x) = \frac{x}{\sigma_\zeta^2} e^{\frac{-x^2}{2\sigma_\zeta^2}}, \tag{3.11}$$

---

[1] $P_{Tx} = 10^3$ mW is assumed for each node.

where x is the envelope amplitude of the received signal. $2\sigma_\zeta^2$ is the mean power of the multipath received signal. $2\sigma_\zeta^2 = 1$ is adopted in this analysis to consider the case of normalized power.

Regarding the shadowing effect, we have assumed that its power follows a Lognormal distribution

$$f_\xi(x) = \frac{1}{\sqrt{2\pi}\sigma_\xi x} e^{\frac{-(ln(x)-\mu_\xi)^2}{2\sigma_\xi^2}}, \tag{3.12}$$

with parameters μ_ξ and σ_ξ. To obtain unitary mean we only parametrize $\sigma_\xi > 0$ and μ_ξ is given by $\mu_\xi = -\frac{\sigma_\xi^2}{2}$.

Although (3.12) appears to be a simple expression, it is often inconvenient when further analysis are required. Consequently, [AK99] has shown that the Lognormal distribution can be accurately approximated by a Gamma distribution, defined by

$$f_\xi(x) \approx \frac{1}{\Gamma(\vartheta)} \left(\frac{\vartheta}{\omega_s}\right)^{\vartheta} x^{\vartheta-1} e^{-x\frac{\vartheta}{\omega_s}}, \tag{3.13}$$

where ϑ is equal to $\frac{1}{e^{\sigma_\xi^2}-1}$ and ω_s is equal to $e^{\mu_\xi}\sqrt{\frac{\vartheta+1}{\vartheta}}$. $\Gamma(.)$ represents the Gamma function. The PDF of Ψ_i is thus represented by

$$f_{\Psi_i}(x) \approx f_{\zeta^2}(x) \cdot f_\xi(x) \approx \frac{2}{\Gamma(\vartheta)} \left(\frac{\vartheta}{\omega_s}\right)^{\frac{\vartheta+1}{2}} x^{\frac{\vartheta-1}{2}} K_{\vartheta-1}\left(\sqrt{\frac{4\vartheta x}{\omega_s}}\right), \tag{3.14}$$

which is the Generalized-K distribution, where $K_{\vartheta-1}(\cdot)$ is the modified Bessel function of the second kind.

Due to the analytical difficulties of the Generalized-K distribution, an approximation of the PDF (3.14) by a more tractable PDF is needed. [AAY10] proposes an approximation of the Generalized-K distribution through a Gamma distribution (the moment matching method was adopted in the approximation). With this method, [AAY10] shows that the scale (θ_ψ) and shape (k_ψ) parameters of the Gamma distribution are given by

$$\theta_\psi = \left(\frac{2(\vartheta+1)}{\vartheta} - 1\right)\omega_s \tag{3.15}$$

and

$$k_\psi = \frac{1}{\frac{2(\vartheta+1)}{\vartheta} - 1}, \tag{3.16}$$

respectively.

Let $M_I^i(s)$ represent the MGF of the i-th interferer located within the annulus ($i = 1,...,n_l$) given by

$$M_I^i(s) = \mathrm{E}_{I_i}[e^{sI_i}] = \mathrm{E}_{\Psi_i}\left[\mathrm{E}_{R_l}[e^{sI_i}]\right]. \tag{3.17}$$

The PDF of R_l can be written as the ratio between the perimeter of the circle with radius x and the total area A_l, being represented as follows

$$f_{R_l}(x) = \begin{cases} \frac{2\pi x}{A_l} & R_i^l < x < R_o^l. \\ 0, & otherwise \end{cases} \tag{3.18}$$

Using the PDF of the distance given in (3.18) and the PDF of the small-scale fading and shadowing effects in (3.14), the MGF of the interference received by the node N_c due to the i-th interferer node in (3.17) can be written as follows

$$M_I^i(s) = \int_0^{+\infty} \int_{R_i^l}^{R_o^l} e^{sI_i} f_{R_l}(r_l) f_{\Psi_i}(\psi_i) \, dr_l \, d\psi_i, \tag{3.19}$$

which using (3.10), (3.15), (3.16), and (3.18) can be simplified to

$$M_I^i(s) = \frac{2\pi}{A_l(2+k_\psi\wp)(P_{Tx}\theta_\psi s)^{k_\psi}} \cdot \left(\left(R_o^l\right)^{2+k_\psi\wp} \varrho(R_o^l) - \left(R_i^l\right)^{2+k_\psi\wp} \varrho(R_i^l) \right), \tag{3.20}$$

where

$$\varrho(x) = {}_2\mathrm{F}_1\left(k_\psi, k_\psi + \frac{2}{\wp}, 1 + k_\psi + \frac{2}{\wp}, -\frac{x^\wp}{P_{Tx}\theta_\psi s}\right),$$

and ${}_2\mathrm{F}_1$ represents the Gauss Hypergeometric function [AS65].

Assuming that the individual interference I_i is independent and identically distributed when compared to the other interferers, the PDF of the aggregate interference I given a total of k active interferers is the convolution of the PDFs of each I_i. Following this rationale, the MGF of I is given by

$$M_{I/k}(s) = M_I^1(s) \times M_I^2(s) \times \cdots \times M_I^k(s) = \left(M_I^i(s)\right)^k. \tag{3.21}$$

Using the law of total probability, the PDF of the interference I can be written as

$$f_I(j) = \sum_{k=0}^{n} f_I(j|X_l = k)\mathrm{P}(X_l = k), \tag{3.22}$$

leading to the MGF of the aggregate interference, I, which can be written as

$$\mathrm{E}[e^{sI}] = \sum_{k=0}^{n} \mathrm{P}(X_l = k) \int_{-\infty}^{+\infty} e^{sj} f_I(j|X_l = k) \, dj = \sum_{k=0}^{n} \mathrm{P}(X_l = k) M_{I/k}(s). \tag{3.23}$$

Using (3.21), the MGF of I is given as follows

$$\mathrm{E}[e^{sI}] = \sum_{k=0}^{n} \mathrm{P}(X_l = k) e^{k \, ln(M_I^i(s))}. \tag{3.24}$$

Using the MGF of the Poisson distribution in (3.24), the MGF of I is finally given by

$$\mathrm{E}[e^{sI}] = e^{\lambda_l A_l \tau (M_I^i(s) - 1)}. \tag{3.25}$$

The first- and second-order statistics of the aggregate interference caused to N_c by the nodes located within the annulus l are an important feature. $\mathrm{E}[I]$, the expected value of the aggregate interference, can be determined by using the Law of Total Expectation. It can be shown that

$$\mathrm{E}[I] = \mathrm{E}\Big[\mathrm{E}\big[I|X_l\big]\Big] = \mathrm{E}\big[I_i\big]\mathrm{E}\big[X_l\big] = 2\pi\lambda_l\tau P_{Tx} e^{\mu_\xi} \sqrt{e^{\sigma_\xi^2}} \left(\frac{(R_o^l)^{2-\wp} - (R_i^l)^{2-\wp}}{2-\wp} \right). \tag{3.26}$$

Making similar use of the Law of Total Variance, the variance of the aggregate interference can be described as

$$\mathrm{Var}[I] \quad = \mathrm{Var}[I_i]\mathrm{E}[X_l] + \mathrm{E}[I_i]^2\mathrm{Var}[X_l]. \tag{3.27}$$

Since X_l is given by a Poisson distribution (with mean and variance $\lambda_l A_l \tau$), the variance of the aggregate interference is given as follows

$$\mathrm{Var}[I] \quad = \lambda_l A_l \tau \left(\frac{\partial^2 M_I^i(0)}{\partial s^2} \right) = \pi \lambda_l \tau P_{Tx}^2 k_\psi \theta_\psi^2 (1 + k_\psi) \left(\frac{(R_o^l)^{2-2\wp} - (R_i^l)^{2-2\wp}}{1 - \wp} \right). \tag{3.28}$$

The first and second moments can be matched with the respective moments of a given distribution to obtain an approximation of the aggregate interference. As shown in [HG09], the aggregate interference due to path loss, fast fading and shadowing effect can be approximated by a Gamma distribution. Consequently, the shape and the scale parameters of the Gamma distribution, denoted by k_l and θ_l, are respectively given by

$$k_l = \mathrm{E}[I]^2/\mathrm{Var}[I], \tag{3.29}$$

and

$$\theta_l = \mathrm{Var}[I]/\mathrm{E}[I]. \tag{3.30}$$

3.3.2 Interference due to interferers located within L annuli

As shown before, the interference I caused by interferers located within the l-th annulus is approximated by a Gamma distribution, with MGF

$$M_{I/K}^l(s) = (1 - \theta_l s)^{-k_l}. \tag{3.31}$$

Since the annulus of width $R_o^L - R_i^1$ where the interferers are located can be expressed as a summation of L annuli of width ρ, the MGF of the aggregate interference caused by the interferers located within the L annuli is given by

$$M_{I_{agg}}(s) = \prod_{l=1}^{L} (1 - \theta_l s)^{-k_l}. \tag{3.32}$$

Finally, the expectation of the aggregate interference can be computed as follows

$$\mathrm{E}[I_{agg}] = \frac{\partial M_{I_{agg}}(0)}{\partial s}. \tag{3.33}$$

3.3.3 Distribution of the aggregate interference

The aggregate interference may be stated as being the summation of the L individual aggregated interference caused by the nodes located within each annulus. Expressions for the PDF and the CDF of the summation of L independent Gamma RVs were initially derived by Mathai in [Mat82]. Those were simplified in [Mos85] in order to be computed more efficiently.

Let $\{Z_l\}_{l=1}^{L}$ be independent but not necessarily identically distributed Gamma variables with parameters k_l (shape) and θ_l (scale). The PDF of the aggregate interference is written as $I_{agg} = \sum\limits_{l=1}^{L} Z_l$, which can be approximated by [Mos85]

$$f_{I_{agg}}(x) \approx \prod_{l=1}^{L}\left(\frac{\theta_1}{\theta_l}\right)^{k_l} \sum_{w=0}^{+\infty} \frac{\delta_w\, x^{(\sum_{l=1}^{L} k_l+w-1)} \exp\left(-\frac{x}{\theta_1}\right)}{\theta_1^{(\sum_{l=1}^{L} k_l+w)}\, \Gamma\left(\sum_{l=1}^{L} k_l+w\right)}, \tag{3.34}$$

where $\theta_1 = \min\limits_{l}\{\theta_l\}$, δ_w coefficients are computed recursively,

$$\delta_{w+1} = \frac{1}{w+1}\sum_{i=1}^{w+1}\left[\sum_{l=1}^{L} k_l \left(1-\frac{\theta_1}{\theta_l}\right)^{i}\right]\delta_{w+1-i},$$

and $\delta_0 = 1$. $\Gamma(.)$ is the Gamma function. Finally, the CDF of I_{agg}, $F_{I_{agg}}(x) = \int\limits_{-\infty}^{x} f_{I_{agg}}(z)dz$, is computed as follows [Mos85]

$$F_{I_{agg}}(x) \approx \prod_{l=1}^{L}\left(\frac{\theta_1}{\theta_l}\right)^{k_l} \sum_{w=0}^{\infty} \frac{\delta_w}{\theta_1^{\sum_{l=1}^{L} k_l+w}\, \Gamma\left(\sum_{l=1}^{L} k_l+w\right)} \times \int\limits_{0}^{x} z^{\sum\limits_{l=1}^{L} k_l+w-1} \exp\left(-\frac{z}{\theta_1}\right)dz. \tag{3.35}$$

The computation of $f_{I_{agg}}(x)$ and $F_{I_{agg}}(x)$ can also be performed in a more efficient way using the Fast Fourier Transform (FFT) algorithm, instead of using (3.34) and (3.35). Since the annulus of width $R_o^L - R_i^1$ where the mobile nodes are located can be described as a sum of L annuli of width ρ, the CF of the aggregate interference (I_{agg}) received from the mobile nodes is given by

$$\varphi_{I_{agg}}(t) = \prod_{l=1}^{L}(1-\theta_l i t)^{-k_l}. \tag{3.36}$$

Using the Fourier transform, the PDF of the aggregate interference is given as follows,

$$f_{I_{agg}}(x) = \frac{1}{2\pi}\int_{-\infty}^{+\infty} e^{-itx}\varphi_{I_{agg}}(t)dt, \tag{3.37}$$

which can be numerically calculated using a FFT algorithm. Finally, the CDF of the aggregate interference is given by

$$F_{I_{agg}}(x) = \int_{-\infty}^{x} f_{I_{agg}}(z)dz. \tag{3.38}$$

3.4 Interference Estimation

This subsection starts with the assumption that the aggregate interference can be approximated by a GEV distribution [Mur+11]. This assumption was based on sampled data obtained through simulation, which was used in different goodness of fit tests to identify the theoretical distributions that better approximate the empirical distribution of the sample data. The results presented in Section 3.5 validate our assumption and show the accuracy of the approximation.

The PDF of a GEV distribution is represented by

$$f(x;\sigma,\gamma,\mu) = \frac{1}{\sigma}t(x)^{\gamma+1}e^{-t(x)}, \tag{3.39}$$

where

$$t(x) = \begin{cases} \left(1+\gamma\dfrac{x-\mu}{\sigma}\right)^{-1/\gamma}, & \gamma \neq 0 \\ e^{-(x-\mu)/\sigma}, & \gamma = 0 \end{cases}. \tag{3.40}$$

With the help of two estimators we plan to estimate the parameters σ, γ and μ of the GEV distribution. To this end, a MLE estimator and a PWM estimator are introduced next, in order to be used in real-time to estimate the aggregate interference. Hereafter, we represent the interference sample set by $\mathcal{X} = \{S_1, S_2, ..., S_m\}$, where $S_1, S_2, ..., S_m$ are the samples periodically acquired by the node N_c. The ordered sample set is denoted by $\mathcal{X}_s = \{S_{1,m}, S_{2,m}, ..., S_{m,m}\}$, where $S_{1,m} \leq S_{2,m} \leq ... \leq S_{m,m}$.

3.4.1 MLE

The log-likelihood function for a sample set $\mathcal{X} = \{S_1, ..., S_m\}$ of i.i.d. GEV RVs is given by

$$\log L(\sigma,\gamma,\mu) = -m\log\sigma - \left(\frac{1}{\gamma}+1\right)\sum_{i=1}^{m}\log\left(1+\gamma\frac{S_i-\mu}{\sigma}\right) - \sum_{i=1}^{m}\log\left(1+\gamma\frac{S_i-\mu}{\sigma}\right)^{-1/\gamma}, \tag{3.41}$$

under the condition $1+\gamma\frac{S_i-\mu}{\sigma} > 0$. The MLE estimator $(\hat{\sigma},\hat{\gamma},\hat{\mu})$ for (σ,γ,μ) is obtained by maximizing (3.41).

3.4.2 PWM Estimator

As described in [Gre+79], the PWM of a RV X with distribution function $F(X) = P(X \leq x)$ are the quantities

$$M_{p,r,s} = \mathrm{E}[X^p(F(X))^r(1-F(X))^s], \tag{3.42}$$

for real p, r and s values. For the GEV distribution, [Hos+85] shows that $\mathrm{E}[X(F(X))^r]$ can be written as

$$M_{1,r,0} = \frac{1}{r+1}\left\{\mu - \frac{\sigma}{\gamma}[1-(r+1)^{\gamma}\Gamma(1-\gamma)]\right\}, \tag{3.43}$$

with $\gamma < 1$ and $\gamma \neq 0$. The PWM estimators $(\hat{\sigma}, \hat{\gamma}, \hat{\mu})$ of the GEV parameters (σ, γ, μ) are the solution of the following system of equations

$$\begin{cases} M_{1,0,0} = \mu - \frac{\sigma}{\gamma}(1-\Gamma(1-\gamma)) \\ 2M_{1,1,0} - M_{1,0,0} = \frac{\sigma}{\gamma}\Gamma(1-\gamma)(2^{\gamma}-1) \\ \dfrac{3M_{1,2,0}-M_{1,0,0}}{2M_{1,1,0}-M_{1,0,0}} = \dfrac{3^{\gamma}-1}{2^{\gamma}-1} \end{cases}, \tag{3.44}$$

in which $M_{1,r,0}$ can be replaced by the unbiased estimator proposed in [Lan+79]

$$\hat{M}_{1,r,0} = \frac{1}{m} \sum_{j=1}^{m} \left(\prod_{l=1}^{r} \frac{j-l}{m-l} \right) S_{j,m}. \tag{3.45}$$

3.5 Model Evaluation

Several simulations were parameterized according the data in Table 3.2 to validate the average aggregate interference. A mobility region consisting of a square area of 1000x1000 m was defined where the nodes move with $V_{min} = 5$ m/s and $V_{max} = 20$ m/s. Different mobility scenarios were considered: an average speed (E$[V]$) of 10.82 m/s was achieved for a pause time $T_p = 0$ s; a second scenario was defined with E$[V] = 3.52$ m/s adopting $T_p = 100$ s; and a third scenario was defined to obtain E$[V] = 1.5$ m/s considering $T_p = 300$ s. The aggregate interference was sampled every second and 3×10^6 simulations were run.

Table 3.2: Parameters adopted in the simulations.

X_{max}	1000 m	Y_{max}	1000 m	p_s	0 s
V_{min}	5 m/s	V_{max}	20 m/s	τ	1
R_i^1	20 m	ρ	20 m	L	5
Simulation time	3000 s	$\wp$	2	σ_ξ	0.69

To evaluate the proposed model of the aggregate interference we compare the numerical results obtained with the model and the results obtained through simulation. The CDF of the aggregate interference is illustrated in Figure 3.4 and Figure 3.5 for a simulation scenario considering $n = 100$ mobile nodes. The receiver node N_c was positioned in the center of the simulation area, i.e. $x_{N_c} = y_{N_c} = 500$ m. The aggregate interference was measured by the node N_c every second. In Figure 3.4 only the path loss effect was considered, while the results plotted in Figure 3.5 were obtained considering path loss, fast fading and shadowing effect, for $\sigma_\xi = 0.69$. The numerical results were obtained with (3.35) considering the first 25 terms in the infinite sum series, i.e, $w = 25$.

As shown in both Figures 3.4 and 3.5, the error observed between the model and the simulations is in range with the error bound given in [Mos85] for the case when the approximation in (3.35) is adopted. Different CDFs are obtained for the three mobility scenarios (E$[V]$ =10.82 m/s, E$[V]$ = 3.52 m/s and E$[V] = 1.5$ m/s), indicating that an increase of T_p leads to a decrease of the aggregate interference power, or in other words, the interference power increases with the average speed of the nodes. This fact is due to the decrease of the node's density near to the node N_c as T_p increases, which is also confirmed by the theoretical analysis in [Bet+03] and the values of λ_l represented in Figure 3.2. As the average pause time increases, the spatial distribution of the nodes converges to a Uniform distribution, and a smaller number of nodes is located in the vicinity of N_c, causing less

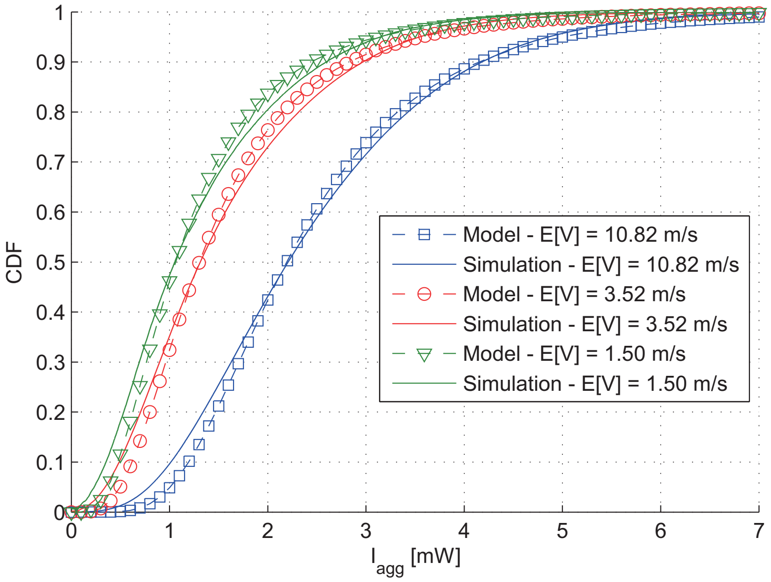

Figure 3.4: CDF of the aggregate interference considering the path loss effect ($\tau = 1$).

interference to N_c. Contrarily, the increase of the mobility increases the average number of nodes in the vicinity of N_c, causing more interference to N_c.

Comparing the results plotted in Figures 3.4 and 3.5(a), we observe that when small-scale fading and shadowing are considered, the average interference power remains approximately the same because small-scale fading and shadowing are parametrized for unitary mean.

The proposed model can handle the case when nodes transmit with a given probability, τ. τ can represent the medium access probability of a specific random medium access control (MAC) protocol (e.g. Slotted Aloha), or even the behavior imposed by fair resource management policies. Different medium access probabilities (τ) were considered in the results presented in Figure 3.5(b). We have considered the high mobility scenario (E$[V]$ =10.82 m/s) and the same parameters adopted in the results presented in Figure 3.5(a). The simulations were modified to consider that the interference power received from each mobile node is null when a number randomly (uniformly) generated at each discrete simulation time is above τ. In this way the mobile nodes only contribute to the aggregate interference according to τ. From the validation results, presented in Figure 3.5(a), we observe that the proposed model also approximates the CDF of the aggregate interference for different τ values. Moreover, the interference power decreases as $\tau \rightarrow 0$, as expected.

While the results obtained in Figures 3.4 and 3.5 were obtained considering that the receiver node N_c was positioned in the center of the simulation, in Figure 3.6 we evaluate the accuracy of the proposed model for different positions of N_c. The evaluation was done at positions $(x_{N_c}, y_{N_c}) = \{(200, 300)(500, 500), (600, 700), (800, 800)\}$ m. We have considered the high mobility scenario (E$[V]$ =10.82 m/s) and the same parameters adopted in the results presented in Figure 3.5(a). As can be observed, the results computed with the model are close to the results obtained through simulation. Moreover, we also observe that the aggregate interference decreases as the node N_c is further away from the center of the simulated area ((x, y) = (500, 500) m). This is explained by the higher density of mobile nodes in the center of the simulation area, as observed in Figure

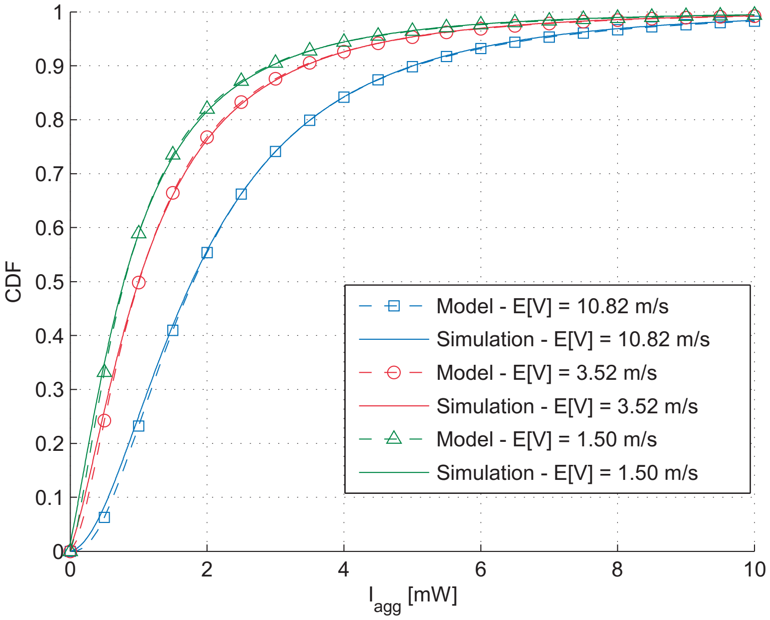

(a)

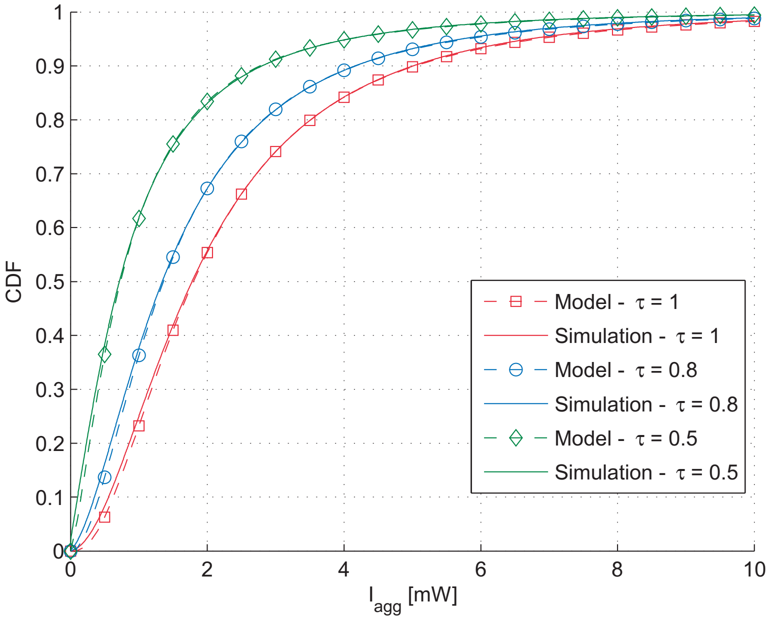

(b)

Figure 3.5: CDF of the aggregate interference considering path loss, small-scale fading and shadowing effect ($\sigma_{\xi} = 0.69$): (a) for $\tau = 1$ and $\mathrm{E}[V] = \{1.5, 3.52, 10.82\}$ m/s; (b) for $\tau = \{0.5, 0.8, 1\}$ and $\mathrm{E}[V] = 10.82$ m/s.

3.2. Consequently, as N_c is further away from the center of the simulated area less mobile nodes (interferers) are found in the same circular area ($R_i^1 = 20$ m and $R_o^L = 120$ m).

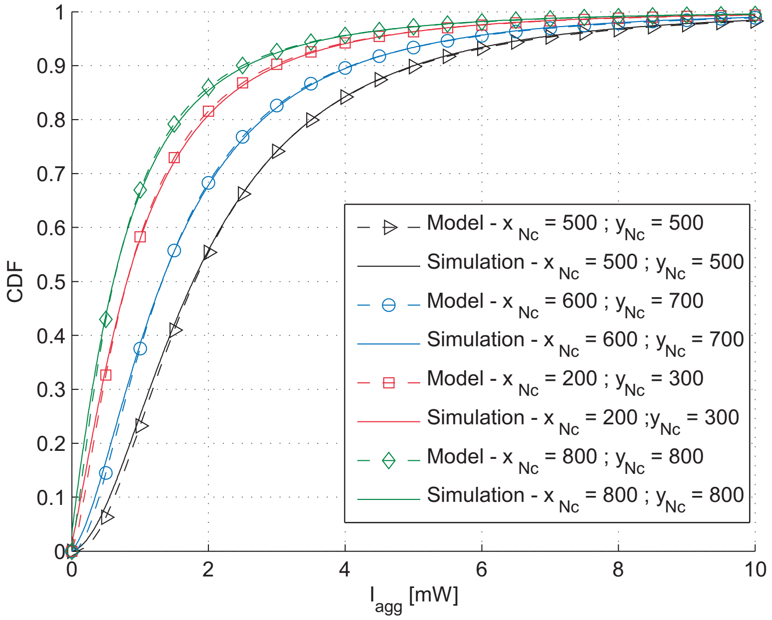

Figure 3.6: CDF of the aggregate interference for different positions (x_{Nc}, y_{Nc}) of the receiver node N_c.

Figure 3.7 compares the simulation results with the numerical results obtained for different values of L. Regarding the parameterization of L, both model's accuracy and model's computation time increase with L. However, different simulation results were used to evaluate the accuracy of the model when $L \geq 5$, confirming its effectiveness even for low values of L.

Next, we assess the accuracy of the proposed estimators. Considering the same radio conditions and the two mobility scenarios (E$[V]$ =10.82 m/s and E$[V]$ = 1.5 m/s) assumed in Figure 3.5(a), we computed the CDF of the aggregate interference with the PWM estimator and the MLE. The length of the sample set was $m = 100$. As can be seen in Figure 3.8, which represents the CDFs obtained by simulation and computed by maximizing (3.41) (MLE) and solving (3.44) (PWM), the results achieved with the proposed estimators are close to the results obtained by simulation. In this case the error obtained with the MLE or with the PWM estimator is similar. This fact is mainly due to the length of the sample set (m), as we will see later.

To evaluate the impact of the length of the sample set in the estimation, we have considered the mobility E$[V]$ =10.82 m/s, being the aggregate interference estimated with the PWM estimator considering $m = 50$, $m = 10$, and $m = 5$ samples. The simulation results and the results achieved with the PWM estimator considering the different m values are illustrated in Figure 3.9. As expected, a larger set of samples allows more accurate results. However, we would like to highlight the quality of the estimation even when a small set of samples (m =10) is adopted. These results confirm the quality of the proposed model and estimator, highlighting the importance in terms of its practical application.

Additionally, we note that the aggregate interference follows a GEV distribution, as confirmed

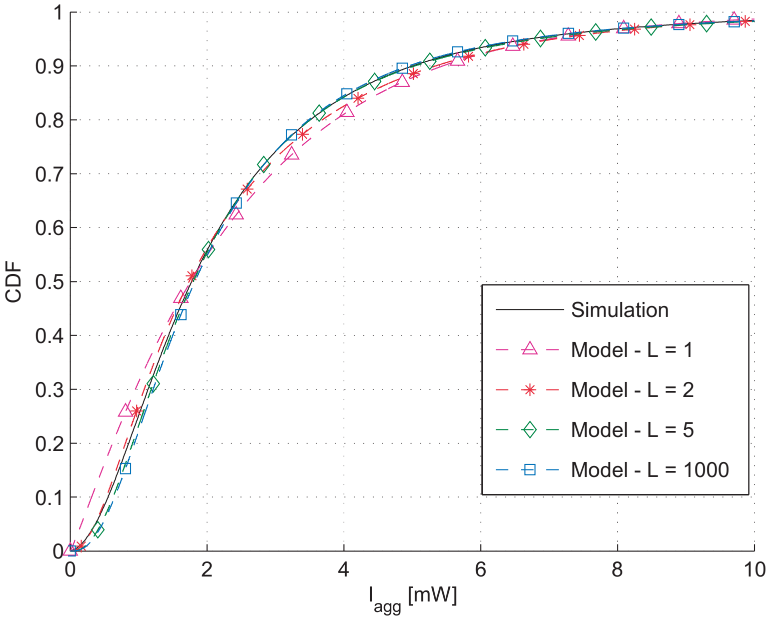

Figure 3.7: CDF of the aggregate interference considering path loss, small-scale fading and shadowing effect ($\sigma_\xi = 0.69$), for $L = \{1, 2, 5, 1000\}$, $\mathrm{E}[V] = 10.82$ m/s, $\tau = 1$ and $x_{N_c} = y_{N_c} = 500$ m.

by the estimation results presented in Figures 3.8 and 3.9.

As a final remark, although the interferers considered in the results presented in Figures 3.4, 3.5, 3.6, 3.8 and 3.9, were always located within an annulus parameterized with $R_i^1 = 20$ m and $R_o^L = 120$ m, we note that the model (and the estimation methodology) was also successfully validated for other R_i^1 and R_o^L values, including the particular case when all moving nodes are considered, i.e. R_i^1=0 m and $R_o^L \geq \sqrt{(X_{max}/2)^2 + (Y_{max}/2)^2}$ for the cases when N_c is positioned at $x_{N_c} = y_{N_c} = 500$ m.

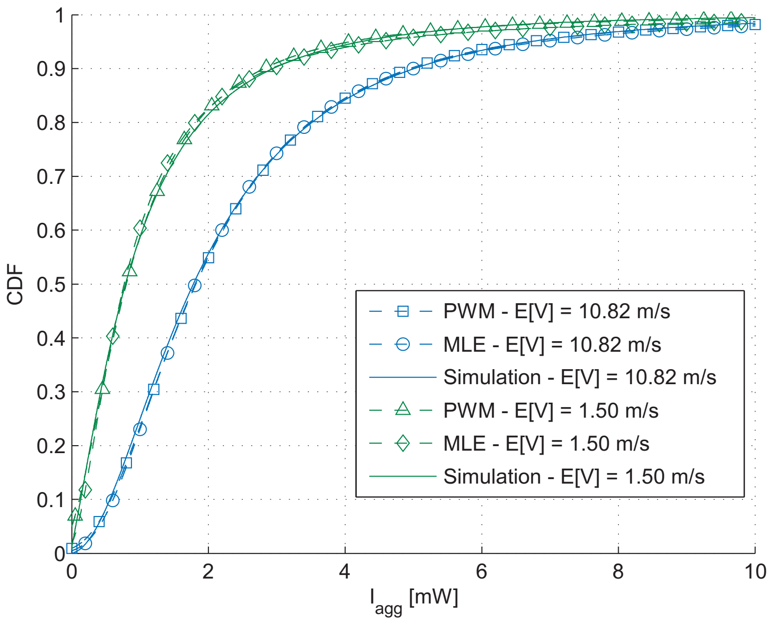

Figure 3.8: Estimation of the aggregate interference through the PWM estimator and the MLE (m =100 samples), considering path loss, fading and shadowing effects for two mobility scenarios (E[V] =10.82 m/s and E[V] = 1.5 m/s, τ = 1).

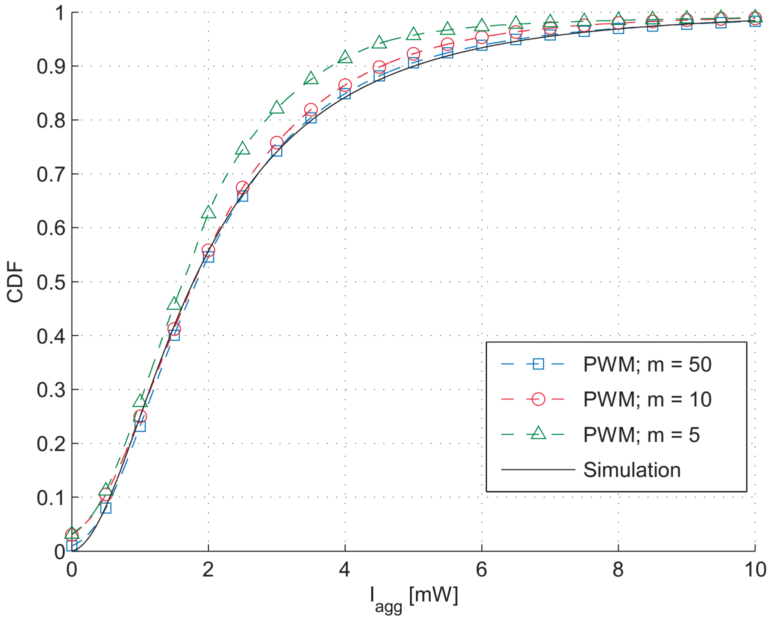

Figure 3.9: Estimation of the aggregate interference through the PWM considering different lengths of the sampling set ($m = \{50, 10, 5\}$) for the mobility scenario E[V] =10.82 m/s (τ = 1).

3.6 Conclusions

This chapter characterized the wireless interference caused by a mobile network, when the nodes move according to the RWP model. Assuming a time-varying wireless channel due to slow and fast fading and, considering the dynamic path loss due to the mobility of the nodes, we have characterized the interference distribution caused to a receiver by the moving interferers located in a ring. After that, the distribution of the aggregate interference caused to a tagged receiver by moving interferers located within an interference region was characterized. Results from several simulations were compared with the theoretical characterization, showing the accuracy of the proposed methodology.

The simulation results confirmed that the distribution of the aggregated interference may be accurately approximated by a GEV distribution. Based on the interference distribution, two different methodologies (MLE and PWM) were assessed to estimate the interference. The accuracy of the results achieved with the proposed methodologies show that they may be used as an effective tool of interference estimation in future wireless communication systems. Moreover, the low number of required samples constitutes one of the advantages of the proposed PWM estimator.

CHAPTER 4

RESIDUAL SELF-INTERFERENCE POWER IN IN-BAND FULL-DUPLEX WIRELESS SYSTEMS

4.1 Introduction

Motivated by the importance of the analog SI's characterization in the joint cancellation process, this chapter derives a theoretical analysis of the residual SI power, i.e., the amount of uncanceled SI due to channel estimation errors at the analog cancellation process. The need of analog and digital-domain cancellation requires a precise characterization of the amount of interference not canceled in the analog-domain. The knowledge of the residual SI due to the AC is crucial to design efficient SI estimation methods to be used in the digital-domain. By doing so, the efficiency of the joint AC and DC schemes may be improved.

In this chapter, the distribution of the residual SI power in an analog post-mixer canceler is characterized, which represents the amount of uncanceled SI due to imperfect SI channel estimation and imperfections in the transmission chain [Kor+14a]. Closed form expressions are derived for the distribution of the residual SI power when Rician and Rayleigh fading SI channels are considered. The distribution of the residual SI power is also derived for low and high channel gain dynamics, by considering the cases when the SI channel gain is time-invariant and time-variant. Different simulation results to show the influence of the channel dynamics on the distribution of the SI power are presented, where numerical results computed with the proposed model are compared with Monte Carlo simulation results to evaluate the accuracy of the theoretical analysis for both SI channel's gain and phase estimation errors. The accuracy of the theoretical analysis is also assessed for the limit case when the frequency of the input signal to be transmitted is close to the carrier frequency. Finally, the impact of the PN is evaluated through Monte Carlo simulation results for different values of PN variance.

Chapter Contents

- **Section 4.2**: This section introduces the assumptions made regarding the system model in the chapter.
- **Section 4.3**: Describes the steps involved in the theoretical characterization of the residual SI power.
- **Section 4.4**: Presents the accuracy of the proposed methodology, where numerical results computed with the proposed model and Monte Carlo simulation results are compared.
- **Section 4.5**: Concludes the chapter by outlining its contribution.

4.2 System Model

In this chapter, a IBFDX scheme adopting an active analog canceler that reduces the SI at the carrier frequency is considered. The active analog canceler actively reduces the SI by injecting a canceling signal into the received signal. A post-mixer canceler is assumed, because the canceling signal is generated by processing the SI signal after the upconversion stage [Sah+13]. The block diagram of the system model is shown in Figure 4.1.

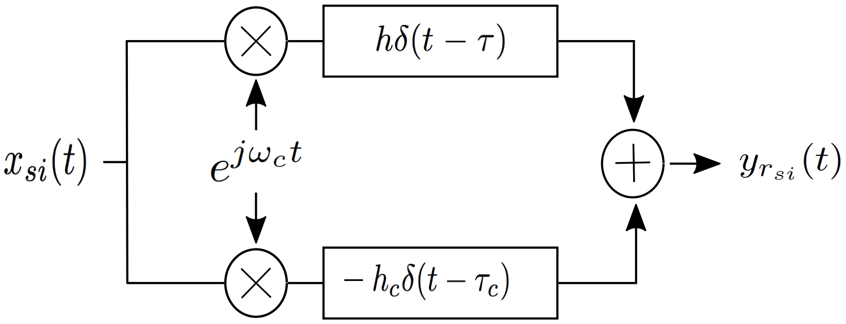

Figure 4.1: Block diagram representation of the post-mixer canceller.

The SI signal $x_{si}(t)$ is up-converted to the frequency $\omega_c = 2\pi f_c$ and transmitted over the IBFDX channel characterized by the gain h and the delay τ. In this chapter, is considered that the active analog canceler estimates the channel's gain and delay in order to reduce the residual SI $y_{r_{si}}(t)$.

The residual SI, $y_{r_{si}}(t)$, is represented as follows

$$y_{r_{si}}(t) = x_{si}(t)e^{j\omega_c t} * \mathbf{h}_{si}(t) - x_{si}(t)e^{j\omega_c t} * \hat{\mathbf{h}}_{si}(t), \tag{4.1}$$

where $x_{si}(t)$ is the SI signal, $\mathbf{h}_{si}(t)$ is the impulse response of the SI channel, $\hat{\mathbf{h}}_{si}(t)$ represents the estimate of the SI channel, ω_c is the angular frequency and $*$ represents the convolution operation. The SI channel considered in this chapter is a single-tap delay channel, i.e., $\mathbf{h}_{si}(t) = h\delta(t-\tau)$. Similarly, the estimate of the SI channel is denoted by $\hat{\mathbf{h}}_{si}(t) = h_c\delta(t-\tau_c)$, where h_c and τ_c are the estimated SI channel's gain and delay, respectively.

It is assumed that the SI signal, $x_{si}(t)$, is a circularly-symmetric complex signal, which might represent the case when Orthogonal Frequency-Division Multiplexing with a high number of sub-carriers is adopted [Wul+00]. Departing from the residual SI in (4.1), it can be rewritten as

$$y_{r_{si}}(t) = h\, x_{si}(t-\tau)e^{j(\omega_c(t-\tau))} - h_c\, x_{si}(t-\tau_c)e^{j(\omega_c(t-\tau_c))}. \tag{4.2}$$

In what follows it is considered that the channel gain is complex, $h = h_r + jh_j$, and the estimate of the channel's gain is given by $h_c = \epsilon h$, where $(1-\epsilon)$ is the channel's gain estimation error. Channel's phase estimation error is represented by $\Xi = \omega_c(\tau - \tau_c)$. It is also considered that the SI signal $x_{si}(t)$ is a random signal, whose value for a specific sample k is represented by a pair of two RVs $\{X_r, X_j\}$, i.e. for a specific sample k is represented $x_{si}(k\Delta_T) = X_r + jX_j$, where Δ_T represents the sample period. If the sample period is low, i.e. $\Delta_T << 2\pi/\omega_c$, and the value of the RVs $X_r + jX_j$ remain constant for several samples, we may assume that $\Pr[x_{si}(t-\tau) - x_{si}(t-\tau_c) = 0]$ is high, since the SI signal $x_{si}(k\Delta_T)$ may remain constant for a consecutive number of samples. While this approximation may be quite simplistic at this stage, the validation results presented in Section 4.4 show that it does not compromise the accuracy of the proposed modeling methodology. This is mainly because $X_r + jX_j$ take the same value for a consecutive number of samples, since the carrier frequency (and consequently the sampling frequency, Δ_T) is higher than any frequency component of the input signal x_{si}. After a few algebraic manipulations, the residual SI can be represented by its real and imaginary parts, $\mathfrak{Re}\{y_{r_{si}}\}$ and $\mathfrak{Im}\{y_{r_{si}}\}$, respectively, defined by

$$\mathfrak{Re}\{y_{r_{si}}\} = \alpha X_r + \beta X_j, \tag{4.3}$$

$$\mathfrak{Im}\{y_{r_{si}}\} = -\beta X_r + \alpha X_j. \tag{4.4}$$

(4.2) can be used in the system of 2 equations formed by (4.3) and (4.4), to obtain α and β, which are respectively given by

$$\alpha = h_r \cos(\omega_c(t-\tau)) - \epsilon h_r \cos(\omega_c(t-\tau_c)) - h_j \sin(\omega_c(t-\tau)) + \epsilon h_j \sin(\omega_c(t-\tau_c)), \tag{4.5}$$

and

$$\beta = -h_j \cos(\omega_c(t-\tau)) + \epsilon h_j \cos(\omega_c(t-\tau_c)) - h_r \sin(\omega_c(t-\tau)) + \epsilon h_r \sin(\omega_c(t-\tau_c)). \tag{4.6}$$

Using (4.3) and (4.4), the residual SI power after cancellation can be written as follows

$$P_{y_{r_{si}}} = \left(X_r^2 + X_j^2\right)\left(\alpha^2 + \beta^2\right), \tag{4.7}$$

which represents the amount of interference power received due to inability to cancel the SI.

4.3 Characterization of the Residual SI

This section describes the steps required to derive the distribution of the residual SI. Motivated by the fact that the channel may have different dynamics, two different cases are considered:

- *Low channel dynamics* - in this scenario the channel gain is almost time-invariant, and consequently h and h_c can be considered constants;

- *High channel dynamics* - in this scenario the channel gain is time-variant, and consequently h and h_c are assumed to be RVs.

4.3.1 High channel dynamics

By considering the case when the channel gain is time-varying and $x_{si}(t)$ is a circularly-symmetric complex signal, i.e., $X_r \sim \mathcal{N}(0, \sigma_x^2)$ and $X_j \sim \mathcal{N}(0, \sigma_x^2)$, Lemma 4.3.1 gives the distribution of the residual SI power when a SI Rician fading channel is considered, i.e., the time-varying variables h_r and h_j are realizations of the RVs $H_r \sim \mathcal{N}(\mu_h \cos(\vartheta), \sigma_h^2)$ and $H_j \sim \mathcal{N}(\mu_h \sin(\vartheta), \sigma_h^2)$, respectively. On other hand, Lemma 4.3.2 characterizes the distribution of the residual SI power when a SI Rayleigh fading channel is considered, where $H_r \sim \mathcal{N}(0, \sigma_h^2)$ and $H_j \sim \mathcal{N}(0, \sigma_h^2)$.

Lemma 4.3.1. *When the SI channel gain is distributed according to a Rice*[1] *distribution with non-centrality parameter μ_h and scale parameter σ_h, the probability density function of the SI power follows a product distribution given by*

$$f_{P_{y_{r_{si}}}}(z) = \frac{2^{(1/2-k_h/2)}\sigma_x^{(-k_h-1)}\lambda_A^{-k_h}}{\Gamma(k_h)}(\lambda_A/z)^{\frac{k_h-1}{2}} z^{k_h-1} K_{(k_h-1)}\left(\sqrt{\frac{2z}{\sigma_x^2\lambda_A}}\right) \tag{4.8}$$

where $K_{(k_h-1)}(.)$ is the modified Bessel function of the second kind ($(K_n(x))$ for $n = k_h - 1$), and λ_A, k_h and θ_h are given by

$$\lambda_A = \theta_h\left[1 + \epsilon^2 - 2\epsilon\cos\left(\omega_c(\tau - \tau_c)\right)\right], \tag{4.9}$$

$$k_h = \frac{(\mu_h^2 + 2\sigma_h^2)^2}{4\sigma_h^2(\mu_h^2 + \sigma_h^2)}, \tag{4.10}$$

$$\theta_h = \frac{4\sigma_h^2(\mu_h^2 + \sigma_h^2)}{\mu_h^2 + 2\sigma_h^2}. \tag{4.11}$$

Proof. Departing from (4.7), and assuming that $X_r \sim \mathcal{N}(0, \sigma_x^2)$ and $X_j \sim \mathcal{N}(0, \sigma_x^2)$, then X_r^2 and X_j^2 are distributed according to a chi-squared distribution with 1 degree of freedom, denoted by χ_1^2. X_r and X_j may be written as follows

$$X_r^2 \sim \sigma_x^2 {\chi_1}^2, \tag{4.12}$$

---

[1] The Rice distribution was assumed because the SI channel is formed between two antennas that are close to each other, in which there is a strong LOS component. Since the Rician fading model assumes that the received signal is the result of a dominant component (the LOS component), the SI channel is usually modeled by a Rician fading channel [Dua+12; Eve+14; Sho+17].

$$X_j^2 \sim \sigma_x^2 {\chi_1}^2. \tag{4.13}$$

By definition, if $Y \sim \chi_k^2$ and $c > 0$, then $cY \sim \text{Gamma}(k/2, 2c)$. Consequently,

$$X_r^2 \sim \text{Gamma}(1/2, 2\sigma_x^2), \tag{4.14}$$

and

$$X_j^2 \sim \text{Gamma}(1/2, 2\sigma_x^2). \tag{4.15}$$

Knowing that the sum of two gamma RVs with different shape parameters is given by $\text{Gamma}(k_1, \theta) + \text{Gamma}(k_2, \theta) \sim \text{Gamma}(k_1 + k_2, \theta)$, the following is obtained

$$X_r^2 + X_j^2 \sim \text{Gamma}(1, 2\sigma_x^2). \tag{4.16}$$

Departing again from (4.7), the term $\left(\alpha^2 + \beta^2\right)$ is a RV because h_r and h_j are time-varying variables representing realizations of the RVs H_r and H_j, respectively. After a few algebraic manipulations, and replacing h_r and h_j by the RVs H_r and H_h, respectively, $\alpha^2 + \beta^2$ is written as

$$\alpha^2 + \beta^2 = (H_j^2 + H_r^2)\left[1 + \epsilon^2 - 2\epsilon \cos\left(\omega_c(\tau - \tau_c)\right)\right]. \tag{4.17}$$

The Rician fading channel is described by parameters K and Ω, where K is the ratio between the power of LOS path and the power in the other reflected paths, and Ω is the total power from both paths. The signal envelope is Rician distributed with parameters $\mu_h = \sqrt{\frac{K\Omega}{1+K}}$ and $\sigma_h = \sqrt{\frac{\Omega}{2(1+K)}}$. K can also be expressed in decibels by the variable $K_{dB} = 10\log_{10}(K)$.

Defining ${H_p}' = (1/\sigma_h^2)(H_j^2 + H_r^2)$, ${H_p}'$ follows a non-central Chi-square distribution with two degrees of freedom, and non centrality parameter $\frac{{\mu_h}^2}{{\sigma_h}^2}$.

Applying the method of moments to provide a Gamma approximation for the distribution of ${H_p}'$, the following shape and scale parameters are given by,

$${k_h}' = \frac{(\mu_h^2 + 2\sigma_h^2)^2}{4\sigma_h^2(\mu_h^2 + \sigma_h^2)}, \tag{4.18}$$

$${\theta_h}' = \frac{4(\mu_h^2 + \sigma_h^2)}{\mu_h^2 + 2\sigma_h^2}. \tag{4.19}$$

Since ${H_p}'$ is considered instead of $H_j^2 + H_r^2$, the distribution that represents the residual SI channel power gain is approximatted by

$$H_j^2 + H_r^2 \sim \text{Gamma}(k_h, \theta_h), \tag{4.20}$$

following the same steps to obtain (4.16), where $k_h = {k_h}'$ and $\theta_h = \sigma_h^2 {\theta_h}'$.

Because $\left[1+\epsilon^2-2\epsilon\cos\Big(\omega_c(\tau-\tau_c)\Big)\right]$ is a constant, and knowing that when $Y \sim \text{Gamma}(k,\theta)$ and $c>0$, $cY \sim \text{Gamma}(k, c\theta)$, then

$$(H_j^2+H_r^2)\left[1+\epsilon^2-2\epsilon\cos\Big(\omega_c(\tau-\tau_c)\Big)\right] \sim \text{Gamma}\left(k_k, \theta_h\left[1+\epsilon^2-2\epsilon\cos\Big(\omega_c(\tau-\tau_c)\Big)\right]\right). \tag{4.21}$$

In (4.7) the term $(\alpha^2+\beta^2)$ only depends on the RVs H_r and H_j, and consequently is independent of the term $(X_r^2+X_j^2)$. Because (4.7) has the product of the two terms, the probability density function of $P_{y_{r_{si}}}$ is given by the classical product probability density function expressed as follows

$$f_{P_{y_{r_{si}}}}(z) = \int_{-\infty}^{\infty} f_{X_r^2+X_j^2}(x)\, f_{\alpha^2+\beta^2}(z/x)\frac{1}{|x|}\,dx. \tag{4.22}$$

Replacing $f_{X_r^2+X_j^2}(x)$ and $f_{\alpha^2+\beta^2}(z/x)$ in (4.22) by (4.16) and (4.21), respectively, the expression (4.23) is obtained. Solving the integral in (4.23), $f_{P_{y_{r_{si}}}}$ is finally given by

$$\begin{aligned} f_{P_{y_{r_{si}}}}(z) = \int_{-\infty}^{\infty} & \frac{\Big([1+\epsilon^2-2\epsilon\cos(\omega_c(\tau-\tau_c))]\theta_h\Big)^{-k_h}}{2\sigma_x^2\Gamma(k_h)|x|}\left(\frac{z}{x}\right)^{k_h-1} \times \\ \times \quad & e^{-\dfrac{x}{2\sigma_x^2}-\dfrac{z}{\theta_h x[1+\epsilon^2-2\epsilon\cos(\omega_c(\tau-\tau_c))]}}\,dx. \end{aligned} \tag{4.23}$$

$$f_{P_{y_{r_{si}}}}(z) = \frac{2^{(1/2-k_h/2)}\sigma_x^{(-k_h-1)}\lambda_A^{-k_h}}{\Gamma(k_h)}(\lambda_A/z)^{\frac{k_h-1}{2}}z^{k_h-1}K_{(k_h-1)}\left(\sqrt{\frac{2z}{\sigma_x^2\lambda_A}}\right). \tag{4.24}$$

The CDF of the residual SI power is given by

$$F_{P_{y_{r_{si}}}}(z) = 1-\left(\frac{2^{(1-k_h/2)}(\lambda_A z)^{k_h/2} \quad K_{k_h}\left(\sqrt{\frac{2z}{\sigma_x^2\lambda_A}}\right)}{(\sigma_x\lambda_A)^{k_h}\Gamma(k_h)}\right), \tag{4.25}$$

where $K_{k_h}(.)$ is the modified Bessel function of the second kind $((K_n(x))$ for $n=k_h)$.

□

Lemma 4.3.2. *When the SI channel gain is distributed according to a Rayleigh distribution with scale parameter σ_h, the probability density function of the SI power follows a product distribution given by*

$$f_{P_{y_{r_{si}}}}(z) = \frac{K_0\left(\sqrt{\frac{2z}{\sigma_x^2\lambda_B}}\right)}{\sigma_x^2\lambda_B}, \tag{4.26}$$

where $K_0(.)$ is the modified Bessel function of the second kind, and λ_B is given by

$$\lambda_B = 2\sigma_h^2\left[1+\epsilon^2-2\epsilon\cos\Big(\omega_c(\tau-\tau_c)\Big)\right]. \tag{4.27}$$

Proof. Assuming again that $X_r \sim \mathcal{N}(0,\sigma_x^2)$ and $X_j \sim \mathcal{N}(0,\sigma_x^2)$, the term $X_r^2 + X_j^2$ has the same distribution represented in (4.16).

In this case, when $H_r \sim \mathcal{N}(0,\sigma_h^2)$ and $H_j \sim \mathcal{N}(0,\sigma_h^2)$, the RV that represents $H_j^2 + H_r^2$ is given by

$$H_j^2 + H_r^2 \sim \text{Gamma}(1, 2\sigma_h^2), \tag{4.28}$$

following the same steps to obtain (4.16). As the term $\left[1+\epsilon^2-2\epsilon\cos\left(\omega_c(\tau-\tau_c)\right)\right]$ is a constant, then

$$(H_j^2 + H_r^2)\left[1+\epsilon^2-2\epsilon\cos\left(\omega_c(\tau-\tau_c)\right)\right] \sim \text{Gamma}\left(1, 2\sigma_h^2\left[1+\epsilon^2-2\epsilon\cos\left(\omega_c(\tau-\tau_c)\right)\right]\right). \tag{4.29}$$

Replacing $f_{X_r^2+X_j^2}(x)$ and $f_{\alpha^2+\beta^2}(z/x)$ in (4.22) by (4.16) and (4.29), respectively, the expression (4.30) is obtained. Solving the integral in (4.30), $f_{P_{y_{r_{si}}}}$ is finally given by

$$\begin{aligned} f_{P_{y_{r_{si}}}}(z) = \int_{-\infty}^{\infty} & \frac{1}{4\sigma_x^2\sigma_h^2\Gamma(1)^2[1+\epsilon^2-2\epsilon\cos(\omega_c(\tau-\tau_c))]|x|} \quad \times \\ \times \quad & e^{-\dfrac{x}{2\sigma_x^2}-\dfrac{z}{2\sigma_h^2 x[1+\epsilon^2-2\epsilon\cos(\omega_c(\tau-\tau_c))]}}\, dx. \end{aligned} \tag{4.30}$$

$$f_{P_{y_{r_{si}}}}(z) = \frac{K_0\left(\sqrt{\frac{2z}{\sigma_x^2\lambda_B}}\right)}{\sigma_x^2\lambda_B}, \tag{4.31}$$

where $K_0(.)$ is the modified Bessel function of the second kind $((K_n(x))$ for $n=0)$ and $\lambda_B = 2\sigma_h^2\left[1+\epsilon^2-2\epsilon\cos\left(\omega_c(\tau-\tau_c)\right)\right]$. The CDF of the residual SI power is given by

$$F_{P_{y_{r_{si}}}}(z) = 1 - \left(\frac{\sqrt{2\lambda_B z} \quad K_1\left(\sqrt{\frac{2z}{\sigma_x^2\lambda_B}}\right)}{\sigma_x\lambda_B}\right), \tag{4.32}$$

where $K_1(.)$ is the modified Bessel function of the second kind $((K_n(x))$ for $n=1)$. ☐

4.3.2 Low channel dynamics

By considering the case when the channel gain is constant and $x_{si}(t)$ is a circularly-symmetric complex signal, i.e., $X_r \sim \mathcal{N}(0,\sigma_x^2)$ and $X_j \sim \mathcal{N}(0,\sigma_x^2)$, Lemma 4.3.3 shows that the distribution of the residual SI power follows an exponential distribution with rate parameter λ_C.

Lemma 4.3.3. *When the channel gain is constant the SI power is exponentially distributed, i.e.*

$$f_{P_{y_{r_{si}}}}(z) = \frac{e^{\frac{-z}{\lambda_C}}}{\lambda_C}, \tag{4.33}$$

with rate parameter

$$\lambda_C = \frac{1}{2\sigma_x^2\left(h_r^2 + h_j^2\right)\left[1 + \epsilon^2 \ - 2\epsilon \cos\left(\omega_c(\tau - \tau_c)\right)\right]}. \tag{4.34}$$

Proof. Once again, $X_r \sim \mathcal{N}(0, \sigma_x^2)$ and $X_j \sim \mathcal{N}(0, \sigma_x^2)$ are assumed, then the term $X_r^2 + X_j^2$ has the same distribution represented in (4.16).

Contrarily to the case assumed in the Subsection 4.3.1, when h and h_c are considered constant, $h_r \in \mathbb{R}$ and $h_j \in \mathbb{R}$, then $\left(\alpha^2 + \beta^2\right) \in \mathbb{R}$, and $\left(\alpha^2 + \beta^2\right) > 0$. Departing from (4.7), using (4.16), and knowing that when $Y \sim \text{Gamma}(k, \theta)$ and $c > 0$, $cY \sim \text{Gamma}(k, c\theta)$, $P_{y_{r_{si}}}$ can be given by

$$P_{y_{r_{si}}} \sim \text{Gamma}\left(1, 2\sigma_x^2\left(\alpha^2 + \beta^2\right)\right). \tag{4.35}$$

Because $\text{Gamma}(1, \lambda^{-1}) \sim \text{Exp}(\lambda)$, $P_{y_{r_{si}}}$ can be rewritten as follows

$$P_{y_{r_{si}}} \sim \text{Exp}\left((2\sigma_x^2\left(\alpha^2 + \beta^2\right))^{-1}\right). \tag{4.36}$$

Using (4.5) and (4.6), (4.36) is finally rewritten as follows

$$P_{y_{r_{si}}} \sim \text{Exp}\left(\frac{1}{2\sigma_x^2\left(h_r^2 + h_j^2\right)\left[1 + \epsilon^2 \ - 2\epsilon \cos\left(\omega_c(\tau - \tau_c)\right)\right]}\right).$$

The CDF of the residual SI power is given by

$$F_{P_{y_{r_{si}}}}(z) = 1 - e^{\frac{-z}{\lambda_C}}. \tag{4.37}$$

☐

4.4 Validation and Results

This section evaluates the accuracy of the derivation proposed in Section 4.3. The evaluation methodology is presented in Subsection 4.4.1 and the accuracy of the derivation is discussed in Subsection 4.4.2.

4.4.1 Evaluation Methodology

The accuracy of the residual SI power distribution is evaluated through the comparison of Monte Carlo simulations with numerical results, obtained from the derivation presented in Section 4.3. The comparison includes different channel conditions and SI cancellation errors.

Regarding the simulations, the post-mixer canceller presented in Figure 4.1 was simulated. The simulation results were obtained using the Monte Carlo method during 200 μs of simulation time (72×10^6 samples were collected during each simulation). The up-conversion frequency was parametrized to $\omega_c = 2\pi \times 10^9$ rad/s, i.e., the IBFDX communication system is operating at a carrier frequency of 1 GHz (equivalent to a period $T_c = 1$ ns). In the simulations, a sample period $\Delta_T = T_c/360$ was adopted. The values of X_r and X_j were sampled from Normal distributions, $\mathcal{N}(0, \sigma_x^2)$, each $4T_c$ (with $\sigma_x^2 = \frac{1}{2}$). H_r and H_j were sampled from Normal distributions ($H_r \sim \mathcal{N}(\mu_h \cos(\vartheta), \sigma_h^2)$, $H_j \sim \mathcal{N}(\mu_h \sin(\vartheta), \sigma_h^2)$ for Rician fading, and $H_r \sim \mathcal{N}(0, \sigma_h^2)$, $H_j \sim \mathcal{N}(0, \sigma_h^2)$ for Rayleigh fading). For time-variant channels, H_r and H_j were sampled each $40T_c$, maintaining constant h_r and h_j during the simulation ($h_r^2 = h_j^2 = 1/2$ was assumed). An average unitary channel gain was considered in all fading channels, to guarantee a fair comparison. In the simulations, the residual SI was determined for each simulation sample collected each Δ_T, by computing (4.2). The residual SI power was also computed for each sample using (4.7). The parameters adopted in the simulations are presented in Table 4.1.

The numerical results were obtained computing (4.24) and (4.25) for time-variant Rician channels, (4.32) for time-variant Rayleigh channels, and (4.37) for time-invariant channels, respectively. From (4.24), (4.25), (4.32), and (4.37), we observe that the computation of the distribution of the residual SI power only depends on the statistics of the SI signal (X_r, X_j), the statistics of the SI channel (H_r, H_j), the channel's gain estimation accuracy (ϵ), and channel's phase estimation error (Ξ).

4.4.2 Accuracy Assessment

First, the distribution of the residual SI power was evaluated for different values of channel's gain estimation accuracy (ϵ) and considering perfect estimation of the channel's delay ($\tau = \tau_c$). Time-invariant and Rayleigh time-variant channels are compared. Numerical results are compared with simulation results in Figure 4.2. In the figure the "inv" curve represents the results obtained with the time-invariant channel. The "var - Rayleigh" curve represents the results obtained with the time-variant channel, when a Rayleigh fading SI channel is considered, with $\sigma_h^2 = \frac{1}{2}$. The CDF is plotted for different channel's gain estimation accuracy values (ϵ = [0.95, 0.90, 0.80]). The "Simulation" curves represent the results obtained through Monte Carlo simulatiom. The "Model" curves were obtained with the computation of (4.37) and (4.32) for time-invariant and time-variant Rayleigh channels, respectively.

Table 4.1: Parameters adopted in the simulations.

f_c	1 GHz	ω_c	$2\pi \times 10^9$ rad/s
σ_x^2	1/2	Ξ	$\{\pi/18, \pi/9, \pi/6\}$
T_c	1 ns	ϵ	$\{0.95, 0.90, 0.80\}$
Δ_T	1/360 ns	Simulation time	200 μs
ϑ	$\pi/4$	K_{dB}	$\{-10, 0, 3, 10\}$
Ω	1		

As can be seen, the numerical results computed with the proposed model are close to the results obtained through simulation. This is observed for the different levels channel's gain estimation accuracy and for the time-variant and invariant channels. As a general trend, it is observed that the SI power increases with the channel's gain estimation error $(1-\epsilon)$, as expected. Moreover, Figure 4.2 shows that the probability of observing higher values of residual SI power increases when the time-variant channels are considered, because of its higher dynamics.

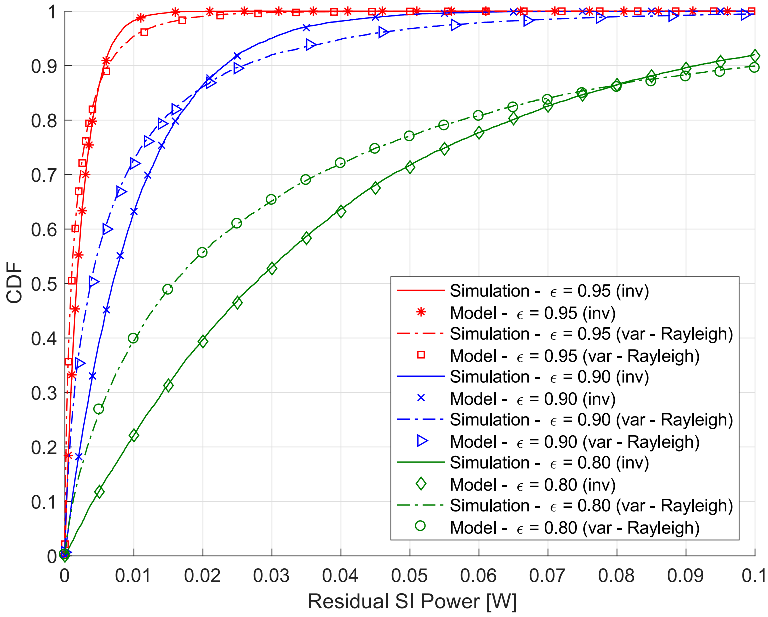

Figure 4.2: Residual SI Power for different values of ϵ (Rayleigh fading channel: $\sigma_h^2 = \frac{1}{2}$; Time-invariant channel: ${h_r}^2 = {h_j}^2 = 1/2$).

Next, the distribution of the residual SI power was evaluated for perfect estimation of the channel's gain $(\epsilon = 1)$ and considering imperfect estimation of the channel's delay. Figure 4.3 plots numerical and simulation results of the distribution of the residual SI power, adopting different phase estimation errors $(\Xi = \omega_c(\tau - \tau_c) = [\pi/18, \pi/9, \pi/6])$. The results were obtained for a time-invariant channel, a time-variant Rayleigh channel, and a time-variant Rician channel. In this case the numerical results in the "Model" curves were computed with (4.25) and (4.32), for Rician fading and Rayleigh fading, respectively. Once again, the numerical results are close to the results obtained through simulation. As can be seen, the phase estimation error significantly impacts on the distribution of the residual SI power and the average residual SI power increases with the phase estimation error. Moreover, the different types of the fading channel lead to different distributions of the residual SI power (for the same value of phase estimation error).

To evaluate the impact of parameter K_{dB} on the distribution of the residual SI power, we have considered different parameterizations of the Rician fading channel, i.e., $K_{dB} = [-10, 0, 10]$ dB, for a single value of phase estimation error $(\Xi = \pi/18)$ and considering perfect estimation of the channel's gain $(\epsilon = 1)$. Simulation and numerical results are presented in Figure 4.4, which confirm the accuracy of the proposed methodology for both PDF and CDF (numerically computed from (4.24) and (4.25), respectively). From the results in the Figure, it can be concluded that the

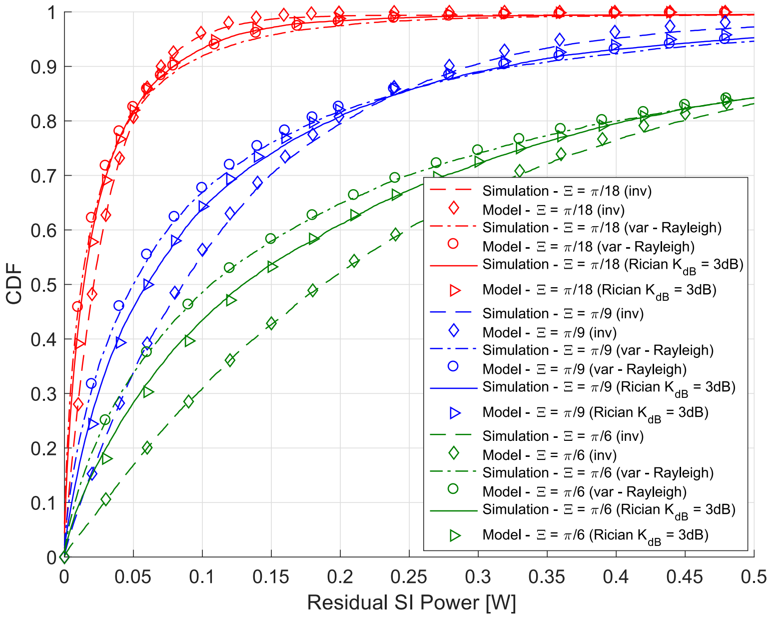

Figure 4.3: Residual SI Power for different values of Ξ (Rayleigh fading: $\sigma_h^2 = \frac{1}{2}$; Rician fading: $K_{dB} = 3$ dB, $\mu_h = 0.8162$, $\sigma_h = 0.4086$).

average residual SI power increases with the ratio between the power of the LOS path and the power of the other reflected paths.

In Section 4.2 it was assumed that the input signal $X_r + jX_j$ might take the same value for a consecutive number of samples, since the carrier frequency (and consequently the sampling frequency) is higher than any frequency component of the input signal x_{si}. To assess the impact of such assumption different simulations were performed considering that X_r and X_j are sampled from a Normal distribution at submultiples of the carrier frequency (f_c). Figure 4.5 compares the residual SI power obtained with the simulation results when X_r and X_j remain constant during one, two, three, and four carrier periods (curves “Simulation - 1 T$_c$”, “Simulation - 2 T$_c$”, “Simulation - 3 T$_c$”, and “Simulation - 4 T$_c$”, respectively). As can be seen, the accuracy of the proposed model increases as X_r and X_j remain with the same value for a longer period of time. The results show that the numerical results (represented by the curve “Model”) are close to the simulated results, when X_r and X_j remain constant for approximately 4 carrier periods, which is a valid assumption from the practical viewpoint. The results in Figure 4.5 confirm the accuracy of the proposed model, even when x_{si} exhibits high temporal dynamics.

Next the impact of the oscillator’s PN ($\phi(t)$) was analyzed on the residual SI power. A typical PN value for a low power low area oscillator was considered, built in a standard 130 nm complementary metal-oxide-semiconductor (CMOS) technology, operating at 1 GHz [Abd+12], which may typically exhibit a PN of approximately -100 dBc/Hz @ 1 MHz frequency offset. To determine the properties of the Gaussian distribution that represents the PN, the oscillator PN was simulated using the Matlab software package. The PN distribution obtained from the data simulated with the PN Simulink block was caracterized by a Gaussian distribution, $\mathcal{N}(\mu_{pn} = 0, \sigma_{pn}^2 = 16 \times 10^{-4})$. It was also assumed RC oscillators, by considering the minimum achievable PN threshold, which

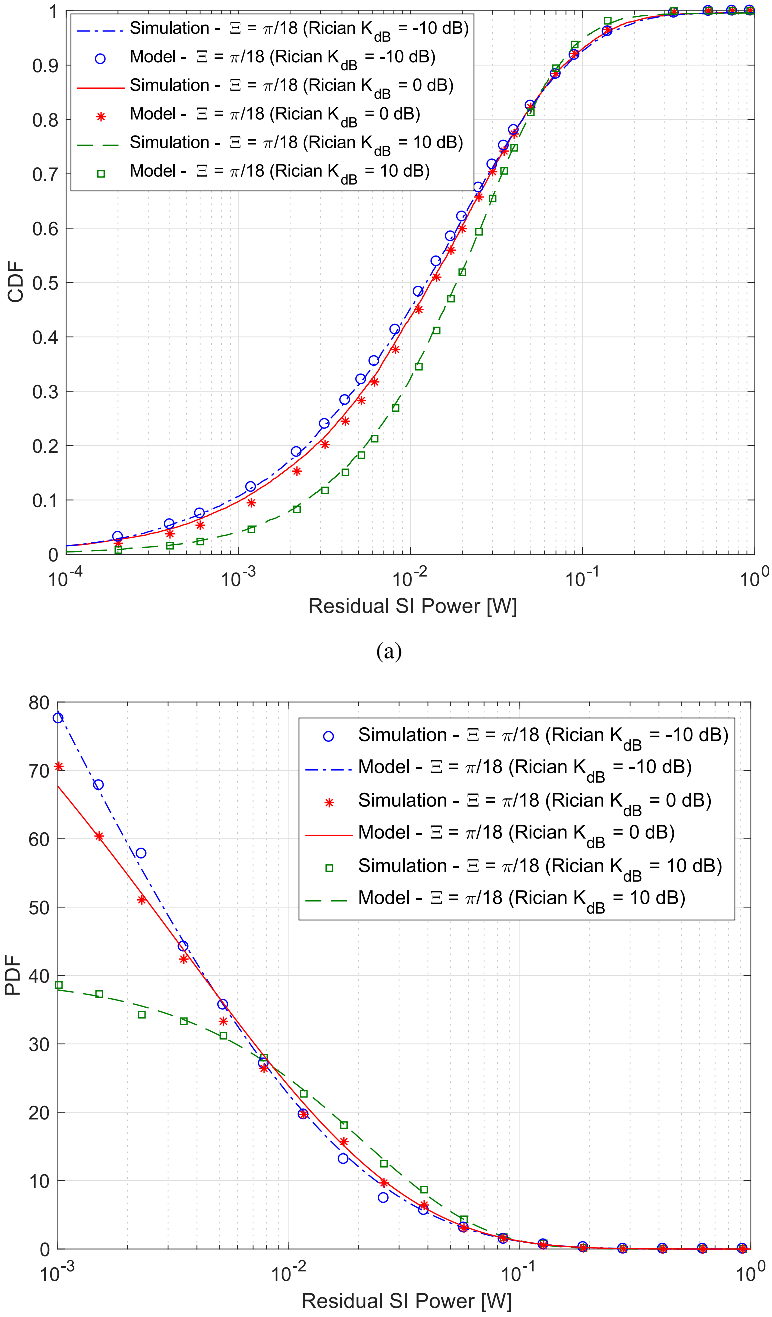

(a)

(b)

Figure 4.4: Residual SI Power for different values of K_{dB} (Rician fading: $\{K_{dB}$ = -10 dB; μ_h = 0.3015; σ_h = 0.6742$\}$, $\{K_{dB}$ = 0 dB; μ_h = 0.7071; σ_h = 0.5000$\}$, $\{K_{dB}$ = 10 dB; μ_h = 0.9535; σ_h = 0.2132$\}$).

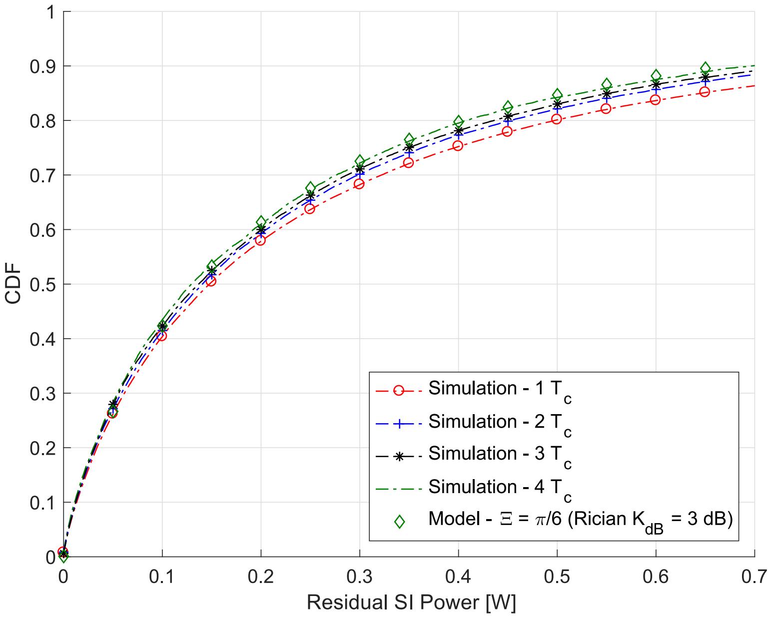

Figure 4.5: Residual SI Power for different sampling periods of $X_r + jX_j$ (Rician fading: $K_{dB} = 3$ dB, $\mu_h = 0.8162$, $\sigma_h = 0.4086$; $\Xi = \pi/6$).

is approximately -120 dBc/Hz [Nav+05]. For this case the oscillator PN is also represented by a Gaussian distribution, $\mathcal{N}(\mu_{pn} = 0, \sigma_{pn}^2 = 16 \times 10^{-6})$. The PN was simulated with a sample period $\Delta_T = T_c/360$ and $\phi(t)$ was added to the the upconverted signal. Thus, instead of using (4.2) to compute the residual SI, was considered the PN and the residual SI was computed with the

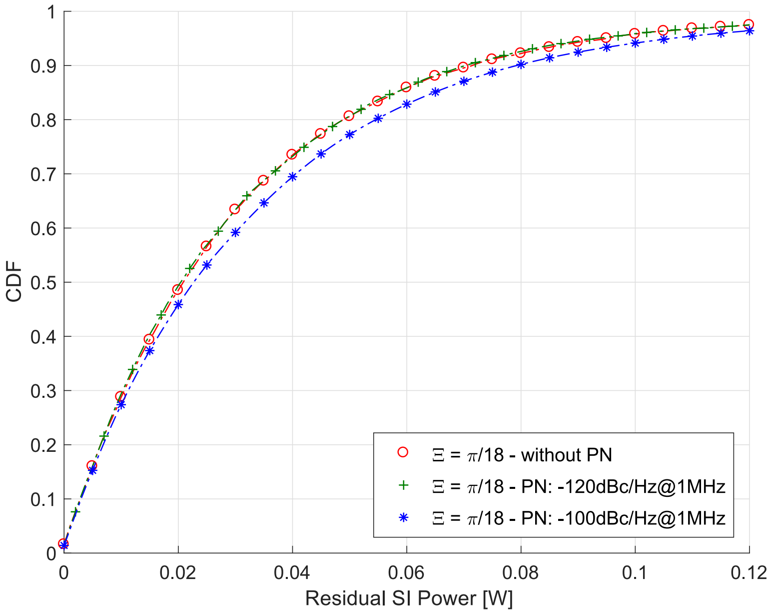

Figure 4.6: Residual SI Power for different values of PN (Time-invariant channel: ${h_r}^2 = {h_j}^2 = 1/2$; $\Xi = \pi/18$).

following formula

$$y_{r_{si}}(t) = h\, x_{si}(t-\tau)e^{j(\omega_c(t-\tau)+\phi(t-\tau))} - h_c\, x_{si}(t-\tau_c)e^{j(\omega_c(t-\tau_c)+\phi(t-\tau_c))}.$$

As can be seen in Figure 4.6, the quality of the oscillators impacts on the distribution of the residual SI power. At the minimum achievable PN threshold (-120 dBc/Hz @ 1 MHz), the impact of the PN on the distribution of the residual SI power is almost negligible. But, as the PN increases (-100 dBc/Hz @ 1 MHz) the average of the residual SI power also increases.

4.5 Conclusions

4.5.1 Applicability of the Proposed Approach

It is well known that the knowledge of the residual SI due to the analog-domain cancellation is crucial to design efficient SI estimation methods to be used in the digital-domain. By doing so, the efficiency of the joint AC and DC schemes may be improved. The analytical derivation of the distribution of the residual SI power presented in this chapter can be used to provide technical criteria for mitigating the SI residual interference in practical IBFDX communication systems. An obvious application is the compensation of the cancelation errors, which include the gain cancelation error $(1-\epsilon)$ and the phase cancellation error (Ξ). By using the theoretical derivation presented in Section 4.3 and multiple samples of the residual SI collected in a practical IBFDX system, different estimation techniques can be employed to estimate the cancelation errors and compensate them. However, the proposed derivation can also be useful for the academic community in general, to determine different aspects related with the performance analysis of IBFDX communications, including for example the capacity of IBFDX communication systems by using the residual SI power to derive the outage probability of a specific IBFDX system.

Finally, we highlight that although this chapter considers a single-tap delay channel, the approach may also be adopted in a multi-path scenario to provide an approximation of the residual SI. In IBFDX systems the LOS component is usually much higher than the non-LOS components (e.g.[Eve+14] reports 20-45 dBs higher). In this case, when the aggregated power of the non-LOS components is low, this model can capture a significant amount of the residual SI power.

4.5.2 Final Remarks

This chapter derives the distribution of the residual SI power due to channel estimation errors at the analog cancellation process. Closed form expressions were derived for the distribution of the residual SI power when Rician and Rayleigh fading SI channels are considered. Moreover, the distribution of the residual SI power was derived for low and high channel gain dynamics, by considering a time-invariant and a time-variant channel, respectively. The accuracy of the theoretical approach was assessed through Monte Carlo simulations for different levels of channel gain cancellation and phase errors during the channel estimation process. The results reported in the chapter show that the channel dynamics strongly influence the distribution of the residual SI power.

While for time-invariant channels the residual SI power is exponentially distributed, for time-variant channels the exponential distribution is not a valid assumption. Instead, the distribution of the residual SI power in time-variant channels can be approximated by a product distribution, as described in Lemma 4.3.1, which constitutes the main contribution of this chapter.

CHAPTER

5

INTERFERENCE IN COEXISTING NETWORKS

5.1 Introduction

With the continuous explosion of wireless communication systems, the number of wireless devices and networks continues to increase. Under this perspective, dynamic spectrum access arises as an efficient tool to increase the operation of the licensed spectrum bands, allowing the coexistence of different communication networks with different radio technologies in the same geographical area and spectrum space. At the same time, the increase of wireless devices, as a result of the rapid emergence of wireless and mobile services, have led to multiple coexisting networks scenarios.

The characterization of the interference in coexisting wireless networks is of high importance because the capacity of the wireless systems is limited by the competition of the users. However, coexistence increases the interference modeling complexity due to the intrinsic stochastic features of each coexisting network, including but not limited to different spatial distribution of the nodes, different transmission power, and different medium access patterns.

Motivated by the importance of the interference characterization in coexisting networks and its complexity, this chapter investigates the aggregate interference caused to a fixed node by multiple transmitters belonging to different coexisting networks. As a main contribution of this chapter, two different methods to characterize the distribution of the aggregate interference power are proposed. Instead of providing a numerical approximation of the aggregate interference distribution, the two methods proposed show that the aggregate interference can be accurately approximated by an α-μ distribution. Consequently, the aggregate interference can be approximated by a closed-form expression, without suffering the scalability issues related with the numerical solutions presented in the literature.

The first method approximates the aggregate interference by assuming that the interference caused by the transmitters located on a given annulus of the spatial region can be approximated by a Gamma distribution. The approximation is motivated by the work in [HG09], even though it does not consider fading or shadowing. The second method proposes a highly accurate approximation based on the α-μ distribution, which holds for the entire spatial region of each coexisting network.

The work developed in this chapter considers different spatial distributions of the coexisting networks, fast fading and shadowing propagation effects, and different transmission powers and medium access.

Chapter Contents

- **Section 5.2**: This section starts introducing the network scenario considered in the chapter, as well as the distribution of the nodes for static and mobile networks.
- **Section 5.3**: Describes the steps involved to model the aggregate interference caused to a central node by multiple nodes located in different networks, considering path loss, and slow and fast fading.
- **Section 5.4**: Proposes the first method to characterize the aggregate interference in coexisting networks, by assuming that the interference caused by the transmitters located on a given annulus of the spatial region can be approximated by a Gamma distribution.
- **Section 5.5**: Presents the second method to characterize the aggregate interference in coexisting networks, by assuming that the interference caused by the transmitters located on a given annulus of the spatial region can be approximated by a α-μ distribution.
- **Section 5.6**: This section assesses the accuracy of both methods, as well as the impact of network parameters, and the impact of mobility in coexisting Networks.
- **Section 5.7**: This section summarizes the chapter's conclusions.

5.2 System Description

In this chapter, we consider the scenario illustrated in Figure 5.1, where multiple Υ_η networks, with $\eta = 1,...,\upsilon$, coexist in the same RF band, and same spatial region with area $X_{max} \times Y_{max}$. The υ networks can be static or mobile. The nodes of the static networks are deployed according to a homogeneous PPP. The nodes of the mobile networks move according to the RWP mobility model [Bet+03], where each node is initially placed in a random position (x,y) sampled from the uniform distributions represented by $x \sim U(0,X_{max})$ and $y \sim U(0,Y_{max})$, and move to a random ending point with velocity uniformly sampled from $U(V_{min},V_{max})$. The nodes stop at the ending point for pause time T_p. After reaching the ending point a node repeats the same cycle. The average velocity of the nodes is denoted by $\mathrm{E}[V]$, which was studied in [Bet+03].

For modeling purposes, we adopt the SCM considered in Chapter 3, where the analysis of the aggregate interference received by the central node (node N_c in Figure 3.1) from the network Υ_η is derived by considering the nodes located in the L_η annuli centered on the receiver node. The radius of the larger and smaller circles of the annulus $l \in \{1,...,L_\eta\}$, are represented by $R_{\eta,l+1} = (R_{\eta,l} + l\rho)$ and $R_{\eta,l}$, respectively, where ρ denotes the annulus' width.

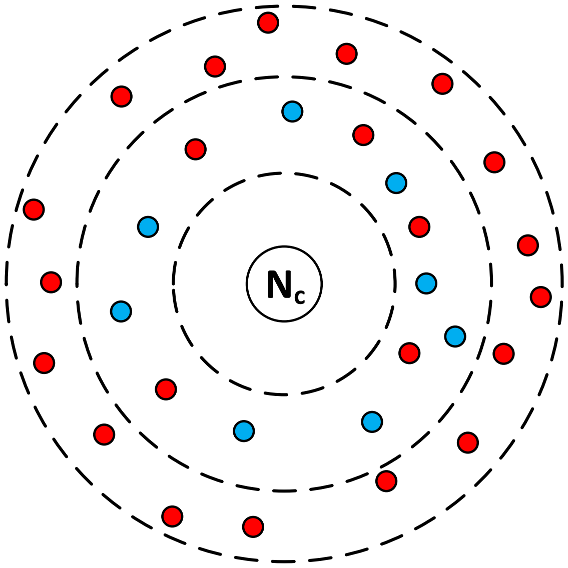

Figure 5.1: Nodes of multiple networks (different colors) distributed in a interference region.

The nodes of a given network Υ_η are thus located in a circular region with area $A_\eta = \sum_{l=1}^{L_\eta} A_{\eta,l}$, where $A_{\eta,l} = \pi\left((R_{\eta,l+1})^2 - (R_{\eta,l})^2\right)$ denotes the area of the annulus l.

Figure 5.2 represents the SCM to be applied for the coexistence of multiple networks.

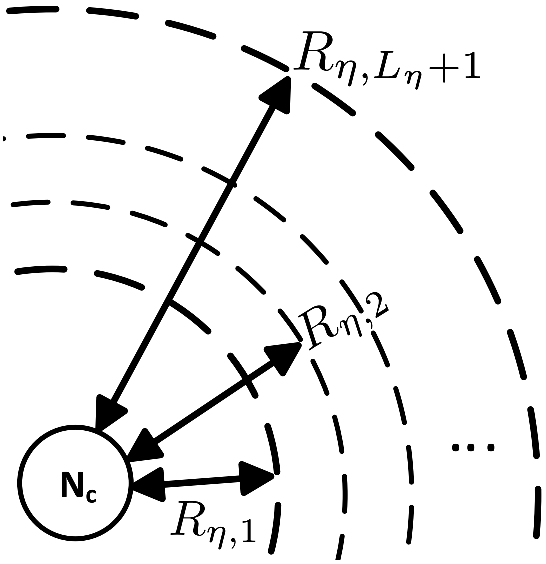

Figure 5.2: The node N_c receives from the n_η transmitters located in the area A_η.

The number of transmitters of the network Υ_η located in a particular annulus $l \in \{1,\ldots,L_\eta\}$ is represented by the RV $X_{\eta,l}$. For both static and mobile networks we consider that $X_{\eta,l}$ is distributed according to a truncated Poisson distribution given by

$$\mathrm{P}(X_{\eta,l} = k) = \frac{(\lambda_{\eta,l}A_{\eta,l}\tau_\eta)^k e^{-\lambda_{\eta,l}A_{\eta,l}\tau_\eta}}{k!\sum_{i=0}^{n_\eta}\frac{(\lambda_{\eta,l}A_{\eta,l}\tau_\eta)^i}{i!}e^{-\lambda_{\eta,l}A_{\eta,l}\tau_\eta}}, 0 \le k \le n_\eta, \tag{5.1}$$

where $\lambda_{\eta,l}$ is the node's spatial density, n_η is the total number of nodes of the network Υ_η, and τ_η is the individual transmission probability. We highlight that for static networks $\lambda_{\eta,l}$ is equal for all L_η annulus. However, for RWP mobile networks, the spatial distribution of the nodes is approximated by an IPP. Consequently, for mobile RWP networks, $\lambda_{\eta,l}$ takes a different value for each annulus l. In this chapter, we consider that the density parameter $\lambda_{\eta,l}$ adopted to model the mobile RWP networks is computed as proposed in (3.8), which takes into account the annuli's geometry (ρ; L_η; $R_{\eta,1}$), and mobility parameters ($V_{min}; V_{max}; X_{max}; Y_{max}; T_p$).

5.3 Interference from an annulus l of network Υ_η

The interference power caused by $n_{\eta,l}$ interferers belonging to the network Υ_η located in the annulus l is given by $I_{\eta,l} = \sum_{i=1}^{n_{\eta,l}} I_{\eta,l,i}$, where $I_{\eta,l,i}$ is the interference caused by the i-th interferer. The interference power $I_{\eta,l,i}$ is expressed by

$$I_{\eta,l,i} = P_{Tx_\eta} \psi_i (d_{\eta,l,i})^{-\wp}, \tag{5.2}$$

where P_{Tx_η} is the transmitted power, ψ_i is the instant value of the fading channel and shadowing gain, $d_{\eta,l,i}$ denotes the distance between the i-th interferer and the receiver, and $\wp$ is the path-loss coefficient. The values ψ_i and $d_{\eta,l,i}$ represent instant values of the RVs Ψ_i and $D_{\eta,l,i}$, respectively. The interferers are uniformly distributed, and consequently the PDF of $D_{\eta,l,i}$ is given by

$$f_{D_{\eta,l,i}}(x) = \begin{cases} \dfrac{2\pi x}{A_{\eta,l}} & R_{\eta,l} < x < R_{\eta,l+1} \\ 0, & \text{otherwise} \end{cases}. \tag{5.3}$$

To characterize the distribution of Ψ_i the small-scale fading (fast fading) and shadowing (slow fading) effects must be considered. The amplitude of the small-scale fading effect is described by a Rayleigh distribution with the following PDF

$$f_\zeta(x) = \frac{x}{\sigma_\zeta^2} e^{\frac{-x^2}{2\sigma_\zeta^2}},$$

where x is the envelope amplitude of the received signal, and $2\sigma_\zeta^2 = 1$ is the mean power of the multipath received signal. Regarding the shadowing effect, we have assumed that its power follows a Lognormal distribution with the following PDF

$$f_\xi(x) = \frac{1}{\sqrt{2\pi}\sigma_\xi x} e^{\frac{-(ln(x)-\mu_\xi)^2}{2\sigma_\xi^2}},$$

with $\sigma_\xi > 0$ and $\mu_\xi = -\frac{\sigma_\xi^2}{2}$. As described in [AK99], the PDF of a Lognormal distribution can be accurately approximated by the PDF of a Gamma distribution, yielding

$$f_\xi(x) \approx \frac{1}{\Gamma(\vartheta)} \left(\frac{\vartheta}{\omega_s}\right)^\vartheta x^{\vartheta-1} e^{-x\frac{\vartheta}{\omega_s}},$$

where ϑ is given by $\frac{1}{e^{\sigma_\xi^2}-1}$ and ω_s is equal to $e^{\mu_\xi}\sqrt{\frac{\vartheta+1}{\vartheta}}$.

Considering that the small-scale fading and shadowing are independent, the PDF of Ψ_i is represented by

$$f_{\Psi_i}(x) \approx f_{\zeta^2}(x)\cdot f_\xi(x) \approx \frac{2}{\Gamma(\vartheta)}\left(\frac{\vartheta}{\omega_s}\right)^{\frac{\vartheta+1}{2}} x^{\frac{\vartheta-1}{2}} K_{\vartheta-1}\left(\sqrt{\frac{4\vartheta x}{\omega_s}}\right),$$

which according to [AAY10] can be accurately approximated by the following Gamma distribution

$$f_{\Psi_i}(x) \approx \frac{x^{k_\psi-1}}{\Gamma(k_\psi)\theta_\psi^{k_\psi}} e^{-x/\theta_\psi}, \tag{5.4}$$

with scale and shape parameters given by $\theta_\psi = \left(\frac{2(\vartheta+1)}{\vartheta}-1\right)\omega_s$, and $k_\psi = \left(\frac{2(\vartheta+1)}{\vartheta}-1\right)^{-1}$, respectively.

Let $M_{I_{\eta,l,i}}(s)$ denote the MGF of the i-th interferer located within the annulus l, which is given by

$$M_{I_{\eta,l,i}}(s) \quad = \mathrm{E}_{I_{\eta,l,i}}[e^{sI_{\eta,l,i}}] = \mathrm{E}_{\Psi_i}\left[\mathrm{E}_{D_{\eta,l,i}}[e^{sI_{\eta,l,i}}]\right] = \int_0^{+\infty}\int_{R_{\eta,l}}^{R_{\eta,l+1}} e^{sI_{\eta,l,i}} f_{D_{\eta,l,i}}(x) f_{\Psi_i}(y)\,dx\,dy.$$

Using (5.2), (5.3), and (5.4), $M_{I_{\eta,l,i}}(s)$ can be simplified to

$$M_{I_{\eta,l,i}}(s) = \frac{2\pi}{A_{\eta,l}(2+k_\psi\wp)(P_{Tx_\eta}\theta_\psi s)^{k_\psi}} \times \left(\left(R_{\eta,l+1}\right)^{2+k_\psi\wp}\varrho(R_{\eta,l+1}) - \left(R_{\eta,l}\right)^{2+k_\psi\wp}\varrho(R_{\eta,l})\right),$$

with

$$\varrho(x) = {}_2\mathrm{F}_1\left(k_\psi, k_\psi+\frac{2}{\wp}, 1+k_\psi+\frac{2}{\wp}, -\frac{x^\wp}{P_{Tx_\eta}\theta_\psi s}\right).$$

When the individual interference $I_{\eta,l,i}$ is i.i.d in comparison with the interference from other interferers located within the same annulus, the MGF of the aggregate interference ($I_{\eta,l}$) caused by k active interferers is given by

$$M_{I_{\eta,l}|k}(s) \quad = M_{I_{\eta,l,1}}(s)\times M_{I_{\eta,l,2}}(s)\times\cdots\cdots\times M_{I_{\eta,l,k}}(s) = \left(M_{I_{\eta,l,i}}(s)\right)^k. \tag{5.5}$$

Using the law of total probability, the PDF of I_η is written as

$$f_{I_{\eta,l}}(j) = \sum_{k=0}^{\infty} f_{I_{\eta,l}}(j|X_{\eta,l}=k)\mathrm{P}(X_{\eta,l}=k),$$

leading to the MGF of the aggregate interference as follows

$$\mathrm{E}[e^{sI_{\eta,l}}] = \sum_{k=0}^{\infty}\mathrm{P}(X_{\eta,l}=k)M_{I_{\eta,l}/k}(s).$$

Using (5.1) and (5.5), the MGF of $I_{\eta,l}$ can be finally rewritten as

$$\mathrm{E}[e^{sI_{\eta,l}}] = e^{\lambda_\eta A_{\eta,l} \tau_\eta (M_{I_{\eta,l,i}}(s)-1)}. \tag{5.6}$$

5.4 Aggregate Interference - Method 1

According to the results in [HG09], the aggregate interference considering path-loss, fast fading and shadowing effects can be approximated by a Gamma distribution. In line of that, this method considers that the interference caused by the interferers of the network Υ_η located within the annulus l is distributed according to a Gamma distribution. Using (5.6), the expectation and the variance of the aggregate interference are written as

$$\mathrm{E}[I_{\eta,l}] = 2\pi\lambda_\eta \tau_\eta P_{Tx_\eta} e^{\mu_\xi} \sqrt{e^{\sigma_\xi^2}} \left(\frac{(R_{\eta,l+1})^{2-\wp} - (R_{\eta,l})^{2-\wp}}{2-\wp} \right),$$

and

$$\mathrm{Var}[I_{\eta,l}] = \pi\lambda_\eta \tau_\eta P_{Tx_\eta}^2 \theta_\psi^2 (k_\psi + k_\psi^2) \times \left(\frac{(R_{\eta,l+1})^{2-2\wp} - (R_{\eta,l})^{2-2\wp}}{1-\wp} \right),$$

respectively.

The aggregate interference is approximated by using the method of the moments, and the shape and the scale parameters of the Gamma distribution that characterizes the interference caused by the interferers of the annulus l, $I_{\eta,l}$, are represented by $k_{\eta,l}$ and $\theta_{\eta,l}$, being respectively given by

$$k_{\eta,l} = \mathrm{E}[I_{\eta,l}]^2/\mathrm{Var}[I_{\eta,l}], \tag{5.7}$$

$$\theta_{\eta,l} = \mathrm{Var}[I_{\eta,l}]/\mathrm{E}[I_{\eta,l}]. \tag{5.8}$$

Until now, we have only considered the aggregate interference due to interferers of a network Υ_η located within the annulus l. To obtain the aggregate interference of a given network Υ_η, the summation of the L_η annuli where all interferers are located must be considered. Let $\{Z_{\eta,l}\}_{l=1}^{L_\eta}$ be independent non-identically distributed (i.n.i.d.) Gamma RVs with parameters $k_{\eta,l}$ (shape) and $\theta_{\eta,l}$ (scale). The aggregate interference of the network Υ_η can be written as

$$I_\eta = \sum_{l=1}^{L_\eta} Z_{\eta,l}.$$

Assuming the coexistence of multiple networks with different features (e.g. transmission power and channel access probability), the joint aggregate interference can be written as

$$I_{agg} = \sum_{\eta=1}^{\upsilon} I_\eta,$$

where υ represents the number of different coexisting networks. The joint aggregate interference can be seen as the aggregate interference caused by the nodes located within the L_N annuli of υ coexisting networks, with $L_N = \upsilon L_\eta$.

Let $\{Z_j\}_{j=1}^{L_N}$ be i.n.i.d. Gamma RVs with parameters k_j and θ_j and $W_j \sim \text{Nakagami}(m_j, \Omega_j)$. The aggregate interference can be written as

$$I_{agg} = \sum_{j=1}^{L_N} Z_j = \sum_{j=1}^{L_N} {W_j}^2,$$

since by definition $Z_j = {W_j}^2$, with $k_j = m_j$ and $\theta_j = \Omega_j / m_j$. According to [Cos+08a], the sum of i.n.i.d. Nakagami-m RVs can be accurately approximated by an α-μ distribution[1]. Consequently, the PDF of I_{agg} can be expressed as [Cos+08a]

$$f_{I_{agg}}(y) \approx \frac{\alpha \mu^{\mu} y^{\alpha\mu - 1}}{\hat{r}^{\alpha\mu} \Gamma(\mu)} \exp\left(-\mu \frac{y^{\alpha}}{\hat{r}^{\alpha}}\right),$$

where $\hat{r} = \sqrt[\alpha]{\mathrm{E}[Y^{\alpha}]}$, and $\mu = \frac{\hat{r}^{2\alpha}}{\mathrm{Var}[Y^{\alpha}]}$. To compute $f_{I_{agg}}(y)$, the moment-based estimators for α and μ can be obtained from [Cos+08a] as

$$\frac{\Gamma^2(\mu + 1/\alpha)}{\Gamma(\mu)\Gamma(\mu + 2/\alpha) - \Gamma^2(\mu + 1/\alpha)} = \frac{\mathrm{E}^2[I_{agg}]}{\mathrm{E}[{I_{agg}}^2] - \mathrm{E}^2[I_{agg}]}, \tag{5.9}$$

and

$$\frac{\Gamma^2(\mu + 2/\alpha)}{\Gamma(\mu)\Gamma(\mu + 4/\alpha) - \Gamma^2(\mu + 2/\alpha)} = \frac{\mathrm{E}^2[{I_{agg}}^2]}{\mathrm{E}[{I_{agg}}^4] - \mathrm{E}^2[{I_{agg}}^2]}. \tag{5.10}$$

By its turn, the exact moments $\mathrm{E}[I_{agg}]$, $\mathrm{E}[{I_{agg}}^2]$, $\mathrm{E}[{I_{agg}}^4]$ required in (5.9) and (5.10), can be computed using the multinomial expansion as follows [Cos+08a]

$$\begin{aligned}\mathrm{E}[{I_{agg}}^n] = \sum_{n_1=0}^{n} \sum_{n_2=0}^{n_1} \cdots \sum_{n_{L_N-1}=0}^{n_{L_N-2}} \binom{n}{n_1} \binom{n_1}{n_2} \cdots \binom{n_{L_N-2}}{n_{L_N-1}} \\ \times \mathrm{E}[{W_1}^{2(n-n_1)}] \mathrm{E}[{W_2}^{2(n_1-n_2)}] \cdots \mathrm{E}[{W_{L_N}}^{2(n_{L_N-1})}],\end{aligned}$$

where the Nakagami-m moments are given as

$$\mathrm{E}[{W_j}^n] = \frac{\Gamma(k_j + n/2)}{\Gamma(k_j)} \left(\theta_j\right)^{n/2}.$$

Using the parameters α and μ, the parameter $\hat{r}$ can be estimated by

$$\hat{r} = \left[\frac{\mu^{2/\alpha} \Gamma(\mu) \mathrm{E}[I_{agg}]}{\Gamma(\mu + 2/\alpha)}\right]^{1/2}. \tag{5.11}$$

---

[1] The α-μ distribution is a general fading distribution written in terms of two physical parameters, where α is related to the non-linearity of the environment, and μ is associated to the number of multipath clusters [Cos+08b].

5.5 Aggregate Interference - Method 2

As observed in the previous section, the aggregate interference can be accurately approximated by an α-μ distribution. Knowing that the sum of i.n.i.d. α-μ RVs can be accurately approximated by an α-μ distribution [Cos+08b], now we approximate the interference caused to the receiver by the interferers located within the annulus l by an α-μ distribution. To obtain an approximation of the aggregate interference ($I_{\eta,l}$), the moments of our model need to be matched with the respective moments of the α-μ distribution. Consequently, (5.6) is used to derive the first, second and fourth moments of $I_{\eta,l}$, which are respectively given by

$$\begin{aligned}
\mathrm{E}[I_{\eta,l}] =& C_{\eta,l}\mathrm{m}_{1,l},\\
\mathrm{E}[{I_{\eta,l}}^2] =& {C_{\eta,l}}^2{\mathrm{m}_{1,l}}^2 + C_{\eta,l}\mathrm{m}_{2,l},\\
\mathrm{E}[{I_{\eta,l}}^4] =& {C_{\eta,l}}^4{\mathrm{m}_{1,l}}^4 + 6{C_{\eta,l}}^3{\mathrm{m}_{1,l}}^2\mathrm{m}_{2,l} + 3{C_{\eta,l}}^2{\mathrm{m}_{2,l}}^2\\
&+ 4{C_{\eta,l}}^2\mathrm{m}_{1,l}\mathrm{m}_{3,l} + {\mathrm{m}_{1,l}}^4,
\end{aligned}$$

where $C_\eta = \lambda_\eta A_{\eta,l}\tau_\eta$, and

$$\mathrm{m}_{n,l} = \frac{\pi(\theta_\psi)^n(P_{Tx\eta})^n\left((R_{\eta,l+1})^{(2-n\wp)} - (R_{\eta,l})^{(2-n\wp)}\right)}{A_{\eta,l}\left(1-(\frac{n\wp}{2})\right)}\prod_{j=0}^{n-1}(k_\psi + j).$$

The knowledge of $\mathrm{E}[I_{\eta,l}]$, $\mathrm{E}[{I_{\eta,l}}^2]$, and $\mathrm{E}[{I_{\eta,l}}^4]$, allows the computation of the moment-based estimators to determine the parameters $\alpha_{\eta,l}$, $\mu_{\eta,l}$ and $\hat{r}_{\eta,l}$ of the α-μ distribution that characterizes $I_{\eta,l}$, i.e.,

$$f_{I_{\eta,l}}(y) = \frac{\alpha_{\eta,l}\mu_{\eta,l}^{\mu_{\eta,l}}\, y^{\alpha_{\eta,l}\mu_{\eta,l}-1}}{\hat{r}^{\alpha_{\eta,l}\mu_{\eta,l}}\Gamma(\mu_{\eta,l})}\exp\left(-\mu_{\eta,l}\frac{y^{\alpha_{\eta,l}}}{\hat{r}_{\eta,l}^{\alpha_{\eta,l}}}\right).$$

These parameters can be computed by solving the system of equations formed by (5.9), (5.10) and (5.11) after replacing α, μ, $\hat{r}$, $\mathrm{E}[I_{agg}]$, $\mathrm{E}[{I_{agg}}^2]$ and $\mathrm{E}[{I_{agg}}^4]$ by $\alpha_{\eta,l}$, $\mu_{\eta,l}$, $\hat{r}_{\eta,l}$, $\mathrm{E}[I_{\eta,l}]$, $\mathrm{E}[{I_{\eta,l}}^2]$ and $\mathrm{E}[{I_{\eta,l}}^4]$, respectively.

Since we have already approximated $I_{\eta,l}$, i.e., the interference caused by the nodes within the l-th annulus of the η-th coexisting network, we are now interested on characterizing the interference caused by all annuli of all coexisting networks. The joint aggregate interference may be stated as being the aggregate interference caused by the nodes located within the L_N annuli of υ coexisting networks, with $L_N = \upsilon L_\eta$.

Let $\{Z_j\}_{j=1}^{L_N}$ be i.n.i.d. α-μ RVs with parameters $\alpha_{\eta,l}$, $\mu_{\eta,l}$ and $\hat{r}_{\eta,l}$, the aggregate interference can be written as

$$I_{agg} = \sum_{j=1}^{L_N} Z_j.$$

According to [Cos+08b], the sum of i.n.i.d. α-μ RVs can be accurately approximated by an α-μ distribution. Consequently, the parameters α and μ adopted to parametrize the α-μ distribution of the aggregate interference distribution, i.e. $f_{I_{agg}} \approx \alpha$-$\mu(\alpha, \mu, \hat{r})$, can be obtained again from (5.9) and (5.10), assuming that the exact moments $\mathrm{E}[I_{agg}]$, $\mathrm{E}[{I_{agg}}^2]$, $\mathrm{E}[{I_{agg}}^4]$ in (5.9) and (5.10) are now computed using the multinomial expansion as follows

$$\mathrm{E}[{I_{agg}}^n] = \sum_{n_1=0}^{n}\sum_{n_2=0}^{n_1}\cdots\sum_{n_{L_N-1}=0}^{n_{L_N-2}} \binom{n}{n_1}\binom{n_1}{n_2}\cdots\binom{n_{L_N-2}}{n_{L_N-1}}$$
$$\times \mathrm{E}[{Z_1}^{(n-n_1)}]\mathrm{E}[{Z_2}^{(n_1-n_2)}]\cdots\mathrm{E}[{Z_{L_N}}^{(n_{L_N-1})}],$$

where the n-th moment, $\mathrm{E}[{Z_j}^n]$, is given by

$$\mathrm{E}[{Z_j}^n] = \frac{\hat{r}_j\Gamma(\mu_j + n/\alpha_j)}{{\mu_j}^{(n/\alpha_j)}\Gamma(\mu_j)},$$

and the parameters μ_j, α_j and $\hat{r}_j$ represent the parameters $\mu_{\eta,l}$, $\alpha_{\eta,l}$ and $\hat{r}_{\eta,l}$ computed for each annulus of each individual coexisting network. Having determined α and μ, the parameter $\hat{r}$ can be estimated by (5.11) to finally parametrize $f_{I_{agg}}$, the PDF of the aggregate interference caused by the coexisting networks.

5.6 Model Validation and Discussions

This section presents numerical and simulation results of the aggregate interference power in coexisting networks, comparing the accuracy of the two methods in Subsection 5.6.1, evaluating the impact of different network parameters in Subsection 5.6.2, such as the density of nodes, the channel access probability, and the transmitted power level, and also analyzing the impact of nodes' mobility in Subsection 5.6.3.

5.6.1 Comparison of the two Methods

In this subsection, the assessment of the accuracy was carried out by comparing the numerical results obtained with Method 1 and Method 2 against Monte Carlo simulations. 3×10^6 samples of the aggregate interference power were adopted in the Monte Carlo methodology. To validate the distribution of the aggregate interference, we adopt the default values described in Table 5.1.

We consider two coexisting static networks, i.e., $\upsilon = 2$, with different densities of nodes (λ_1 and λ_2). Usually, the transmitters of the different networks also adopt different transmission powers and access the band with different medium access probabilities. We consider that static transmitters of network Υ_1 transmit twice the power of the transmitters of network Υ_2 (i.e., $P_{Tx_1} = 2000$ mW and $P_{Tx_2} = 1000$ mW). Regarding the medium access probabilities, the transmitters of network Υ_1 access the band when they have a new packet to transmit ($\tau_1 = 1.0$), while the transmitters of network Υ_2 transmit with probability $\tau_2 = 0.7$. In this way, the heterogeneity of the coexisting networks is taken into account by considering different nodes' densities, different transmitting powers, and different probabilities of accessing the band. The area where the interferers of the networks Υ_1 and Υ_2 are located was divided in $\{5, 2, 1\}$ annuli, meaning $L_N = \{10, 4, 2\}$, respectively.

Figure 5.3 compares the CDF of the aggregate interference power computed with the two methods described in Sections 5.4 and 5.5. Different number of annuli with different widths

Table 5.1: Parameters adopted in the simulations.

$R_{1,1}$	20 m	$R_{2,1}$	20 m
$R_{1,L_\eta+1}$	120 m	$R_{2,L_\eta+1}$	120 m
λ_1 (node/m^2)	1×10^{-4}	λ_2 (node/m^2)	2×10^{-4}
P_{Tx_1}	2000 mW	P_{Tx_2}	1000 mW
τ_1	1.0	τ_2	0.7
σ_ζ^2	0.5	σ_ξ	0.69
L_N	{10, 4, 2}	ρ	{20, 50, 100} m
$\wp$	2	Monte Carlo samples	3×10^6

($\rho = \{20, 50, 100\}$ m) were considered in the Method 1, $L_N = \{10, 4, 2\}$, to cover the networks' area A_η. For the Method 2, a single annulus was considered ($\rho = 100$ m) to represent the area of each coexisting network, i.e., $L_N = 2$. Table 5.2 presents the parameters of the α-μ distributions obtained to represent the CDF of I_{agg} with Method 1 and Method 2 (computed with (5.9), (5.10) and (5.11)).

Table 5.2: Parameters estimated for the model curves.

		α	μ	$\hat{r}$
Figure 5.3	Method 1 – $L_N = 10$	0.147	65.945	2.862
	Method 1 – $L_N = 4$	0.458	5.830	3.126
	Method 1 – $L_N = 2$	0.824	1.651	3.574
	Method 2 – $L_N = 2$	0.160	55.071	2.871

The “Method" curves in Figure 5.3 indicate the numerical results obtained with the proposed methods, while the “Simulation curve" represent the CDF obtained with Monte Carlo simulations. The results depicted in Figure 5.3 show that the accuracy of the Method 1 increases with L_N, i.e., by considering more annuli to cover the same area. This means that the Gamma distribution approximation used to characterize $I_{\eta,l}$ through the parameters in (5.7) and (5.8) is more accurate as more and thinner annuli are considered to cover the network's area. For $L_N = 10$, 5 annuli of width $\rho = 20$ m are considered for each network, and the numerical results obtained with Method 1 are close to the ones obtained through simulation. However, Method 2 obtains almost the same accuracy by only assuming a single annulus for each coexisting network. This fact highlights the advantage of the Method 2, because it achieves a similar accuracy by only computing the parametrization of $L_N = 2$ α-μ distributions, while the Method 1 needs to compute $L_N = 10$ parametrizations of Gamma distributions prior to the final α-μ approximation of the aggregate interference. Moreover, in Method 2 a single annulus can be adopted for each coexisting network, so that the accuracy of the method does not depend on the number and thickness of the annuli that represent the area of the network.

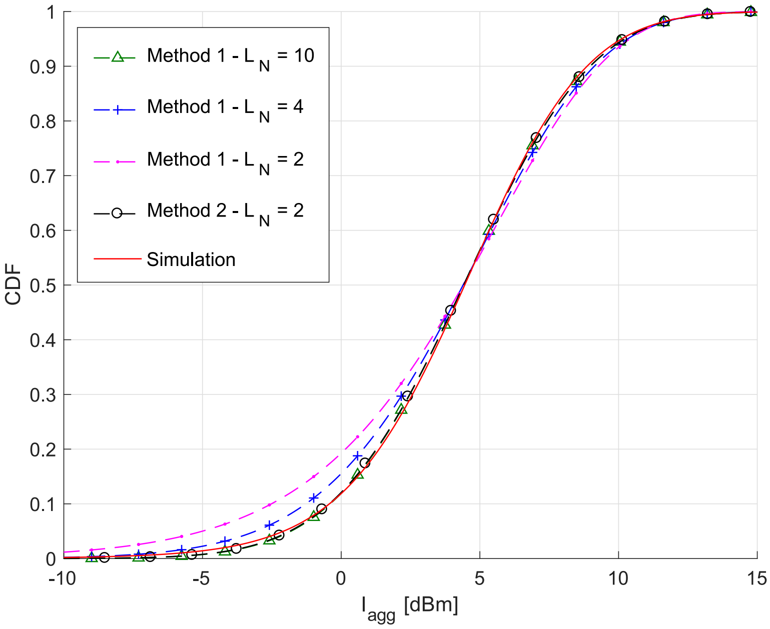

Figure 5.3: Comparison of the two methods proposed for modeling I_{agg}.

5.6.2 Impact of network parameters in Coexisting Networks

This subsection presents numerical and simulation results of the aggregate interference power, evaluating the impact of different network parameters, such as the density of nodes, the channel access probability, and the transmitted power level. Simulation and numerical results are presented for 2 coexisting static networks, i.e. $\upsilon = 2$. Different densities of nodes (λ_1 and λ_2) and different channel access probabilities (τ_1 and τ_2) are considered. To validate the distribution of the aggregate interference we adopt the default values described in Table 5.3 unless otherwise stated, and we compare the numerical results with results obtained through simulation.

Table 5.3: Parameters adopted in the simulations.

$R_{1,1}$	20 m	$R_{1,L+1}$	80 m
$R_{2,1}$	20 m	$R_{2,L+1}$	120 m
L_1	3	L_2	5
Simulation time	3000 s	$\wp$	2
λ_1 (node/m^2)	2×10^{-4}	λ_2 (node/m^2)	2×10^{-4}
τ_1	1	τ_2	1
ρ	20 m	σ_ξ	0.69
L_N	8	P_{Tx_η}	10^3 mW

The aggregate interference is sensed by the node N_c. The area where the interferers of the networks Υ_1 and Υ_2 are located was divided in 3 and 5 annuli of width 20 m (ρ), respectively, meaning $L_N = 8$. Table 5.4 depicts the parameters estimated for the analytical curves in Figures 5.4, 5.5 and 5.6.

Table 5.4: Parameters estimated for the model curves.

		α	μ	$\hat{r}$
Figure 5.4	$\tau_1 = 0.5$	0.298	17.464	2.520
	$\tau_1 = 0.7$	0.303	18.294	2.848
	$\tau_1 = 1$	0.307	19.824	3.345
Figure 5.5	$P_{Tx_1} = P_{Tx_2}$	0.399	8.112	2.313
	$P_{Tx_1} < P_{Tx_2}$	0.230	25.531	3.043
	$P_{Tx_1} > P_{Tx_2}$	0.377	8.100	3.592
Figure 5.6	Non-Overlapped	0.200	25.186	0.949
	Overlapped	0.298	17.464	2.520

The CDF of the aggregate interference is illustrated in Figure 5.4 considering different channel access probabilities for the nodes of the network Υ_1 ($\tau_1 = \{0.5; 0.7; 1\}$). The channel access probability was maintained constant for the network Υ_2 ($\tau_2 = 1$). From the results, we observe that the aggregate interference increases with the channel access probability, as expected. Moreover, the numerical results (represented in the figure by the legend “Model") are close to the results obtained through simulation (represented in the figure by the legend “Simulation").

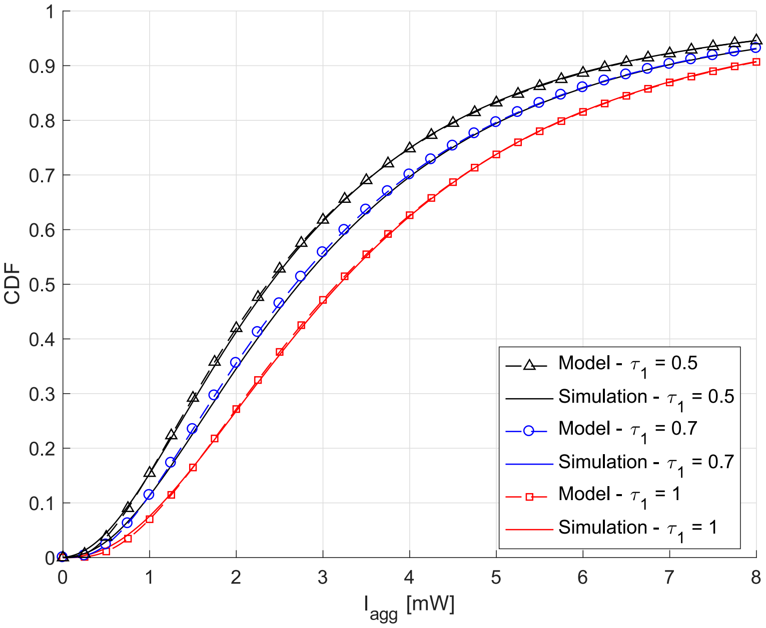

Figure 5.4: CDF of aggregate interference for different channel access probabilities of network Υ_1 (τ_1).

Figure 5.5 compares the results of aggregate interference for different transmitted power levels (P_{Tx_η}) of the two networks. The channel access probability was maintained constant for the two networks ($\lambda_1 = 2\times10^{-4}$ nodes/m^2 and $\lambda_2 = 1\times10^{-4}$ nodes/m^2). From the results we observe that the aggregate interference increases with the transmitted power level, and it can also be concluded that a higher density of nodes with higher transmission power located in the vicinity of N_c increases the aggregate interference.

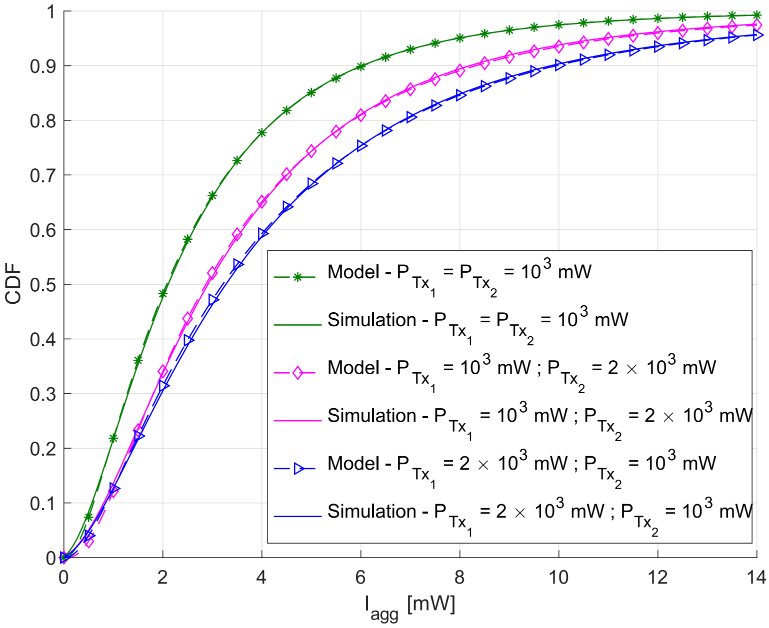

Figure 5.5: CDF of aggregate interference for different transmitted power levels (P_{Tx_η}).

In Figure 5.6 different node densities of network Υ_1 ($\lambda_1 = 1\times10^{-4}$ nodes/m^2) and Υ_2 ($\lambda_2 = 2\times10^{-4}$ nodes/m^2) were considered. This figure considers two different operational scenarios:

- in the “Overlapped Scenario" the unlicensed users of the two networks are allowed to operate between $R_{1,1} \equiv R_{2,1}$ and $R_{1,4} \equiv R_{2,4}$, i.e., the nodes of both networks coexist in the same spatial region;
- in the “Non-Overlapped Scenario" the two networks operate in disjoint spatial regions $(R_{1,L\eta+1} \equiv R_{2,1})$.

Consequently $L_N = 8$ was considered for the “Overlapped Scenario" and $L_N = 5$ was considered in the “Non-Overlapped Scenario". Once again, the proposed methodology approximates the distribution of aggregate interference caused to the node N_c. Regarding the parameter L_N, both model's accuracy and model's complexity increase with L_N.

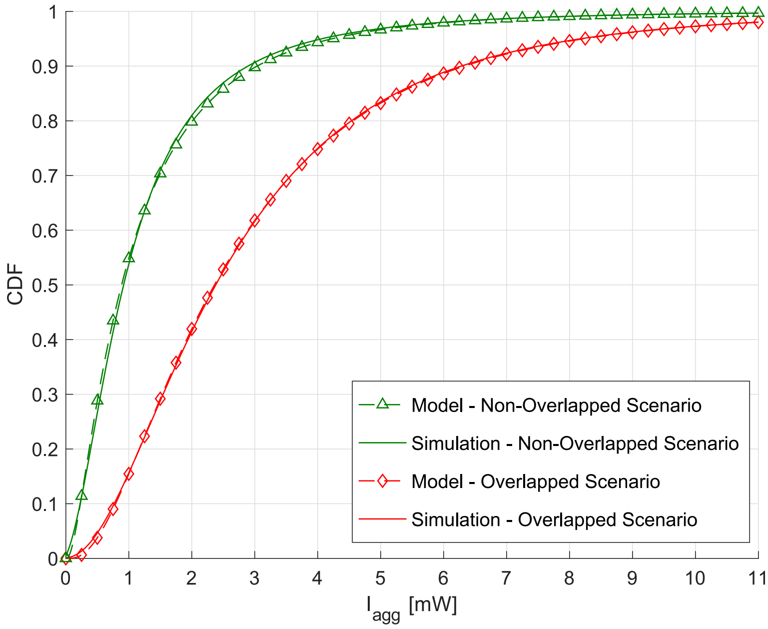

Figure 5.6: CDF of aggregate interference for overlapped and non-overlapped scenarios.

5.6.3 Impact of mobility in Coexisting Networks

This subsection presents numerical and simulation results of the aggregate interference power, evaluating the impact of different network mobility. We consider two coexisting networks ($\upsilon = 2$): a static network (Υ_1), and a network (Υ_2) where the nodes move according to the RWP. Three different mobility scenarios are analysed for Υ_2, considering the case where nodes are static ($\mathrm{E}[V] = 0$ m/s), or mobile with different average velocities ($\mathrm{E}[V] = \{10.82, 1.50\}$ m/s).

The parameters adopted in the validation are presented in Table 5.5, which are divided in the parameters related with the “Propagation Effects", the parameters of the network Υ_1 (“Static Network"), and the parameters of the network Υ_2 (“Mobile Network").

The assessment of the model is carried out by comparing Monte Carlo simulation results with numerical results of the aggregate power (I_{agg} approximated by (5.9)).

In the SCM, we have considered the same circular area for both networks Υ_1 and Υ_2, i.e., $R_{1,1} = R_{2,1} = 20$ m, $R_{1,L_\eta+1} = R_{2,L_\eta+1} = 120$ m, and $\rho_1 = \rho_2 = 20$ m.

In Figure 5.7, we compare the CDF of the aggregate power (I_{agg}) generated by the coexisting networks (Υ_1 and Υ_2) for the different mobility scenarios considered in network Υ_2 ($\mathrm{E}[V] = \{10.82$ m/s$, 1.50$ m/s$, 0$ m/s$\}$).

Table 5.6 presents the α-μ distribution parameters adopted in (5.9) to approximate I_{agg} for the different average velocities $\mathrm{E}[V]$. As can be seen, the numerical results (represented by the “Model" curves) are close to the results obtained through simulation. This indicates that the α-μ distribution in (5.9) can effectively approximate the distribution of I_{agg} with high accuracy. Moreover, we observe that the aggregate power increases with the mobility of the network Υ_2, which is due to the higher density of nodes closer located to N_{Tx} as the node's mobility increase [Bet+03].

Table 5.5: Parameters adopted in the simulations.

Propagation Effects	P_{Tx_η}	10^3 mW	$\wp$	2
	σ_ξ	0.69	${\sigma_h}^2$	1/2
	$\sigma^2_{n_d}$	0.01 mW		

Static Network (Υ_1)	$R_{1,1}$	20 m	$R_{1,L_\eta+1}$	120 m
	ρ_1	20 m	L_1	5
	λ_1 (node/m^2)	1×10^{-4}		

Mobile Network (Υ_2)	$R_{2,1}$	20 m	$R_{2,L_\eta+1}$	120 m
	ρ_2	20 m	L_2	5
	V_{min}	5 m/s	V_{max}	20 m/s
	n_2	100	τ_2	1
	E[V]	$\{10.82, 1.50, 0\}$ m/s	X_{max}	1000 m
	T_p	$\{0, 300, 3000\}$ s	Y_{max}	1000 m

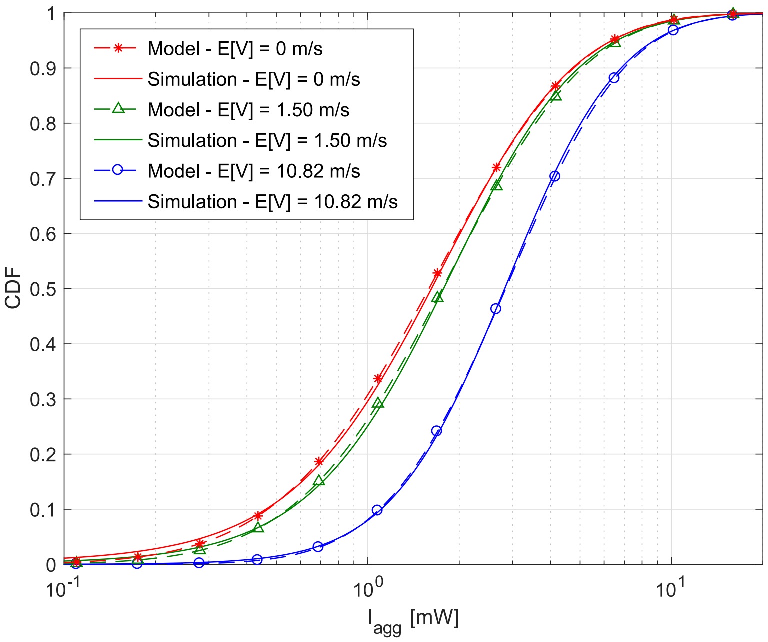

Figure 5.7: CDF of the aggregate power when Υ_1 and Υ_2 coexist, and considering different average speeds of Υ_2's nodes.

Table 5.6: Parameters estimated for the model curves of I_{agg}.

		α	μ	$\hat{r}$
Figure 5.7	$\mathrm{E}[V] = 10.82$ m/s	0.198	49.032	2.946
	$\mathrm{E}[V] = 1.50$ m/s	0.263	19.548	1.881
	$\mathrm{E}[V] = 0$ m/s	0.275	16.621	1.714

5.7 Conclusions

This chapter characterized the problem of the coexistence interference caused by multiple networks to a central node, when the nodes of the static networks are deployed according to a homogeneous PPP, and the nodes of the mobile networks are distributed according to the RWP mobility model.

The contribution of this chapter is mainly focused on the derivation of two methods that approximate the distribution of the aggregate coexisting interference by an α-μ distribution. The proposed methods advance the current state of the art by proposing a closed-form expression for the approximation of the aggregate interference (instead of a numerical solution).

Several simulation results compared the two proposed methods, and also evaluated the impact of different network parameters, such as the density of nodes, the channel access probability, and the transmitted power level. Finally, the impact of different network mobility was also evaluated, analysing three different mobility scenarios.

CHAPTER

6

MODEL APPLICATION SCENARIOS

This chapter presents several applications where the theoretical results of the previous chapters can be used to aid the analysis of different aspects of multiple access networks. Section 6.1 characterizes the transmission capability of a CRN, when the PUs are mobile. The transmission capability identifies the available opportunities for secondary user's SU's transmission. No opportunities are available when mobile PUs are active/transmitting within the SU's sensing region. However, admitting multiple PUs outside the SUs' sensing region, the interference caused to a SU can lead to a misinterpretation of a non-interfering PU due to the high power received from the multiple PUs. Thus, based on the amount of aggregate interference characterized in Chapter 3, Section 6.1 defines a new SC metric to include the Spatial False Alarm (SFA) effect caused by the mobile PUs located outside the SU sensing region.

In Section 6.2, we investigate the impact of wireless-powered communications when energy is harvested from multiple static and/or mobile wireless coexisting networks. In a first step, we use the aggregate power characterized in Chapter 5 to derive the energy received by a harvester node when it harnesses the energy generated by the coexisting wireless networks. Considering that the harvester node acts as a transmitter after the harvesting duration, we derive the outage probability for such coexisting scenario. In addition, the throughput achieved by the harvester node is also characterized, and the optimal harvesting duration is identified taking into account the mobility of the coexisting networks, the features of the static networks, the energy harvesting process, as well as the communication performance between the harvester node and the receiver. Our work shows that the distribution of the power received by the harvester from the coexisting networks can be accurately approximated by an $\alpha - \mu$ distribution. Moreover, the mobility also impacts on the optimal throughput of the wireless-powered communications, which is accurately confirmed by the proposed analysis and extensive simulations.

Section 6.3 derives a method to compute the optimal carrier-sensing range in a CSMA network. To investigate the optimal carrier-sensing range it is defined an utility function that takes into account the medium access probability of the node, and at the same time the carrier-sensing range. To derive the medium access probability it is used the aggregate power characterized in Chapter 5. The optimal carrier-sensing range is identified for two different scenarios, considering the cases when the coexisting networks are spatially overlapped or non-overlapped.

Finally, in Section 6.4 we derived a method to estimate the residual SI power in a IBFDX system. Considering the case when the channel gain is time-varying, admitting a Rician fading SI channel, and adopting the Lemma 4.3.1, we derive a estimation method for the distribution of the residual SI with a set of samples. We also evaluate the impact of the length of the sample set in the estimation method. The results show that a larger set of samples allows more accurate results and also the quality of the estimation even when a small set of samples is adopted.

6.1 Sensing Capacity of Cognitive Radio Mobile Networks

In CRNs, the non-licensed users usually denominated Secondary Users (SUs) must detect the activity of the licensed users, denominated Primary Users (PUs), in order to utilize the unused spectrum bands without causing them harmful interference. Spectrum Sensing (SS) plays a central role in CRNs, since it is possible detect the availability of vacant portions (holes) of spectrum in the spatial sensing area of a SU.

In CRNs, the mobility of the PUs introduces an additional challenge to detect its activity. Consequently, the SUs' transmission capability in the presence of the PUs, hereafter denoted as SC, is more difficult to be characterized in mobile scenarios.

The SC metric was introduced in [LA08] for static CRNs, where the nodes do not move, being defined as

$$C^{static} = \varepsilon \cdot \zeta \cdot W \cdot P_{off}, \tag{6.1}$$

where ε represents the sensing efficiency, ζ is the spectral efficiency of the band (bit/sec/Hz), W is the bandwidth and P_{off} represents the probability of the band being available to SUs due to the inactivity of PUs. Recently, the SC was extended to the case when multiple PUs may move [Cac+11; Cac+13], being defined as

$$C^{mob} = \varepsilon \cdot \zeta \cdot W \cdot P_{I_{off}}, \tag{6.2}$$

where $P_{I_{off}}$ represents the probability of not occurring any activity caused by the PUs that may be located within the SU's sensing region. However, although defining the SC for mobile scenarios and admitting multiple PUs, [Cac+11; Cac+13] do not consider the case when the PUs located outside the sensing region of a SU may be anomaly detected. This effect of a SU misinterpreting a non-interfering PU was firstly studied in [Han+11] for a single PU, who have named it as the SFA effect. SFA was recently studied in [Han+13] considering multiple static PUs. When the SFA is considered, the SC defined in (6.2) is an upper bound because SFA may cause SUs to not transmit when no PU is active within their sensing region. Differently from [Cac+11; Cac+13], we consider the occurrence of the SFA effect in a CRN with multiple mobile PUs, being the SC now defined as

$$C^{mob}_{SFA} = \varepsilon \cdot \zeta \cdot W \cdot \left(P_{O_{SFA}} P_{I_{off}}\right), \tag{6.3}$$

where $P_{O_{SFA}}$ represents the probability of not occurring a spatial false alarm by the nodes located outside the SU's sensing region.

The characterization of the sensing capacity when both mobility [Cac+11; Cac+13] and SFA effects [Han+11; Han+13] are considered has not been addressed before. The main contributions of this section are as follows:

- The probability of SFA is derived through the characterization of the amount of aggregate interference caused by the mobile PUs located outside the SU sensing region, using the results presented in Chapter 3;
- The SC of CRNs, defined in [Cac+11; Cac+13], is extended to include the SFA effect. Both simulation and theoretical results show that SFA should not be neglected.
- We confirm that the SFA effect decreases the SC, and the results in [Cac+11; Cac+13; LA08] represent a SC's upper bound;
- Regarding the mobility of the nodes, it is shown that the SC varies inversely with the average speed of the PUs.

6.1.1 Network scenario

It is considered a CRN where n PUs move in a region defined by the area $X_{max} \times Y_{max}$ according to the RWP mobility model, similar to the RWP model that was defined in Chapter 3.

The system considered in this section is depicted in Figure 6.1. A fixed central SU N_c is located in the center of the considered scenario (in the position $(X_{max}/2, Y_{max}/2)$), which senses the activity of the mobile PUs located in the circular sensing region with radius R_i^1 (represented by the dark disk surrounding N_c).

This section considers the SU's sensing region concept instead of the PU's protection region. However, both concepts are equivalent if the PU's protection range is equal or smaller than the SU's sensing range.

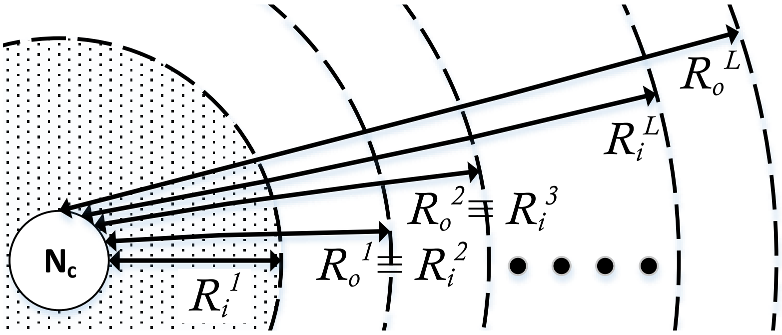

Figure 6.1: Spatial scenario considered. The SU's sensing region is represented by the area $A_{SR} = \pi(R_i^1)^2$. The PUs located outside the sensing region are found in the annulus area $A = \pi\left((R_o^L)^2 - (R_i^1)^2\right)$.

6.1.2 Sensing Capacity Definition

A SU senses the band licensed to PUs distinguish between occupied and vacant spectrum. The sensing decision considered takes into account the amount of aggregate interference sensed outside the sensing region.

Departing from the definition of SC in (6.3), we first define $P_{I_{off}}$, the probability of not occurring any activity caused by the PUs that may be located within the SU's sensing region. According to (3.7), the probability of a PU being located within the sensing region of the SU N_c is given by

$$P_I = \int_{(x_{N_c}-R_i^1)}^{(x_{N_c}+R_i^1)} \int_{\left(y_{N_c}-\sqrt{(R_i^1)^2-(x-x_{N_c})^2}\right)}^{\left(y_{N_c}+\sqrt{(R_i^1)^2-(x-x_{N_c})^2}\right)} f_{XY}(x,y)dydx. \tag{6.4}$$

Since the PUs move independently of each other, the probability of finding $k \leq n$ PUs within the SU's sensing region is given by the binomial distribution probability mass function, i.e.,

$$B(n,k,P_I) = \binom{n}{k}(P_I)^k(1-P_I)^{(n-k)}. \tag{6.5}$$

Finally, $P_{I_{off}}$ is defined as

$$P_{I_{off}} = \sum_{k=0}^{n} B(n,k,P_I) \cdot (1-\tau)^k, \tag{6.6}$$

since the k PUs within the SU's sensing region are inactive with probability $(1-\tau)^k$.

Regarding $P_{O_{SFA}}$ in (6.3), which represents the probability of not occurring a spatial false alarm due to the PUs located outside the SU's sensing region, and following the notation in (6.6) we start to consider that $n-k$ PUs are located outside the SU's sensing region. A spatial false alarm does not occur if the aggregate interference power caused by the PUs located outside the sensing region is lower than a given threshold (γ). Its probability is represented by $P(I_{agg}\{n_l = n-k\} \leq \gamma)$, where $\{n_l = n-k\}$ indicates that the parameters k_l and θ_l must be computed assuming n_l defined in Subsection 3.3.1 equal to $n-k$. After computing the parameters k_l and θ_l, $f_{I_{agg}}(s)$ may be also computed through (3.34) and

$$P(I_{agg}\{n_l = n-k\} \leq \gamma) = \int_0^{\gamma} f_{I_{agg}}(s)ds. \tag{6.7}$$

By considering the different number of $n-k$ PUs that may be localized outside the session region, $P_{O_{SFA}}$ is given by

$$P_{O_{SFA}} = \sum_{k=0}^{n} P(I_{agg}\{n_l = n-k\} \leq \gamma), \tag{6.8}$$

and finally using (6.3), (6.6) and (6.8), the sensing capacity is written as follows

$$C_{SFA}^{mob} = \varepsilon \cdot \zeta \cdot W \sum_{k=0}^{n} B(n,k,P_I) \cdot (1-\tau)^k \cdot P(I_{agg}\{n_l = n-k\} \leq \gamma). \tag{6.9}$$

6.1.3 Comparison Results

In this subsection we compare the impact of the SFA in the SU's SC. The SC is computed with (6.9) and compared with the results obtained in [Cac+11] (similar to (6.2)), which neglects the SFA effect.

Different network scenarios were defined varying the number of mobile PUs from a single PU to 19. The PUs moving according to the RWP mobility model achieve different average velocities, $E[V] = \{1.50, 10.82\}$ m/s, by adopting $T_P = \{0, 300\}$s, respectively. Different probabilities of PU's activity were also considered, i.e. $\tau = \{0.33, 0.66\}$. The simulations were run for each number of PUs and adopting constant T_P and τ values. The missing parameters related with the propagation model and the computation of theoretical model are described in Table 6.1.

Table 6.1: Parameters adopted to compute the comparison results.

X_{max}	1000 m	R_i^1	100 m	$\wp$	2
Y_{max}	1000 m	T_P	0 s, E[V]=10.82 m/s	ρ	10 m
V_{min}	5 m/s	T_P	300 s, E[V]=1.50 m/s	L	61
V_{max}	20 m/s	$\varepsilon \cdot \zeta \cdot W$	1	γ	0.1 mW

The sensing capacity results (computed with (6.9) and (27) in [Cac+11]) are illustrated in Figure 6.2. Figure 6.2(a) plots the results for $E[V] = 10.82$ m/s, while 6.2(b) plots the result for $E[V] = 1.50$ m/s.

Regarding the impact of the PUs' mobility on the SC, it is well known that the spatial density of the nodes moving according the RWP model increases within the sensing region of the node N_C as the average velocity of the nodes increase [Bet+03]. Consequently, more PUs are likely to be located within the sensing region as the average velocity of the PUs increases. In this case, the node N_c detects higher PUs' activity within its sensing region, leading to a lower SC (Figure 6.2(a)), when compared to a scenario of lower average velocity (Figure 6.2(b)).

Finally, the results in Figure 6.2 show that for both assumptions (considering/neglecting the SFA) the SC varies inversely with the number of PUs, the level of PU's activity (τ), and the average velocity of the PUs ($E[V]$). However, when the SFA effect is considered, the SC decreases more sharply, and the deviation from neglecting the SFA increases as both the number of PUs and PU's level of activity increase, or when the average velocity of the nodes decrease. Moreover, the deviation observed in the SC confirms that when the SFA effect is neglected the results obtained with [Cac+11] represent an upper bound of the SC.

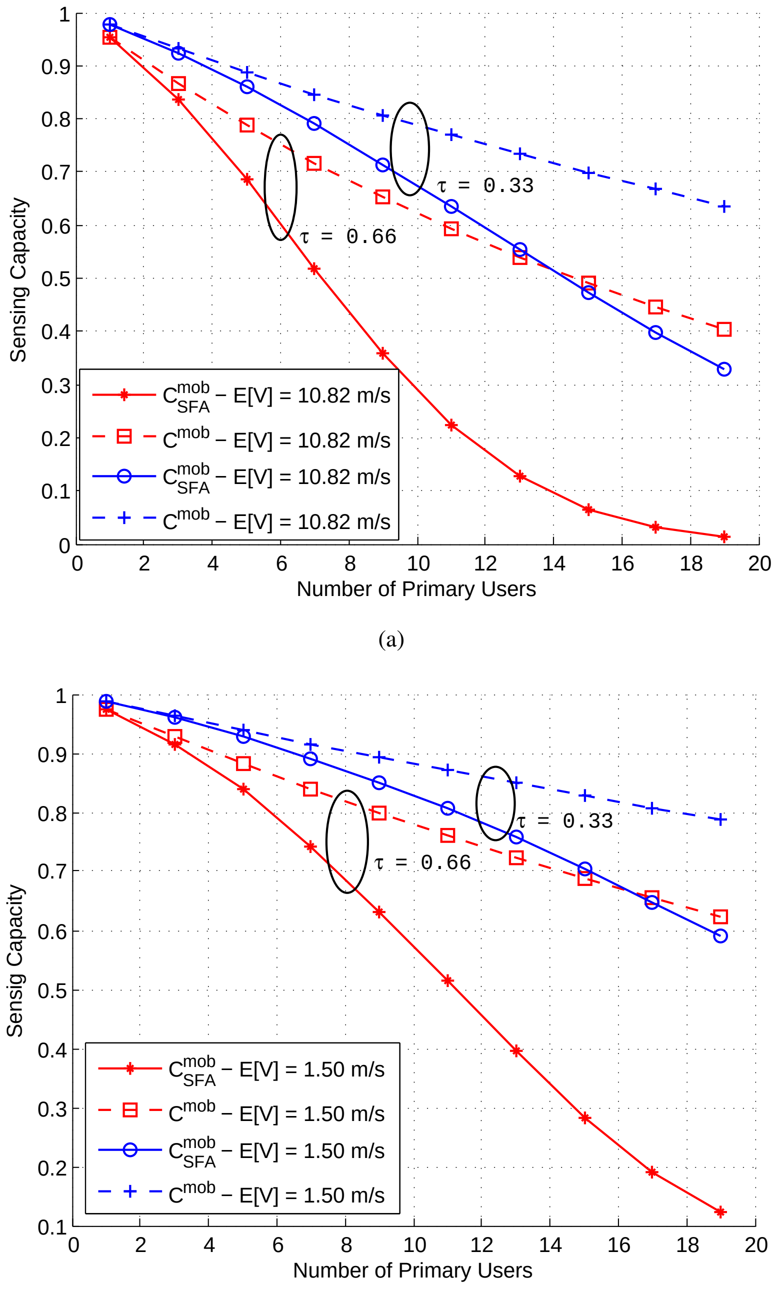

(a)

(b)

Figure 6.2: Sensing Capacity for different levels of PU's activity (τ): (a) high mobility scenario (E[V] = 10.82m/s); (b) low mobility scenario (E[V] = 1.50m/s).

6.2 Wireless-Powered Communications

Wireless-powered communications (WPC) have been recently proposed to extend the network's lifetime. In WPCs, the aggregate energy collected by a harvester node from multiple RF signals is used to power the communication process.

The effect of the interference on the performance of energy harvesting systems has been analyzed in [GA15] and [Che16]. The interference caused by multiple transmitters was characterized in [Fli+15], which considers that different ambient RF energy sources cause interference to a wireless sensor node.

Most of the existing works do not address large scale WPC networks due to the challenges associated with the characterization of the harvested RF energy in the presence of dominant transmitters.

The characterization of WPC systems that harvest energy from multiple coexisting networks (including static and/or mobile ones), has not yet been addressed in the literature. In order to fill this gap that exists in the literature, and using the results of Chapter 5, this section aims to first study the distribution of the harvested energy from multiple energy sources belonging to different coexisting networks. We consider the case where mobile and/or static networks may coexist together in the same band. Admitting that the harvester node acts as a transmitter after the energy harvesting period, we derive the outage probability for such scenario. In addition, we study the throughput achieved by the harvester node, identifying the optimal energy harvesting time allocation having into account the mobility of the mobile networks, the features of the static networks, the energy harvesting process, as well as the communication performance between the harvester node and the receiver.

6.2.1 Network scenario

We consider a WPC network with a time-switching protocol. In particular, wireless energy transfer is assumed in the downlink (DL) band, where the node N_{Tx} accumulates energy from the transmitters of the v different coexisting wireless networks (Figure 6.3). The node N_{Tx} first harvests energy during the time interval cT from the DL RF band, and then uses it to transmit data to N_{Rx} over the uplink (UL) band. The transmission lasts $(1-c)T$, where T is the total duration of a time-switching cycle and c represents the time splitting factor. We consider an unitary cycle duration, i.e., $T = 1$.

A Rayleigh fading channel between the nodes N_{Tx} and N_{Rx} is considered, and the distance between the nodes is denoted as d_1. The transmission power for information transfer depends on the energy harvested in the DL band and is denoted by $P_{N_{Tx}}$. Consequently, the signal received by N_{Rx} can be written as

$$y_{N_{Rx}} = \frac{1}{\sqrt{{d_1}^{\wp}}}\sqrt{P_{N_{Tx}}}h_1 x_c + n_d, \tag{6.10}$$

where h_1 is the channel coefficient from the transmitter N_{Tx} to the receiver N_{Rx}, x_c is the normalized information signal transmitted by N_{Tx}, and n_d is the zero-mean AWGN at the receiver.

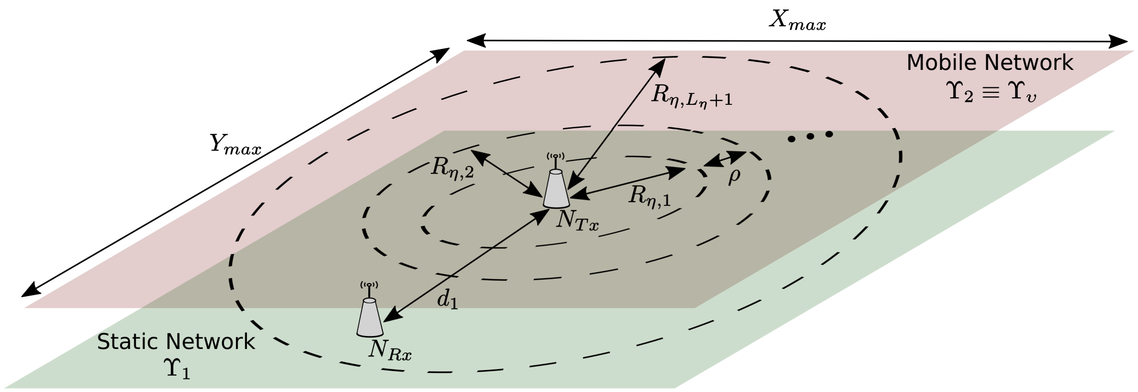

Figure 6.3: A harvester node N_{Tx} receives energy from v coexistent networks to transmit information to the node N_{Rx}. The dashed circles represent the boundaries of the annuli considered in the proposed model. The inner circle radius is denoted by $R_{\eta,1}$, and $R_{\eta,L_\eta+1}$ denotes the outer circle radius.

6.2.2 Harvested Energy

Considering the methods that characterize the aggregate interference in coexisting networks, derived in Chapter 5, the aggregate power received by N_{Tx} from all transmitters of the v coexisting networks can also be approximated by an α-μ distribution. Thus, the PDF of the aggregate power received from all transmitters of the coexisting networks (I_{agg}) can be approximated by an α-μ distribution as follows

$$f_{I_{agg}}(y) \approx \frac{\alpha \mu^{\mu} y^{\alpha\mu-1}}{\hat{r}^{\alpha\mu}\Gamma(\mu)} \exp\left(-\mu \frac{y^{\alpha}}{\hat{r}^{\alpha}}\right). \tag{6.11}$$

Then, the aggregate power is used to derive the energy harvested during the harvesting period cT. Therefore, the harvested energy at the node N_{Tx}, E_h, is written as

$$E_h = \varsigma c T I_{agg}, \tag{6.12}$$

where $0 < \varsigma < 1$ represents the energy conversion efficiency, and the RV I_{agg} follows an α-μ distribution with α, μ and $\hat{r}$ computed from (5.9), (5.10), and (5.11).

6.2.3 Throughput Analysis

After having harvested energy during the harvesting period cT, the node N_{Tx} transmits data in the UL band with $P_{N_{Tx}}$ power, represented by

$$P_{N_{Tx}} = \frac{E_h}{(1-c)T} = \varsigma I_{agg} \frac{c}{(1-c)}. \tag{6.13}$$

Using (6.10), the Signal-to-Noise Ratio (SNR) at the receiver node can be defined as

$$\gamma_d = \frac{P_{N_{Tx}} |h_1|^2}{{d_1}^{\wp} \sigma_{n_d}^2}, \tag{6.14}$$

where $\sigma_{n_d}^2$ is the variance of the zero-mean AWGN. Considering a Rayleigh channel with mean power $2\sigma_h^2$ between the nodes N_{Tx} and N_{Rx}, $|h_1|^2$ is exponentially distributed with parameter

$1/(2\sigma_h^2)$. Given a SNR threshold γ_0, the outage probability of the transmission can be written as

$$P_{out}(\gamma_0) = \mathrm{P}(\gamma_d < \gamma_0) = \int_0^{\gamma_0} f_{\gamma_d}(z)dz. \tag{6.15}$$

Using (6.14), and considering the PDFs of I_{agg} and $|h_1|^2$, (6.15) can be rewritten as

$$P_{out}(\gamma_0) = \frac{\alpha\mu^{\mu}}{\hat{r}^{\alpha\mu}\Gamma(\mu)}\frac{1}{\Lambda}\int_0^{\gamma_0}\int_0^{\infty}\frac{1}{y}\left(\frac{z}{y}\right)^{\alpha\mu-1}\exp\left(\frac{-\mu z^{\alpha}}{(\hat{r}y)^{\alpha}} - \frac{1}{2\sigma_h^2\Lambda}y\right)dy\,dz, \tag{6.16}$$

where

$$\Lambda = \frac{\varsigma c}{(1-c)d_1{}^{\wp}\sigma_{n_d}^2}$$

is the scaling value of the product of the RVs I_{agg} and $|h_1|^2$. Since the integral in (6.16) can only be numerically solved, we propose to approximate $P_{out}(\gamma_0)$ by an α-μ distribution as follows

$$P_{out}(\gamma_0) \approx \Gamma\left(\mu_p, \mu_p\left(\frac{\gamma_0}{\hat{r}_p\Lambda}\right)^{\alpha_p}\right)\frac{1}{\Gamma(\mu_p)}, \tag{6.17}$$

where α_p, μ_p and $\hat{r}_p$ can be obtained by solving the system of equations formed by (5.9), (5.10) and (5.11), substituting the symbols $\alpha, \mu, \hat{r}$, and $\mathrm{E}[I_{agg}{}^n]$ by $\alpha_p, \mu_p, \hat{r}_p$, and

$$\mathrm{E}[(I_{agg}|h_1|^2)^n] = n!(2\sigma_h^2\hat{r})^n\frac{\Gamma(\mu+n/\alpha)}{\mu^{n/\alpha}\Gamma(\mu)}, \tag{6.18}$$

respectively. As will be seen, (6.17) shows to be a very tight approximation, being evaluated instantaneously. (6.18) represents the n-th moment of the product of the RVs I_{agg} and $|h_1|^2$. Assuming a communication rate $\mathcal{R}$ (in bits/T) and the transmission duration $(1-c)T$, the throughput of the communication channel between N_{Tx} and N_{Rx} can be written as

$$R_{\tau}(c) = (1 - P_{out}(\gamma_0))(1-c)\mathcal{R}. \tag{6.19}$$

From (6.19), one can notice that $(1-P_{out}(\gamma_0))$ increases with c. However, the transmission duration decreases with c. This fact has motivated us to derive the optimal time allocation ratio, c^*, that maximize $R_{\tau}(c)$, given by

$$c^* = \arg\max_{0<c<1} R_{\tau}(c).$$

Thus, c^* can be determined by computing the root of the partial derivative $\frac{\partial R_{\tau}(c)}{\partial c}$. Departing from the partial derivative, the solution of $\frac{\partial R_{\tau}(c)}{\partial c} = 0$ only can be computed in a numerical way, finding the value c^* for which the condition (6.20) holds.

$$\alpha_p\left(c^*\Gamma(\mu_p)\right)^{-1}\exp\left(\mu_p\left(\frac{\gamma_0 d_1{}^{\wp}\sigma_{n_d}^2}{\hat{r}_p\varsigma}\frac{1-c^*}{c^*}\right)^{\alpha_p}\right) = 1 - (\Gamma(\mu_p))^{-1}\Gamma\left(\mu_p, \mu_p\left(\frac{\gamma_0 d_1{}^{\wp}\sigma_{n_d}^2}{\hat{r}_p\varsigma}\frac{1-c^*}{c^*}\right)^{\alpha_p}\right) \tag{6.20}$$

6.2.4 Model Validation and Discussions

We consider the same coexisting scenarios adopted in Subsection 5.6.3, with two coexisting networks ($\upsilon = 2$): a static network (Υ_1), and a network (Υ_2) where the nodes move according to the RWP. Three different mobility scenarios are analysed for Υ_2, considering the case where nodes are static ($\mathrm{E}[V] = 0$ m/s), or mobile with different average velocities ($\mathrm{E}[V] = \{10.82, 1.50\}$ m/s).

The parameters adopted in the validation are presented in Table 6.2, which are divided in the parameters related with the "Propagation Effects", the parameters of the network Υ_1 ("Static Network"), the parameters of the network Υ_2 ("Mobile Network"), and other parameters adopted in the WPC model, SCM, and simulations.

Table 6.2: Parameters adopted in the simulations.

Propagation Effects	P_{Tx_η}	10^3 mW	$\wp$	2
	σ_ξ	0.69	${\sigma_h}^2$	1/2
	$\sigma^2_{n_d}$	0.01 mW		

Static Network (Υ_1)	$R_{1,1}$	20 m	$R_{1,L_\eta+1}$	120 m
	ρ_1	20 m	L_1	5
	λ_1 (node/m^2)	1×10^{-4}		

Mobile Network (Υ_2)	$R_{2,1}$	20 m	$R_{2,L_\eta+1}$	120 m
	ρ_2	20 m	L_2	5
	V_{min}	5 m/s	V_{max}	20 m/s
	n_2	100	τ_2	1
	$\mathrm{E}[V]$	$\{10.82, 1.50, 0\}$ m/s	X_{max}	1000 m
	T_p	$\{0, 300, 3000\}$ s	Y_{max}	1000 m

Others	Monte Carlo samples	3×10^6	d_1	5 m
	γ_0	$\{-10, -5, 0, 5, 10, 15\}$ dB	ς	1
	L_N	10	υ	2

The assessment of the model is carried out by comparing Monte Carlo simulation results with numerical results of the throughput ($R_\tau(c)$ computed with (6.19)), and the optimal time allocation ratio (c^*computed with (6.20)). In the SCM, we have considered the same circular area for both networks Υ_1 and Υ_2, i.e., $R_{1,1} = R_{2,1} = 20$ m, $R_{1,L_\eta+1} = R_{2,L_\eta+1} = 120$ m, and $\rho_1 = \rho_2 = 20$ m.

Table 6.3 presents the α-μ distribution parameters adopted in (6.11) to approximate I_{agg} for the different average velocities $\mathrm{E}[V]$.

The throughput (R_τ) is achieved by the WPC system in the same coexisting scenarios adopted in Subsection 5.6.3. To characterize R_τ we have considered the optimal energy conversion efficiency of the energy harvesting process ($\varsigma = 1$), the communication range $d_1 = 5$ m, and the SNR threshold $\gamma_0 = 5$ dB at the receiver. Moreover, it is assumed that N_{Tx} uses all the harvested

Table 6.3: Parameters estimated for the model curves of I_{agg}.

		α	μ	$\hat{r}$
	E$[V] = 10.82$ m/s	0.198	49.032	2.946
	E$[V] = 1.50$ m/s	0.263	19.548	1.881
	E$[V] = 0$ m/s	0.275	16.621	1.714

energy to transmit the information. In Figure 6.4, we present different curves of the throughput as a function of the time splitting ratio c. The numerical results (represented by the “Model" curves) have considered the approximation proposed in (6.17) to compute the outage probability. The parameters used in (6.17) were previously computed as described in Section 6.2.3, and their values for the different mobility scenarios are presented in Table 6.4.

Table 6.4: Parameters estimated for the model curves of P_{out}.

		α_p	μ_p	$\hat{r}_p$
	E$[V] = 10.82$ m/s	0.316	6.098	2.199
	E$[V] = 1.50$ m/s	0.287	6.350	1.347
	E$[V] = 0$ m/s	0.284	6.288	1.216

The throughput, computed with (6.19), is close to the throughput obtained in the Monte Carlo simulations, as illustrated in Figure 6.4. The results show that higher throughput values are achieved for higher mobility scenarios of the RWP network Υ_2. This is because the amount of harvest energy increases with the velocity of the nodes of the network Υ_2, as justified by the aggregate power results in Figure 5.7. Moreover, it is shown that the parameter c effectively impacts on the achieved throughput, clearly identifying an upward where extending the harvesting period increases the transmission power, and a downward zone, where the extension of the harvesting period shortens the transmission period. The optimal point of operation is the one that divide the two zones.

To evaluate the optimal time allocation ratio (c^*) proposed in (6.20), we have considered the higher mobility scenario (E$[V] = 10.82$ m/s), and multiple SNR thresholds ($\gamma_0 = \{-10, -5, 0, 5, 10, 15\}$ dB). The simulation results of the throughput and the numerical results of the optimal time allocation ratio (c^*) are illustrated in Figure 6.5 (a marker “o" was adopted to indicate the c^* value numerically computed with (6.20)). The throughput inversely increases with γ_0, as expected. We also observe that γ_0 also impacts on the shape of the throughput curves. However, the optimal time allocation ratio is accurately approximated by (6.20) for all γ_0 values, as depicted in the figure.

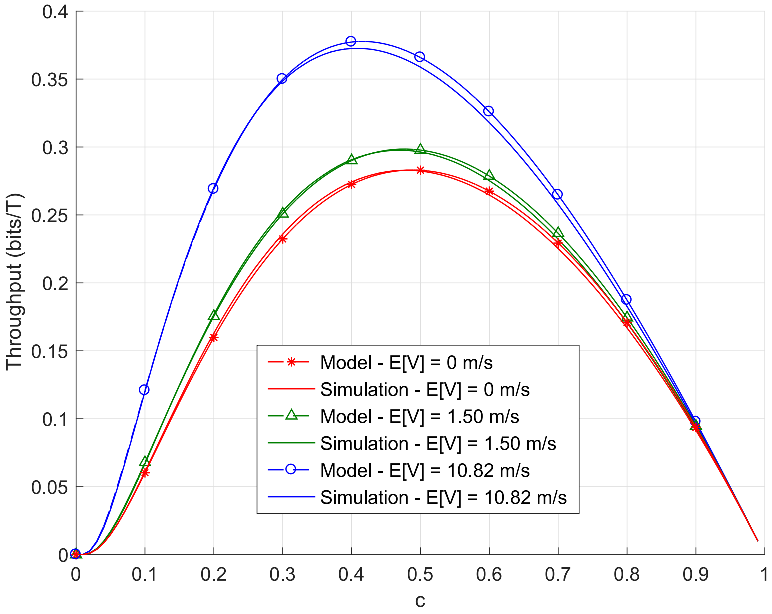

Figure 6.4: Throughput R_τ for the scenario considered in Figure 5.7.

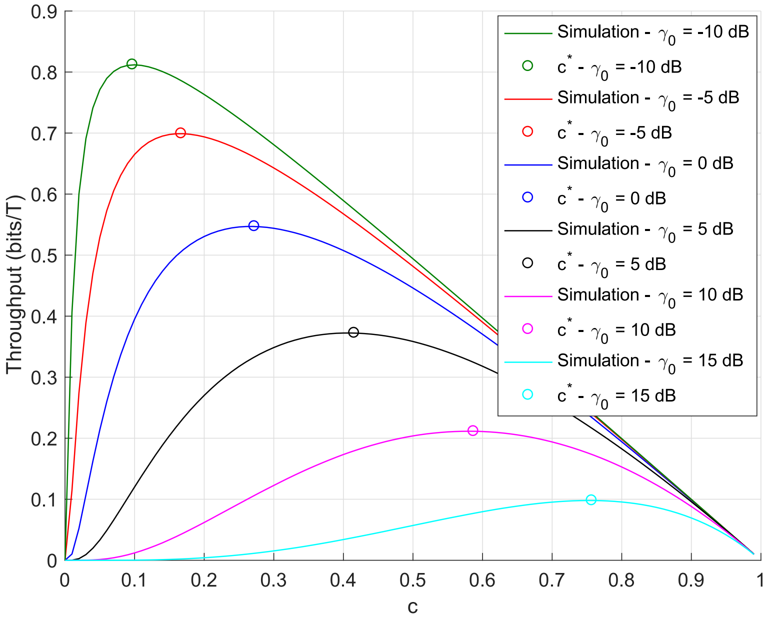

Figure 6.5: Optimal time allocation ratio c^* for different SNR thresholds γ_0 .

6.3 Impact of Carrier Sensing Range in CSMA Networks

Nowadays, due to the densification of the wireless networks, the carrier sense multiple access (CSMA) protocol has become very popular. To improve the network capacity and providing spectrum reuse, the CSMA mechanism allows multiple transmissions using the spatial separation between them [Jam+15]. Generally, the carrier-sensing range is statically defined to improve the spatial reuse, and at the same time to ensure interference-safe transmissions [TM14].

There have been previous works on the proper setting of the carrier-sensing range [JS06; Ma+09]. However, these works assumed simplified interference models, where the realistic physical layer characteristics are ignored and the distribution of the interfering nodes is deterministic. More recently, [Cha+17] proposed two carrier-sensing adaptive methods for the cumulative interference and the incremental interference, but the convergence rate of the proposed algorithm is a problem when the node density is low and the nodes' mobility is high. Based on the effects of the cumulative interference and the dominant pairwise interference in the network, [Din+17] investigated the impact of the carrier-sensing range on the link performance in a dense wireless network. However, the authors do not propose a solution to determine the optimal carrier-sensing value.

Motivated by the lack of literature on the derivation of methods to compute the optimal carrier-sensing range in a coexistence wireless scenario with fading effects, and taking into account the effects of the cumulative interference, in this section we investigate the impact of the carrier-sensing range on the access probability of a transmitter node, which is under the aggregate interference of coexistent multiple access wireless networks. Moreover, we identify the optimal carrier-sensing range for two different scenarios, considering the cases when the coexisting networks are spatially overlapped or non-overlapped.

6.3.1 Network Scenario

We consider a network scenario where a number of transmitters are randomly deployed according to a homogeneous PPP. Transmitting nodes of the network Υ_1 (blue nodes) and Υ_2 (red nodes) are scattered in the plane with average density λ_1 (blue nodes) and λ_2 (red nodes), respectively. The system considered in this section is depicted in Figure 6.6. Each node deployed in the circular region between the inner radius $R_{\eta,1}$ and outer $R_{\eta,L_{\eta+1}}$ operates as a fixed interferer, causing interference to a central node N_c located at position (x_{N_c}, y_{N_c}). The transmitters of networks Υ_1 and Υ_2 access the channel with probability τ_1 and τ_2, respectively. The transmitted power level is constant and equal for all transmitting nodes of a given network Υ_η, and it is also considered path-loss for each signal received by the central node. The fading gain is assumed to be independent and identically distributed (i.i.d) Rayleigh fading with unitary mean, and the shadowing gain follows a Lognormal distribution with unitary mean.

In a first phase, the node N_c uses the CSMA protocol to control the channel access, and it can only transmit if it senses no other active transmissions in its vicinity. More specifically, the node N_c only transmits when the received aggregate power from interfering nodes is below a carrier-sensing

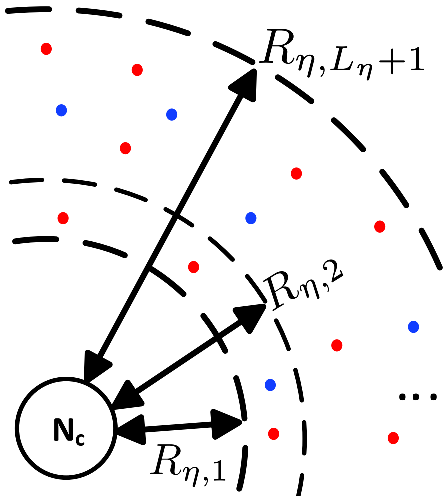

Figure 6.6: A receiver N_c suffers interferece from two coexistent networks.

threshold (γ_{cs}), i.e.,

$$I_{agg} < \gamma_{cs}. \tag{6.21}$$

Admitting that after being able to access the channel, the node N_c transmits with a certain power transmission level, P_{Tx}, the carrier-sensing threshold (γ_{cs}) can be mapped to a carrier-sensing range (R_{cs}), as follows

$$R_{cs} = \left(\frac{P_{Tx}}{\gamma_{cs}}\right)^{1/\wp}, \tag{6.22}$$

where $\wp$ represents the path-loss coefficient. If the distance between the node N_c and other concurrent transmitter N_{Tx} is greater than the carrier-sensing range,

$$d(N_c, N_{Tx}) \geq R_{cs}, \tag{6.23}$$

then N_c and N_{Tx} can not carrier sense each other, and thus can initiate concurrent transmissions.

When the carrier-sensing range is too high, it means that the carrier-sensing threshold is too low (too sensitive). In this case, when multiple transmitters distanced from the central node access the channel, the cumulative interference caused to N_c can be easily above the threshold due to the number of transmitters, and in that case N_c interprets the medium/channel as being busy. This shows that the spatial density of transmitters outside the carrier-sensing range may undesirably inhibit the central node to access the channel. Contrarily, if the carrier-sensing range is decreased, it means that the carrier-sensing threshold increases (not so sensitive). Assuming that the transmission range of a concurrent transmitter is higher than the carrier-sensing range of the node N_c a collision may occur. The node N_c cannot detect the concurrent transmission, because the carrier-sensing threshold is too high, and starts a simultaneous transmission due to the fact of having declared the channel as being idle. Consequently, R_{cs} should be parameterized to find the best tradeoff between the avoidance of unnecessary inhibition of channel access (due to a low carrier-sensing threshold) and the avoidance of high number of concurrent transmissions per area (collisions due to a high carrier-sensing threshold). In the next subsection, we derive a utility function to help finding a value that better balances the identified tradeoff.

6.3.2 Carrier Sensing Range Optimization

Considering the methods that characterize the aggregate interference in coexisting networks, derived in Chapter 5, the aggregate power received by the node N_c from all transmitters of the v coexisting networks can also be approximated by an α-μ distribution. Thus, the PDF of the aggregate power received from all transmitters of the coexisting networks (I_{agg}) can be approximated by an α-μ distribution as follows

$$f_{I_{agg}}(y) \approx \frac{\alpha \mu^{\mu} y^{\alpha\mu-1}}{\hat{r}^{\alpha\mu}\Gamma(\mu)} \exp\left(-\mu \frac{y^{\alpha}}{\hat{r}^{\alpha}}\right). \tag{6.24}$$

The aggregate power distribution can be used to derive the medium access probability of N_c, given by

$$P_{acc}(\gamma_{cs}) = \mathrm{P}(I_{agg} < \gamma_{cs}) = \int_0^{\gamma_{cs}} f_{I_{agg}}(z)dz. \tag{6.25}$$

Observing the accuracy of the approximation results in Chapter 5, we propose to approximate $P_{acc}(\gamma_{cs})$ by the CDF of the α-μ distribution, as follows

$$P_{acc}(\gamma_{cs}) \approx \Gamma\left(\mu, \mu\left(\frac{\gamma_{cs}}{\hat{r}_p}\right)^{\alpha}\right)\frac{1}{\Gamma(\mu)}. \tag{6.26}$$

To investigate the carrier-sensing tradeoff we define an utility function that takes into account the medium access probability of the node, and at the same time the carrier-sensing range. The utility function is defined as follows,

$$C_{cs} = P_{acc}R_{cs}, \tag{6.27}$$

which can be maximized in order to increase the medium access probability of the node and simultaneously increase the carrier-sensing range. We highlight that the increase of the carrier-sensing range decreases the number of collisions per spatial area unit, which increases the transport capacity, i.e. the capacity of transmitting bits/Hz farther away. Replacing (6.26) in (6.27), and using (6.23) to express γ_{cs} as a function of the carrier-sensing range ($\gamma_{cs} = P_{Tx}{R_{cs}}^{-\wp}$), the carrier-sensing metric can be rewritten as

$$C_{cs} \approx \Gamma\left(\mu, \mu\left(\frac{P_{Tx}{R_{cs}}^{-\wp}}{\hat{r}_p}\right)^{\alpha}\right)\frac{R_{cs}}{\Gamma(\mu)}. \tag{6.28}$$

From (6.28), one can notice that P_{acc} decreases with R_{cs}. However, C_{cs} in (6.27) is also written as a function of R_{cs}, apart from P_{acc}. This fact has motivated us to derive the optimal carrier-sensing range, ${R^*}_{cs}$, that maximize C_{cs}, given by

$${R^*}_{cs} = \arg \max_{0<R_{cs}<\infty} C_{cs}.$$

Thus, ${R^*}_{cs}$ can be determined by computing the root of the partial derivative $\frac{\partial C_{cs}}{\partial R_{cs}}$. Departing from the partial derivative, the solution of $\frac{\partial C_{cs}}{\partial R_{cs}} = 0$ only can be computed in a numerical way, finding the value ${R^*}_{cs}$ for which the following equality holds.

$$\alpha\wp\Gamma(\mu)^{-1}\exp\left(-\mu\left(\frac{P_{Tx}{R_{cs}}^{-\wp}}{\hat{r}_p}\right)^{\alpha}\right)\left(\mu\left(\frac{P_{Tx}{R_{cs}}^{-\wp}}{\hat{r}_p}\right)^{\alpha}\right)=\Gamma(\mu)^{-1}\Gamma\left(\mu,\mu\left(\frac{P_{Tx}{R_{cs}}^{-\wp}}{\hat{r}_p}\right)^{\alpha}\right) \tag{6.29}$$

6.3.3 Model Validation and Discussions

In this section, we validate the methodology described in Section 6.3.2, by comparing the optimal carrier-sensing range (${R^*}_{cs}$) proposed in (6.29) with simulations. Simulation and numerical results are presented for 2 coexisting static networks, i.e. $\upsilon = 2$. Different node densities of network Υ_1 ($\lambda_1 = 1 \times 10^{-4}$ nodes/m^2) and Υ_2 ($\lambda_2 = 2 \times 10^{-4}$ nodes/m^2) are considered. Two different operational scenarios of networks Υ_1 and Υ_2 are considered:

- in the "Overlapped Scenario" the transmitters of the two networks are allowed to operate between $R_{1,1} \equiv R_{2,1}$ and $R_{1,4} \equiv R_{2,4}$, i.e., the nodes of both networks coexist in the same spatial region;
- in the "Non-Overlapped Scenario" the two networks operate in disjoint spatial regions ($R_{1,L\eta+1} \equiv R_{2,1}$) .

The parameters adopted in the validation are presented in Table 6.5.

Table 6.5: Parameters adopted in the simulations.

Monte Carlo samples	3×10^6	$\wp$	2
λ_1 (node/m^2)	1×10^{-4}	λ_2 (node/m^2)	2×10^{-4}
τ_1	1	τ_2	1
ρ	20 m	σ_ξ	0.69
υ	2	P_{Tx_η}	10^3 mW

Overlapped Scenario	$R_{1,1}$	20 m	$R_{2,1}$	20 m
	$R_{1,L\eta+1}$	80 m	$R_{2,L\eta+1}$	120 m
	L_1	3	L_2	5

Non-Overlapped Scenario	$R_{1,1}$	20 m	$R_{2,1}$	80 m
	$R_{1,L\eta+1}$	80 m	$R_{2,L\eta+1}$	120 m
	L_1	3	L_2	2

The parameters used in (6.29) were previously computed as described in Chapter 5, and their values for the two different operational scenarios are presented in Table 6.6.

The simulation results of the carrier-sensing metric (C_{cs}) and the numerical results of the optimal carrier-sensing range (${R^*}_{cs}$) are illustrated in Figure 6.7(a) (a marker "o" was adopted to indicate the ${R^*}_{cs}$ value numerically computed with (6.29)). From the Figure, we observe that the

Table 6.6: Parameters estimated for the model curves.

		α	μ	$\hat{r}$
Figure 6.7(a)	Non-Overlapped	0.200	25.186	0.949
	Overlapped	0.298	17.464	2.520

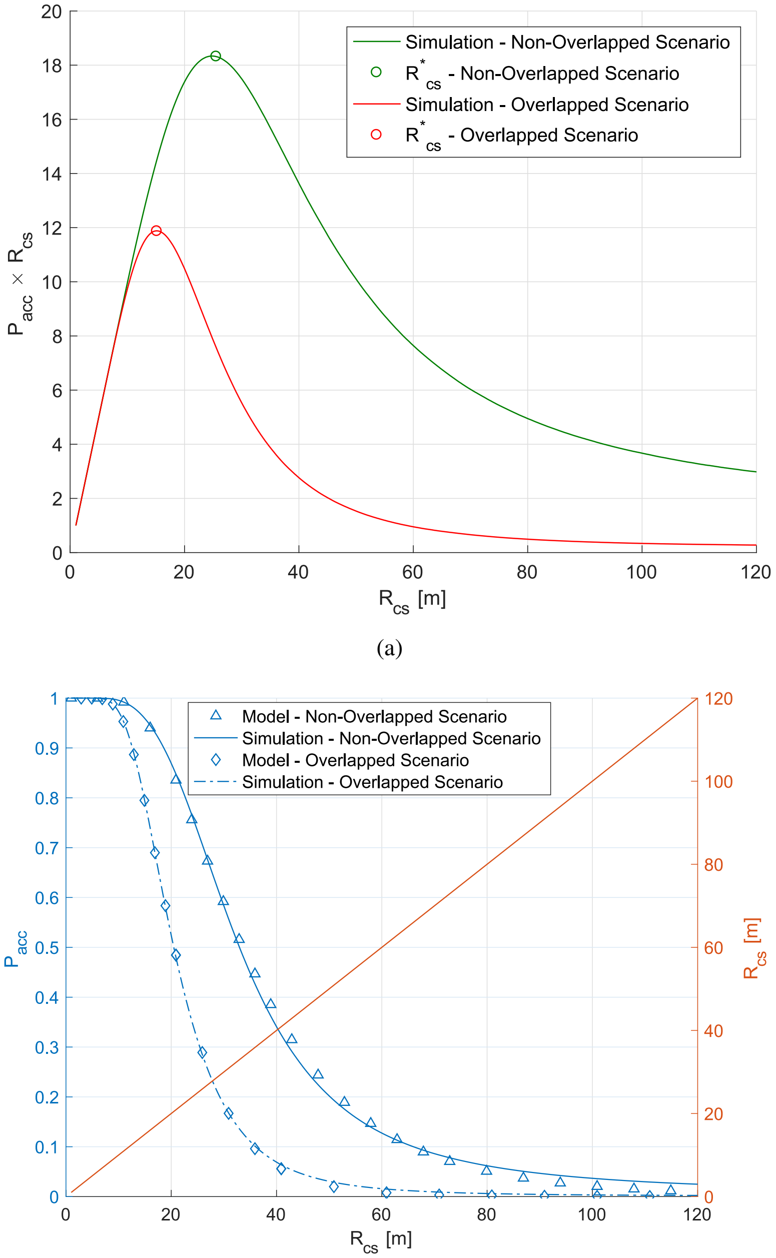

(a)

(b)

Figure 6.7: Carrier-sensing range optimization: (a) Optimal carrier-sensing range; (b) Medium access probability (P_{acc}) and carrier-sensing range (R_{cs}).

higher optimal carrier-sensing range value is achieved for the “Non-Overlapped Scenario”. This is because in the “Non-Overlapped Scenario” less interference is caused to the central node N_c in comparison with the “Overlapped Scenario”, since the density of nodes in the “Non-Overlapped Scenario” is also lower. Moreover, for the “Overlapped Scenario” the optimal carrier-sensing range is smaller than the inner radius of interference region. The results also show that the optimal carrier-sensing range is accurately approximated by (6.29) for the two scenarios.

As observed from Figure 6.7(a), the carrier-sensing metric (C_{cs}) admits a maximum value for each scenario, and this result can be explained by the Figure 6.7(b). As can be seen in the Figure 6.7(b), the medium access probability (P_{acc}) has a significant impact on the carrier-sensing metric, since the utility function varies linearly with the carrier-sensing range. From Figure 6.7(b) we clearly identify a slight decrease on the medium access probability with the carrier-sensing range, which results in a upward zone on the carrier-sensing metric showed in Figure 6.7(a). After $R^{*}{}_{cs}$, the medium access probability strongly decreases, resulting in a downward zone on the carrier-sensing metric.

6.4 Residual self-interference estimation

The success of IBFDX communications relies on the performance of SIC schemes. Since the transmitted signal may suffer different propagation effects, a terminal cannot simply cancel the SI by subtracting its transmitted signal from the received one. Rather, DC must be employed to account for the estimated effects of the propagation channel [AE15a; Kor+14b]. In this way, the knowledge of the residual SI due to the AC is crucial to design efficient SI estimation methods to be used in the digital-domain. Motivated by this fact, we describe the steps required to estimate the distribution of the residual SI. Moreover, we evaluate the impact of the length of the sample set in the accuracy of the estimation process.

6.4.1 System Model

We consider an IBFDX scheme adopting an active analog canceler that reduces the SI at the carrier frequency. The active analog canceler actively reduces the self-interference by injecting a canceling signal into the received signal, as was considered in Chapter 4. Considering the case when the channel gain is time-varying and admitting a Rician fading SI channel, we adopt the Lemma 4.3.1 to derive a estimation method for the distribution of the residual SI with a set of samples. Given a sample set of observations of the residual SI, we derive the residual SI fitting the two parameters required in (4.8) via matching the first two moments.

6.4.2 Residual SI Estimation Method

Next, we estimate the residual SI power applying the method of moments. The i-th moment of the residual SI distribution denoted by M_i, can be obtained through the Riemann–Stieltjes integral, as follows

$$M_i = \int_0^\infty z^i f_{P_{y_{r_{si}}}}(z) dz, \tag{6.30}$$

where $f_{P_{y_{r_{si}}}}$ represents the PDF of the SI power. Using the PDF of the SI power derived in Lemma 4.3.1, and consequently replacing $f_{P_{y_{r_{si}}}}$ in (6.30) by (4.8), we obtain

$$M_i = \frac{2^i \, \Gamma(1+i) \, \lambda_A^i \, \sigma_x^{2i} \, \Gamma(i+k_h)}{\Gamma(k_h)}. \tag{6.31}$$

Using (6.31), we derive the first and second moments of $P_{y_{r_{si}}}$, which are respectively given by

$$\begin{cases} M_1 = 2 \, k_h \, \lambda_A \, \sigma_x^2 \\ \\ M_2 = 8 \, k_h \, (1+k_h) \, \lambda_A^2 \, \sigma_x^4 \end{cases}. \tag{6.32}$$

Since the variance of the SI signal (σ_x) can be determined locally at the analog canceler, to parametrize the residual SI distribution we only need to know the parameters k_h and λ_A. Solving the system of equations (6.32) we obtain

$$k_h = -\frac{2M_1^2}{2M_1^2 - M_2}, \tag{6.33}$$

$$\lambda_A = \frac{-2M_1^2 + M_2}{4M_1\sigma_x}. \tag{6.34}$$

To estimate the residual SI distribution, we periodically acquire samples of the residual SI. Representing the residual SI sample set by $\mathcal{X} = \{S_1, S_2, ..., S_m\}$, where $S_1, S_2, ..., S_m$ are the m samples, we apply the operators $\mathrm{E}[\mathcal{X}]$ and $\mathrm{E}[\mathcal{X}^2]$ to estimate the first ($\hat{M}_1$) and second ($\hat{M}_2$) moments, respectively. After that, the estimators ($\hat{k_h}, \hat{\lambda_A}$) of the parameters ($k_h, \lambda_A$), can be computed by (6.33) and (6.34), replacing (M_1, M_2) by ($\hat{M}_1$, $\hat{M}_2$) and (k_h, λ_A) by ($\hat{k_h}$, $\hat{\lambda_A}$).

To evaluate the impact of the length of the sample set m in the estimation, in the next subsection we analyze the accuracy of the estimation method for different values of m.

6.4.3 Model Validation and Discussions

Several simulations were parameterized according the data in Table 6.7 to evaluate the accuracy of the estimation method. The entire sample set was obtained using the Monte Carlo method during 200 μs of simulation time (72×10^6 samples were collected for the entire sample set). The up-conversion frequency was parametrized to $\omega_c = 2\pi \times 10^9$ rad/s, i.e., the IBFDX communication system is operating at a carrier frequency of 1 GHz (equivalent to a period $T_c = 1$ ns). A sample period $\Delta_T = T_c/360$ was adopted. Three different parameterizations of the Rician fading channel were considered, i.e., $K_{dB} = [-10, 0, 10]$ dB, for a single value of phase estimation error ($\Xi = \pi/18$) and considering perfect estimation of the channel's gain ($\epsilon = 1$). To apply the estimation method we have considered different lengths of the sample set $\mathcal{X}$ ($m = \{100, 200, 500\}$). The samples of $\mathcal{X}$ are selected from the entire set with 72×10^6 samples. Considering a concrete length sample set m, the estimators of k_h and λ_A were computed through (6.33) and (6.34), respectively.

The model results and the results achieved with the estimation method considering different m values are illustrated in Figure 6.8. The "Model" curves were computed with (4.8), where k_h and λ_A were determined by (4.10) and (4.9), respectively. The estimated curves were also computed with (4.8). However, the estimators for k_h and λ_A were determined by (6.33) and (6.34). As expected, a larger set of samples allows more accurate results. However, we would like to highlight the quality of the estimation even when a small set of samples (m = 200) is adopted. Moreover, the estimation results obtained with 500 samples are close to the theoretical ones, confirming the quality of the proposed estimation model, and its drive in terms of practical application.

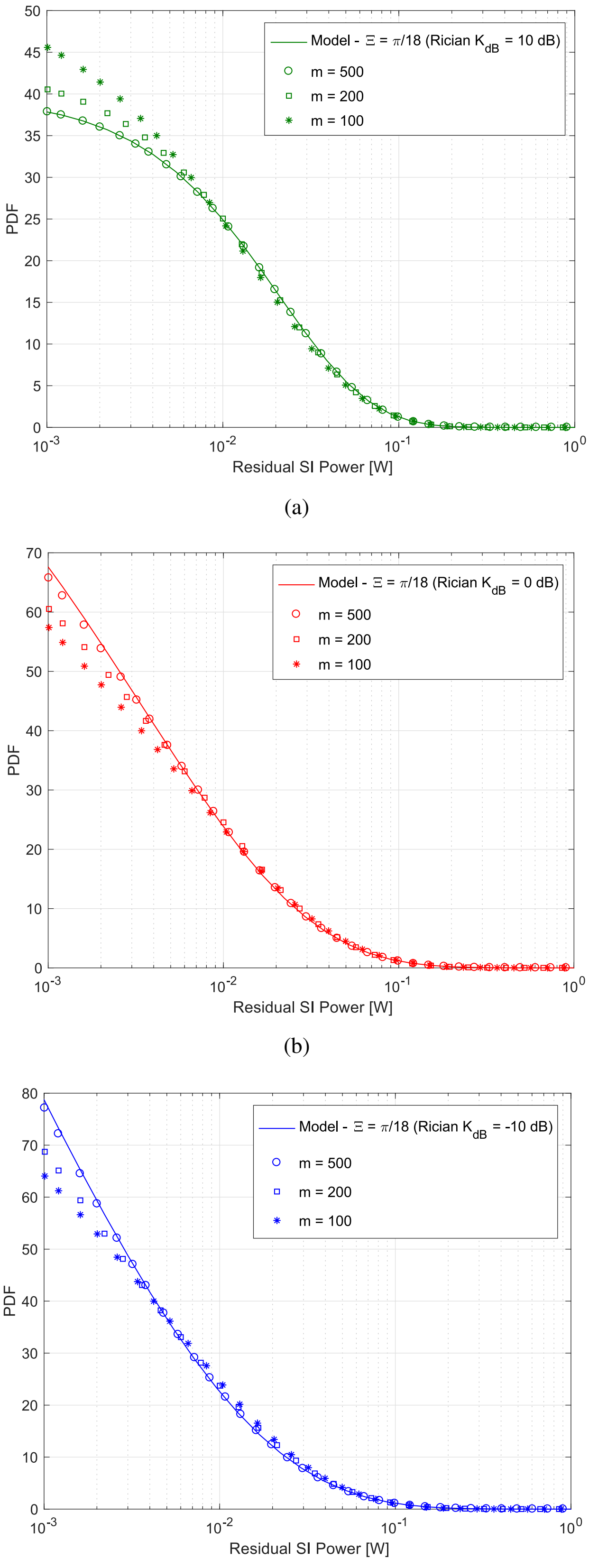

(a)

(b)

(c)

Figure 6.8: Estimation of the residual SI for different values of K_{dB} (Rician fading channel): (a) K_{dB} = 10 dB; (b) K_{dB} = 0 dB; (c) K_{dB} = -10 dB.

Table 6.7: Parameters adopted in the simulations.

f_c	1 GHz	ω_c	$2\pi \times 10^9$ rad/s
σ_x^2	$1/2$	Ξ	$\pi/18$
T_c	1 ns	ϵ	1
Δ_T	$1/360$ ns	Simulation time	200 μs
ϑ	$\pi/4$	K_{dB}	$\{-10, 0, 10\}$
Ω	1	m	$\{100, 200, 500\}$

CHAPTER 7

CONCLUSIONS AND FUTURE WORK

This chapter summarizes the major contributions and attained results of the thesis (Section 7.1) and discusses, in further detail, foreseen directions for future research on this topic (Section 7.2).

7.1 Conclusions

This thesis investigated the interference problem in the multiple access wireless networks, proposing new approaches to characterize the interference in multiple scenarios.

In an initial stage we have investigated the characterization of the wireless interference in a mobile ad hoc network, when the nodes move according to the RWP (Chapter 3). Since the interferers' location in the RWP model is not homogeneous, we have considered the SCM to approximate the spatial distribution of the mobile nodes to an IPP. The density of the spatial IPP was derived and validated through simulation data, showing that IPP modeling approaches can be adopted in RWP mobility scenarios simulated in a square/rectangular area. By assuming the IPP, we have derived the MGF of the aggregate interference when nodes move according to the RWP, providing a theoretical approximation for the aggregate interference distribution of the nodes located within an annulus, and the distribution of the aggregate interference when multiple annuli are considered. To evaluate the aggregate interference model we have compared the numerical results obtained with the model and the results obtained through simulation, considering path loss, fading and shadowing effects. The results showed that the proposed model achieves high accuracy even for different positions of the receiver node. The results confirm that the interference power increases with the average speed of the nodes and decreases when the receiver node is further away from the center of the simulated area. Based on the observation that the aggregate interference in a RWP network can be approximated by a GEV distribution, we have adopted a traditional MLE estimator and a PWM estimator to derive the missing parameters of the GEV distribution. Simulation results show that both estimators achieve high accuracy even for a low number of samples.

Assuming IBFDX communications, Chapter 4 developed a theoretical analysis of the residual SI power, which represents the amount of uncanceled SI due to channel estimation errors in the analog cancellation process. Specifically, we have derived closed form expressions for the distribution of the residual SI power when Rician and Rayleigh fading SI channels are considered. The distribution of the residual SI power was also derived for low and high channel gain dynamics, by considering the cases when the SI channel gain is time-invariant and time-variant. Numerical results computed with the proposed model were compared with Monte Carlo simulation results, in order to evaluate the accuracy of the theoretical analysis for both SI channel's gain and phase estimation errors. From the results, we observed that the SI power increases with the channel's gain and phase estimation errors. The results also showed that the channel dynamics strongly influences the distribution of the SI power and confirm that the type of fading channel strongly impacts the distribution of the residual SI power. The impact of the PN was also evaluated showing that the average of the residual SI power increases with the PN variance.

In Chapter 5, the problem of coexistence interference caused by multiple networks operating in the same band was considered. The model considers different spatial distributions of the coexisting networks, fast fading and shadowing propagation effects, as well as different transmission powers and medium access probabilities. Two different methods were derived to characterize the aggregate interference power caused to a receiver when the interferers belong to different coexisting networks. The first method developed in Chapter 5 approximates the aggregate interference by assuming that the interference caused by the transmitters located on a given annulus of the spatial region is approximated by a Gamma distribution. The second method proposed a highly accurate approximation based on the α-μ distribution, which holds for the entire spatial region of each coexisting network. The precisions of both methods was assessed through simulations, and it was shown that the second approach can efficiently increase the accuracy of the interference power distribution in coexistence networks.

Chapter 6 was dedicated to different applications of the interference models presented in Chapters 3, 4, and 5. The first application uses the knowledge of the aggregate interference distribution derived in Chapter 3 to define a new SC metric in CRNs with multiple mobile PUs. Contrarily to other works, we have assumed that PUs may also be detected active when they are located outside the SUs' sensing region (known as SFA effect). Moreover, it was shown that the decrease of the SC due to the SFA effect may be significant, namely when the number of PUs and the PU's activity increase. Finally, due to the mobility model, we have shown that the SC increases as the average velocity of the nodes decrease. This result indicates that the capacity of the SUs varies inversely with the velocity of the PUs. The second application investigated the impact of WPC when energy is harvested from multiple static and/or mobile wireless coexisting networks. First, the distribution of the harvested energy from multiple energy sources belonging to different coexisting networks was studied, benefiting from the derivation of coexistence interference in Chapter 5. Admitting that the harvester node acts as a transmitter after the energy harvesting period, we have derived the outage probability for such scenario. In addition, we have studied the throughput achieved by the harvester node, identifying the optimal energy harvesting time allocation having into account the mobility of the networks, the features of the static networks, the energy harvesting process, as well as the communication performance between the harvester node and the receiver. The results shown that higher throughput values were achieved for higher mobility scenarios of the RWP network. The third application derived a method to compute the optimal carrier-sensing range in a CSMA network. To investigate the optimal carrier-sensing range we have defined an utility function that takes into account the medium access probability of the node, and at the same time the carrier-sensing range. The optimal carrier-sensing range was identified for two different scenarios, considering the cases when the coexisting networks are spatially overlapped or non-overlapped. Finally, the fourth application derived a method to estimate the residual SI power in an IBFDX system. Considering the case when the channel gain is time-varying, and admitting a Rician fading SI channel, we have derived a estimation method for the distribution of the residual SI using a small set of samples. The impact of the sample set length was evaluated, showing that a larger set of samples increases the estimation accuracy, and the estimation method exhibits high accuracy even when a small set of samples is adopted.

7.2 Future Work

We identify many possible future directions for the work carried out during this thesis.

In Chapter 3 we have observed that the spatial distribution of the transmitter nodes impacts on the characterization of the aggregate interference. For this reason, as future work, different mobility models should be considered. The identification of reference mobility models with a particular focus on realistic mobility scenarios would also be an advantage in the forthcoming works.

The promising theoretical background developed in Chapter 4 presents the residual SI characterization when Rician and Rayleigh fading SI channels are considered. However, a single-tap delay channel is considered. In future research works it would be interesting also include the components yielded by multi-path scattering outside the transceiver, as well as the antenna reflection inside the transceiver. Therefore, the SI channel to be considered in the analog SI canceller should be described by a tapped-delay mode with at least two delay taps. Furthermore, the main hardware impairments should be considered in the derivation of closed-form expressions, including the oscillators' phase noise, the IQ imbalance, and the quantization noise.

Chapter 5 discusses two approaches for modeling interference in coexisting wireless networks, where the transmitted power level is constant and equal for all unlicensed users of a given network. Admitting that each of these users experience different network conditions and adopt a different transmit power, as a future work it would be interesting to develop an algorithm that dynamically adapts the transmitted power of each node based on the experienced interference.

The work developed in Section 6.1 investigates the impact of mobile PUs on the spectrum sensing capacity of one stationary SU assuming the SFA effect in a mobile CRN. A future study would bring novelty if a mobile SU is considered, instead of a stationary SU.

In Section 6.2, we developed a linear energy harvesting model, when energy is harvested from multiple static and/or mobile wireless coexisting networks. In a future study the linear energy harvesting model should be replaced by a practically-viable non-linear energy harvesting model.

Section 6.3 investigates the impact of the carrier-sensing range on the access probability of a half-duplex transmitter node in a CSMA network. A comparison of the optimal carrier-sensing results obtained in Section 6.3, with future results considering an IBFDX transmitter node would bring novelty for the current literature.

In Section 6.4, we presented a method to estimate the residual SI. However, it would be interesting to assess the estimation method to cancel the residual SI in real-time. Furthermore, a future research work should analyze the feasibility of the estimation method in the design of novel CSMA protocols.

To sum up, while significant progress has already been made in this field of research, various open research topics still require significant research efforts.

BIBLIOGRAPHY

[AK99] A. Abdi and M. Kaveh. "On the utility of gamma PDF in modeling shadow fading (slow fading)". In: *1999 IEEE 49th Vehicular Technology Conference (Cat. No.99CH36363)*. Vol. 3. 1999, 2308–2312 vol.3. DOI: 10.1109/VETEC.1999.778479.

[Abd+12] S. Abdollahvand, J. Goes, L. B. Oliveira, L. Gomes, and N. Paulino. "Low phase-noise temperature compensated self-biased ring oscillator". In: *Proc. IEEE Int. Symp. Circuits Syst.* Seoul, South Korea, 2012, pp. 2489–2492. DOI: 10.1109/ISCAS.2012.6271805.

[AS65] M. Abramowitz and I. Stegun. In: *Handbook of Mathematical Functions with Formulas, Graphs, and Mathematical Tables, New York: Dover* (1965).

[AE15a] E. Ahmed and A. M. Eltawil. "All-Digital Self-Interference Cancellation Technique for Full-Duplex Systems". In: *IEEE Transactions on Wireless Communications* 14.7 (2015), pp. 3519–3532. ISSN: 1536-1276. DOI: 10.1109/TWC.2015.2407876.

[AE15b] E. Ahmed and A. Eltawil. "On Phase Noise Suppression in Full-Duplex Systems". In: *IEEE Transactions on Wireless Communications* 14.3 (2015), pp. 1237–1251. ISSN: 1536-1276. DOI: 10.1109/TWC.2014.2365536.

[AAY10] S. Al-Ahmadi and H. Yanikomeroglu. "On the approximation of the generalized-K distribution by a gamma distribution for modeling composite fading channels". In: *IEEE Transactions on Wireless Communications* 9.2 (2010), pp. 706–713. ISSN: 1536-1276. DOI: 10.1109/TWC.2010.02.081266.

[AY10] M. Aljuaid and H. Yanikomeroglu. "Investigating the Gaussian Convergence of the Distribution of the Aggregate Interference Power in Large Wireless Networks". In: *IEEE Transactions on Vehicular Technology* 59.9 (2010), pp. 4418–4424. ISSN: 0018-9545. DOI: 10.1109/TVT.2010.2067452.

[Alo+01] M. . Alouini, A. Abdi, and M. Kaveh. "Sum of gamma variates and performance of wireless communication systems over Nakagami-fading channels". In: *IEEE Transactions on Vehicular Technology* 50.6 (2001), pp. 1471–1480. ISSN: 0018-9545. DOI: 10.1109/25.966578.

[BJ10] A. Babaei and B. Jabbari. “Interference Modeling and Avoidance in Spectrum Underlay Cognitive Wireless Networks”. In: *2010 IEEE International Conference on Communications*. 2010, pp. 1–5. DOI: `10.1109/ICC.2010.5501850`.

[Bet+03] C. Bettstetter, G. Resta, and P. Santi. “The node distribution of the random waypoint mobility model for wireless ad hoc networks”. In: *IEEE Transactions on Mobile Computing* 2.3 (2003), pp. 257–269. ISSN: 1536-1233. DOI: `10.1109/TMC.2003.1233531`.

[Bet01] C. Bettstetter. “Mobility modeling in wireless networks: categorization, smooth movement, and border effects”. In: *ACM SIGMOBILE Mobile Computing and Communications Review* 5.3 (2001), pp. 55–66.

[Bet+04] C. Bettstetter, H. Hartenstein, and X. Pérez-Costa. “Stochastic properties of the random waypoint mobility model”. In: *Wireless Networks* 10.5 (2004), pp. 555–567.

[BK14] D. Bharadia and S. Katti. “Full Duplex MIMO Radios”. In: *Proc. 11th USENIX Symp. Netw. Syst. Design Implement.* Seattle, WA, USA, 2014, pp. 359–372. ISBN: 978-1-931971-09-6.

[Bha+13] D. Bharadia, E. McMilin, and S. Katti. “Full Duplex Radios”. In: *Proc. ACM SIGCOMM Conf.* Hong Kong, China, 2013, pp. 375–386. ISBN: 978-1-4503-2056-6.

[BS98] K. Bowman and L. Shenton. “Estimation: Method of Moments”. In: *Encyclopedia of Statistical Sciences* (1998).

[Bra+14] B. Branco, F. Ganhão, L. Irio, L. Bernardo, R. Dinis, R. Oliveira, P. Amaral, and P. Pinto. “SC-FDE femtocell energy saving using IB-DFE Interference Cancellation techniques”. In: *2014 21st International Conference on Telecommunications (ICT)*. 2014, pp. 328–332. DOI: `10.1109/ICT.2014.6845133`.

[Cac+11] A. S. Cacciapuoti, I. F. Akyildiz, and L. Paura. “Primary-user mobility impact on spectrum sensing in Cognitive Radio networks”. In: *2011 IEEE 22nd International Symposium on Personal, Indoor and Mobile Radio Communications*. 2011, pp. 451–456. DOI: `10.1109/PIMRC.2011.6140001`.

[Cac+13] A. S. Cacciapuoti, I. F. Akyildiz, and L. Paura. “Optimal Primary-User Mobility Aware Spectrum Sensing Design for Cognitive Radio Networks”. In: *IEEE Journal on Selected Areas in Communications* 31.11 (2013), pp. 2161–2172. ISSN: 0733-8716. DOI: `10.1109/JSAC.2013.131102`.

[CH01] C. C. Chan and S. V. Hanly. “Calculating the outage probability in a CDMA network with spatial Poisson traffic”. In: *IEEE Transactions on Vehicular Technology* 50.1 (2001), pp. 183–204. ISSN: 0018-9545. DOI: `10.1109/25.917918`.

[Cha+17] C. Chau, I. W. H. Ho, Z. Situ, S. C. Liew, and J. Zhang. "Effective Static and Adaptive Carrier Sensing for Dense Wireless CSMA Networks". In: *IEEE Transactions on Mobile Computing* 16.2 (2017), pp. 355–366. ISSN: 1536-1233. DOI: 10.1109/TMC.2016.2557780.

[Che16] Y. Chen. "Energy-Harvesting AF Relaying in the Presence of Interference and Nakagami-*m* Fading". In: *IEEE Transactions on Wireless Communications* 15.2 (2016), pp. 1008–1017. ISSN: 1536-1276. DOI: :10.1109/TWC.2015.2481393.

[CS01] K.-H. Chiang and N. Shenoy. "A random walk mobility model for location management in wireless networks". In: *12th IEEE International Symposium on Personal, Indoor and Mobile Radio Communications. PIMRC 2001. Proceedings (Cat. No.01TH8598).* Vol. 2. 2001, E–E. DOI: 10.1109/PIMRC.2001.965260.

[Cho+10a] J. I. Choi, M. Jain, K. Srinivasan, P. Levis, and S. Katti. "Achieving Single Channel, Full Duplex Wireless Communication". In: *Proc. 16th Annu. Int. Conf. Mobile Comput. Netw.* Chicago, Illinois, USA, 2010, pp. 1–12. ISBN: 978-1-4503-0181-7.

[Cho+10b] J. I. Choi, M. Jain, K. Srinivasan, P. Levis, and S. Katti. "Achieving Single Channel, Full Duplex Wireless Communication". In: *Proceedings of the Sixteenth Annual International Conference on Mobile Computing and Networking*. MobiCom '10. Chicago, Illinois, USA: ACM, 2010, pp. 1–12. ISBN: 978-1-4503-0181-7. DOI: 10.1145/1859995.1859997. URL: http://doi.acm.org/10.1145/1859995.1859997.

[CSM13] Y.-S. Choi and H. Shirani-Mehr. "Simultaneous Transmission and Reception: Algorithm, Design and System Level Performance". In: *IEEE Transactions on Wireless Communications* 12.12 (2013), pp. 5992–6010. ISSN: 1536-1276. DOI: 10.1109/TWC.2013.101713.121152.

[Cos+08a] D. B. da Costa, M. D. Yacoub, and J. C. S. Santos Filho. "An Improved Closed-Form Approximation to the Sum of Arbitrary Nakagami- *m* Variates". In: *IEEE Transactions on Vehicular Technology* 57.6 (2008), pp. 3854–3858. ISSN: 0018-9545. DOI: 10.1109/TVT.2008.918725.

[Cos+08b] D. B. da Costa, M. D. Yacoub, and J. C. S. Santos Filho. "Highly Accurate Closed-Form Approximations to the Sum of α-μ Variates and Applications". In: *IEEE Transactions on Wireless Communications* 7.9 (2008), pp. 3301–3306. ISSN: 1536-1276. DOI: 10.1109/TWC.2008.070336.

[Day+12] B. Day, A. Margetts, D. Bliss, and P. Schniter. "Full-Duplex MIMO Relaying: Achievable Rates Under Limited Dynamic Range". In: *IEEE Journal on Selected Areas in Communications* 30.8 (2012), pp. 1541–1553. ISSN: 0733-8716. DOI: 10.1109/JSAC.2012.120921.

[Deb+14] B. Debaillie, D. van den Broek, C. Lavín, B. van Liempd, E. A. M. Klumperink, C. Palacios, J. Craninckx, B. Nauta, and A. Pärssinen. "Analog/RF Solutions Enabling Compact Full-Duplex Radios". In: *IEEE Journal on Selected Areas in Communications* 32.9 (2014), pp. 1662–1673. ISSN: 0733-8716. DOI: `10.1109/JSAC.2014.2330171`.

[Din+17] Z. Ding, S. Xing, F. Yan, Z. Li, and L. Shen. "Impact of adaptive carrier-sensing range on the performance of dense wireless networks". In: *2017 9th International Conference on Wireless Communications and Signal Processing (WCSP)*. 2017, pp. 1–6. DOI: `10.1109/WCSP.2017.8170993`.

[Dua12] M. Duarte. "Full-duplex Wireless: Design, Implementation and Characterization". PhD thesis. Houston, TX, USA, 2012.

[DS10] M. Duarte and A. Sabharwal. "Full-duplex wireless communications using off-the-shelf radios: Feasibility and first results". In: *2010 Conference Record of the Forty Fourth Asilomar Conference on Signals, Systems and Computers*. 2010, pp. 1558–1562. DOI: `10.1109/ACSSC.2010.5757799`.

[Dua+12] M. Duarte, C. Dick, and A. Sabharwal. "Experiment-Driven Characterization of Full-Duplex Wireless Systems". In: *IEEE Transactions on Wireless Communications* 11.12 (2012), pp. 4296–4307. ISSN: 1536-1276. DOI: `10.1109/TWC.2012.102612.111278`.

[Dua+14] M. Duarte, A. Sabharwal, V. Aggarwal, R. Jana, K. Ramakrishnan, C. Rice, and N. Shankaranarayanan. "Design and Characterization of a Full-Duplex Multiantenna System for WiFi Networks". In: *IEEE Transactions on Vehicular Technology* 63.3 (2014), pp. 1160–1177. ISSN: 0018-9545. DOI: `:10.1109/TVT.2013.2284712`.

[ElS+13] H. ElSawy, E. Hossain, and M. Haenggi. "Stochastic Geometry for Modeling, Analysis, and Design of Multi-Tier and Cognitive Cellular Wireless Networks: A Survey". In: *IEEE Communications Surveys Tutorials* 15.3 (2013), pp. 996–1019. ISSN: 1553-877X. DOI: `10.1109/SURV.2013.052213.00000`.

[EE99] J. S. Evans and D. Everitt. "On the teletraffic capacity of CDMA cellular networks". In: *IEEE Transactions on Vehicular Technology* 48.1 (1999), pp. 153–165. ISSN: 0018-9545. DOI: `10.1109/25.740079`.

[Eve+14] E. Everett, A. Sahai, and A. Sabharwal. "Passive Self-Interference Suppression for Full-Duplex Infrastructure Nodes". In: *IEEE Trans. Wireless Commun.* 13.2 (2014), pp. 680–694. ISSN: 1536-1276. DOI: `10.1109/TWC.2013.010214.130226`.

[Fli+15] I. Flint, X. Lu, N. Privault, D. Niyato, and P. Wang. "Performance Analysis of Ambient RF Energy Harvesting with Repulsive Point Process Modeling". In: *IEEE Transactions on Wireless Communications* 14.10 (2015), pp. 5402–5416. ISSN: 1536-1276. DOI: `10.1109/TWC.2015.2437973`.

[For+14] E. Foroozanfard, O. Franek, A. Tatomirescu, E. Tsakalaki, E. de Carvalho, and G. Pedersen. “Full-duplex MIMO system based on antenna cancellation technique”. In: *Electronics Lett.* 50.16 (2014), pp. 1116–1117. ISSN: 0013-5194. DOI: `10.1049/el.2014.1650`.

[Fur+14a] A. Furtado, L. Irio, R. Oliveira, L. Bernardo, and R. Dinis. “Characterization of the Spatial False Alarm effect in Cognitive Radio Networks”. In: *2014 23rd International Conference on Computer Communication and Networks (ICCCN)*. 2014, pp. 1–8. DOI: `10.1109/ICCCN.2014.6911742`.

[Fur+14b] A. Furtado, M. Luís, L. Irio, R. Oliveira, L. Bernardo, and R. Dinis. “Detection of licensed users’ activity in a random access ultra wideband cognitive system”. In: *2014 IEEE International Conference on Ultra-WideBand (ICUWB)*. 2014, pp. 91–95. DOI: `10.1109/ICUWB.2014.6958957`.

[Fur+16] A. Furtado, L. Irio, R. Oliveira, L. Bernardo, and R. Dinis. “Spectrum Sensing Performance in Cognitive Radio Networks With Multiple Primary Users”. In: *IEEE Transactions on Vehicular Technology* 65.3 (2016), pp. 1564–1574. ISSN: 0018-9545. DOI: `10.1109/TVT.2015.2406254`.

[GH08] R. K. Ganti and M. Haenggi. “Interference in ad hoc networks with general motion-invariant node distributions”. In: *2008 IEEE International Symposium on Information Theory*. 2008, pp. 1–5. DOI: `10.1109/ISIT.2008.4594936`.

[GS08] A. Ghasemi and E. S. Sousa. “Interference Aggregation in Spectrum-Sensing Cognitive Wireless Networks”. In: *IEEE Journal of Selected Topics in Signal Processing* 2.1 (2008), pp. 41–56. ISSN: 1932-4553. DOI: `10.1109/JSTSP.2007.914897`.

[GN08] S. Goel and R. Negi. “Guaranteeing Secrecy using Artificial Noise”. In: *IEEE Transactions on Wireless Communications* 7.6 (2008), pp. 2180–2189. ISSN: 1536-1276. DOI: `10.1109/TWC.2008.060848`.

[Gol05] A. Goldsmith. *Wireless communications*. Cambridge university press, 2005.

[GH14] Z. Gong and M. Haenggi. “Interference and Outage in Mobile Random Networks: Expectation, Distribution, and Correlation”. In: *IEEE Transactions on Mobile Computing* 13.2 (2014), pp. 337–349. ISSN: 1536-1233. DOI: `10.1109/TMC.2012.253`.

[Goy+15] S. Goyal, P. Liu, S. S. Panwar, R. A. Difazio, R. Yang, and E. Bala. “Full duplex cellular systems: will doubling interference prevent doubling capacity?” In: *IEEE Communications Magazine* 53.5 (2015), pp. 121–127. ISSN: 0163-6804. DOI: `10.1109/MCOM.2015.7105650`.

[Gre+79] J. Greenwood, J. Landwehr, N. Matalas, and J. Wallis. “Probability weighted moments: definition and relation to parameters of several distributions expressable in inverse form”. In: *Water Resources Research* 15.5 (1979), pp. 1049–1054.

[GA15] Y. Gu and S. Aïssa. “RF-Based Energy Harvesting in Decode-and-Forward Relaying Systems: Ergodic and Outage Capacities”. In: *IEEE Transactions on Wireless Communications* 14.11 (2015), pp. 6425–6434. ISSN: 1536-1276. DOI: `10.1109/TWC.2015.2453418`.

[Gul+12] K. Gulati, R. K. Ganti, J. G. Andrews, B. L. Evans, and S. Srikanteswara. “Characterizing Decentralized Wireless Networks with Temporal Correlation in the Low Outage Regime”. In: *IEEE Transactions on Wireless Communications* 11.9 (2012), pp. 3112–3125. ISSN: 1536-1276. DOI: `10.1109/TWC.2012.072512.111003`.

[HG09] M. Haenggi and R. K. Ganti. *Interference in large wireless networks*. Now Publishers Inc, 2009.

[Han+11] W. Han, J. Li, Q. Liu, and L. Zhao. “Spatial False Alarms in Cognitive Radio”. In: *IEEE Communications Letters* 15.5 (2011), pp. 518–520. ISSN: 1089-7798. DOI: `10.1109/LCOMM.2011.031411.102473`.

[Han+13] W. Han, J. Li, Z. Li, J. Si, and Y. Zhang. “Spatial False Alarm in Cognitive Radio Network”. In: *IEEE Transactions on Signal Processing* 61.6 (2013), pp. 1375–1388. ISSN: 1053-587X. DOI: `10.1109/TSP.2012.2236833`.

[HA07] A. Hasan and J. G. Andrews. “The Guard Zone in Wireless Ad hoc Networks”. In: *IEEE Transactions on Wireless Communications* 6.3 (2007), pp. 897–906. ISSN: 1536-1276. DOI: `10.1109/TWC.2007.04793`.

[Hea+13] R. W. Heath, M. Kountouris, and T. Bai. “Modeling Heterogeneous Network Interference Using Poisson Point Processes”. In: *IEEE Transactions on Signal Processing* 61.16 (2013), pp. 4114–4126. ISSN: 1053-587X. DOI: `10.1109/TSP.2013.2262679`.

[Hei+15] M. Heino, D. Korpi, T. Huusari, E. Antonio-Rodriguez, S. Venkatasubramanian, T. Riihonen, L. Anttila, C. Icheln, K. Haneda, R. Wichman, and M. Valkama. “Recent advances in antenna design and interference cancellation algorithms for in-band full duplex relays”. In: *IEEE Communications Magazine* 53.5 (2015), pp. 91–101. ISSN: 0163-6804. DOI: `10.1109/MCOM.2015.7105647`.

[Hos+85] J. Hosking, J. Wallis, and E. Wood. “Estimation of the generalized extreme-value distribution by the method of probability-weighted moments”. In: *Technometrics* 27.3 (1985), pp. 251–261.

[HB05] J. Hu and N. C. Beaulieu. “Accurate simple closed-form approximations to Rayleigh sum distributions and densities”. In: *IEEE Communications Letters* 9.2 (2005), pp. 109–111. ISSN: 1089-7798. DOI: `10.1109/LCOMM.2005.02003`.

[Ina+09] H. Inaltekin, M. Chiang, H. V. Poor, and S. B. Wicker. “On unbounded path-loss models: effects of singularity on wireless network performance”. In: *IEEE Journal on Selected Areas in Communications* 27.7 (2009), pp. 1078–1092. ISSN: 0733-8716. DOI: `10.1109/JSAC.2009.090906`.

[IO15a] L. Irio and R. Oliveira. “Interference estimation in wireless mobile random waypoint networks”. In: *2015 23rd Telecommunications Forum Telfor (TELFOR)*. 2015, pp. 161–164. DOI: `10.1109/TELFOR.2015.7377438`.

[IO15b] L. Irio and R. Oliveira. “Sensing capacity of Cognitive Radio Mobile Ad Hoc Networks”. In: *2015 IEEE Wireless Communications and Networking Conference (WCNC)*. 2015, pp. 1737–1741. DOI: `10.1109/WCNC.2015.7127730`.

[IO18] L. Irio and R. Oliveira. “On the Impact of Fading on Residual Self-Interference Power of In-Band Full-Duplex Wireless Systems”. In: *Proc. Int. Wireless Commun. Mobile Comput. Conf. (IWCMC)*. Limassol, Cyprus, 2018, pp. 142–146. DOI: `10.1109/IWCMC.2018.8450357`.

[IO19a] L. Irio and R. Oliveira. “Distribution of the Residual Self-Interference Power in In-Band Full-Duplex Wireless Systems”. In: *IEEE Access* 7 (2019), pp. 57516–57526. ISSN: 2169-3536. DOI: `10.1109/ACCESS.2019.2914002`.

[IO19b] L. Irio and R. Oliveira. “Modeling the Interference Caused to a LoRaWAN Gateway Due to Uplink Transmissions”. In: *2019 11th International Conference on Ubiquitous and Future Networks (ICUFN)*. 2019.

[Iri+15a] L. Irio, R. Oliveira, and L. Bernardo. “Aggregate Interference in Random Waypoint Mobile Networks”. In: *IEEE Communications Letters* 19.6 (2015), pp. 1021–1024. ISSN: 1089-7798. DOI: `10.1109/LCOMM.2015.2416718`.

[Iri+15b] L. Irio, A. Furtado, R. Oliveira, L. Bernardo, and R. Dinis. “Path Loss Interference in Mobile Random Waypoint Networks”. In: *Proceedings of European Wireless 2015; 21th European Wireless Conference*. 2015, pp. 1–5.

[Iri+16] L. Irio, D. Oliveira, and R. Oliveira. “Interference Estimation in Wireless Mobile Random Waypoint Networks”. In: *Telfor Journal* 8.2 (2016), pp. 93–97. ISSN: 2334-9905. DOI: `10.5937/telfor1602093I`.

[Iri+18a] L. Irio, R. Oliveira, and L. Oliveira. “Characterization of the residual self-interference power in full-duplex wireless systems”. In: *Proc. IEEE Int. Symp. Circuits Syst.* Florence, Italy, 2018, pp. 1–5. DOI: `10.1109/ISCAS.2018.8351260`.

[Iri+18b] L. Irio, A. Furtado, R. Oliveira, L. Bernardo, and R. Dinis. “Interference Characterization in Random Waypoint Mobile Networks”. In: *IEEE Transactions on Wireless Communications* 17.11 (2018), pp. 7340–7351. ISSN: 1536-1276. DOI: `10.1109/TWC.2018.2866426`.

[Iri+19a] L. Irio, R. Oliveira, and D. B. da Costa. “Highly Accurate Approaches for the Interference Modeling in Coexisting Wireless Networks”. In: *IEEE Communications Letters* (2019), pp. 1–1. ISSN: 1089-7798. DOI: `10.1109/LCOMM.2019.2924887`.

[Iri+19b] L. Irio, R. Oliveira, and D. B. da Costa. “Interference Analysis for Secondary Coexistence in Licensed Networks”. In: *2019 IEEE Global Communications Conference (GLOBECOM)*. 2019.

[IO16] L. Irio and R. Oliveira. “Real-Time Estimation of the Interference in Random Waypoint Mobile Networks”. In: *Technological Innovation for Cyber-Physical Systems*. Cham: Springer International Publishing, 2016, pp. 302–311. ISBN: 978-3-319-31165-4.

[IO17] L. Irio and R. Oliveira. “Impact of Mobility in Spectrum Sensing Capacity”. In: *Cognitive Radio Oriented Wireless Networks*. Cham: Springer International Publishing, 2017, pp. 162–172. ISBN: 978-3-319-76207-4.

[Jab+98] B. Jabbari, Y. Zhou, and F. Hillier. “Random walk modeling of mobility in wireless networks”. In: *VTC ’98. 48th IEEE Vehicular Technology Conference. Pathway to Global Wireless Revolution (Cat. No.98CH36151)*. Vol. 1. 1998, 639–643 vol.1. DOI: 10.1109/VETEC.1998.686653.

[Jam+15] I. Jamil, L. Cariou, and J. Hélard. “Efficient MAC protocols optimization for future high density WLANS”. In: *2015 IEEE Wireless Communications and Networking Conference (WCNC)*. 2015, pp. 1054–1059. DOI: 10.1109/WCNC.2015.7127615.

[JM96] D. Johnson and D. Maltz. “Dynamic Source Routing in Ad Hoc Wireless Networks”. In: *Mobile Computing*. Ed. by Imielinski and Korth. Vol. 353. Kluwer Academic Publishers, 1996. URL: citeseer.ist.psu.edu/johnson96dynamic.html.

[JS06] June Hwang and Seong-Lyun Kim. “A cross-layer optimization of IEEE 802.11 MAC for wireless multihop networks”. In: *IEEE Communications Letters* 10.7 (2006), pp. 531–533. ISSN: 1089-7798. DOI: 10.1109/LCOM.2006.224410.

[Kar+06] G. K. Karagiannidis, N. C. Sagias, and T. A. Tsiftsis. “Closed-form statistics for the sum of squared Nakagami-m variates and its applications”. In: *IEEE Transactions on Communications* 54.8 (2006), pp. 1353–1359. ISSN: 0090-6778. DOI: 10.1109/TCOMM.2006.878812.

[Kim+15] D. Kim, H. Lee, and D. Hong. “A Survey of In-Band Full-Duplex Transmission: From the Perspective of PHY and MAC Layers”. In: *IEEE Communications Surveys Tutorials* 17.4 (2015), pp. 2017–2046. ISSN: 1553-877X. DOI: 10.1109/COMST.2015.2403614.

[Kim+14] D. Kim, S. Park, H. Ju, and D. Hong. “Transmission Capacity of Full-Duplex-Based Two-Way Ad Hoc Networks With ARQ Protocol”. In: *IEEE Transactions on Vehicular Technology* 63.7 (2014), pp. 3167–3183. ISSN: 0018-9545. DOI: 10.1109/TVT.2014.2302013.

[Kin93] J. F. C. Kingman. *Poisson processes*. Wiley Online Library, 1993.

[Kor+14a] D. Korpi, T. Riihonen, V. Syrjälä, L. Anttila, M. Valkama, and R. Wichman. "Full-Duplex Transceiver System Calculations: Analysis of ADC and Linearity Challenges". In: *IEEE Transactions on Wireless Communications* 13.7 (2014), pp. 3821–3836. ISSN: 1536-1276. DOI: `10.1109/TWC.2014.2315213`.

[Kor+14b] D. Korpi, L. Anttila, V. Syrjälä, and M. Valkama. "Widely linear digital self-interference cancellation in direct-conversion full-duplex transceiver". In: *IEEE Journal on Selected Areas in Communications* 32.9 (2014), pp. 1674–1687. ISSN: 0733-8716. DOI: `10.1109/JSAC.2014.2330093`.

[Lan+79] J. Landwehr, N. Matalas, and J. Wallis. "Probability weighted moments compared with some traditional techniques in estimating Gumbel parameters and quantiles". In: *Water Resources Research* 15.5 (1979), pp. 1055–1064.

[Lau+14] L. Laughlin, M. Beach, K. Morris, and J. Haine. "Optimum Single Antenna Full Duplex Using Hybrid Junctions". In: *IEEE Journal on Selected Areas in Communications* 32.9 (2014), pp. 1653–1661. ISSN: 0733-8716. DOI: `10.1109/JSAC.2014.2330191`.

[Lee13] J. Lee. "Self-Interference Cancelation Using Phase Rotation in Full-Duplex Wireless". In: *IEEE Transactions on Vehicular Technology* 62.9 (2013), pp. 4421–4429. ISSN: 0018-9545. DOI: `10.1109/TVT.2013.2264064`.

[LA08] W. Lee and I. F. Akyildiz. "Optimal spectrum sensing framework for cognitive radio networks". In: *IEEE Transactions on Wireless Communications* 7.10 (2008), pp. 3845–3857. ISSN: 1536-1276. DOI: `10.1109/T-WC.2008.070391`.

[Li+18] R. Li, A. Masmoudi, and T. Le-Ngoc. "Self-Interference Cancellation With Non-linearity and Phase-Noise Suppression in Full-Duplex Systems". In: *IEEE Transactions on Vehicular Technology* 67.3 (2018), pp. 2118–2129. ISSN: 0018-9545. DOI: `10.1109/TVT.2017.2754489`.

[LM14] S. Li and R. Murch. "An Investigation Into Baseband Techniques for Single-Channel Full-Duplex Wireless Communication Systems". In: *IEEE Transactions on Wireless Communications* 13.9 (2014), pp. 4794–4806. ISSN: 1536-1276. DOI: `10.1109/TWC.2014.2341569`.

[Li+17] X. Li, C. Tepedelenlioglu, and H. Senol. "Channel Estimation for Residual Self-Interference in Full-Duplex Amplify-and-Forward Two-Way Relays". In: *IEEE Transactions on Wireless Communications* 16.8 (2017), pp. 4970–4983. ISSN: 1536-1276. DOI: `10.1109/TWC.2017.2704123`.

[Lic+10] H. S. Lichte, S. Valentin, and H. Karl. "Expected interference in wireless networks with geometric path loss: a closed-form approximation". In: *IEEE Communications Letters* 14.2 (2010), pp. 130–132. ISSN: 1089-7798. DOI: `10.1109/LCOMM.2010.02.091863`.

[Ma+09] H. Ma, R. Vijayakumar, S. Roy, and J. Zhu. "Optimizing 802.11 Wireless Mesh Networks Based on Physical Carrier Sensing". In: *IEEE/ACM Transactions on Networking* 17.5 (2009), pp. 1550–1563. ISSN: 1063-6692. DOI: 10.1109/TNET.2008.2009443.

[MP02] R. H. Mahadevappa and J. G. Proakis. "Mitigating multiple access interference and intersymbol interference in uncoded CDMA systems with chip-level interleaving". In: *IEEE Transactions on Wireless Communications* 1.4 (2002), pp. 781–792. ISSN: 1536-1276. DOI: 10.1109/TWC.2002.804163.

[MLN16] A. Masmoudi and T. Le-Ngoc. "A Maximum-Likelihood Channel Estimator for Self-Interference Cancelation in Full-Duplex Systems". In: *IEEE Transactions on Vehicular Technology* 65.7 (2016), pp. 5122–5132. ISSN: 0018-9545. DOI: 10.1109/TVT.2015.2461006.

[ML16] A. Masmoudi and T. Le-Ngoc. "Self-Interference Cancellation Limits in Full-Duplex Communication Systems". In: *Proc. IEEE Global Telecomm. Conf.* Washington, DC, USA, 2016, pp. 1–6. DOI: 10.1109/GLOCOM.2016.7842258.

[Mat82] A. M. Mathai. "Storage capacity of a dam with gamma type inputs". In: *Annals of the Institute of Statistical Mathematics* 34.1 (1982), pp. 591–597.

[Meh+07] N. B. Mehta, J. Wu, A. F. Molisch, and J. Zhang. "Approximating a Sum of Random Variables with a Lognormal". In: *IEEE Transactions on Wireless Communications* 6.7 (2007), pp. 2690–2699. ISSN: 1536-1276. DOI: 10.1109/TWC.2007.051000.

[Men+05] R. Menon, R. M. Buehrer, and J. H. Reed. "Outage probability based comparison of underlay and overlay spectrum sharing techniques". In: *First IEEE International Symposium on New Frontiers in Dynamic Spectrum Access Networks, 2005. DySPAN 2005.* 2005, pp. 101–109. DOI: 10.1109/DYSPAN.2005.1542623.

[Mos85] P. G. Moschopoulos. "The distribution of the sum of independent gamma random variables". In: *Annals of the Institute of Statistical Mathematics* 37.1 (1985), pp. 541–544.

[Mur+11] G. Muraleedharan, C. G. Soares, and C. Lucas. "Characteristic and Moment Generating Functions of Generalised Extreme Value Distribution (GEV)". In: *Sea Level Rise, Coastal Engineering, Shorelines and Tides, Nova Science Publishers* (2011), pp. 269–276.

[Nac+08] J. Nachtigall, A. Zubow, and J. Redlich. "The Impact of Adjacent Channel Interference in Multi-Radio Systems using IEEE 802.11". In: *2008 International Wireless Communications and Mobile Computing Conference*. 2008, pp. 874–881. DOI: 10.1109/IWCMC.2008.151.

[Nad+17] A. Nadh, J. Samuel, A. Sharma, S. Aniruddhan, and R. K. Ganti. "A Taylor Series Approximation of Self-Interference Channel in Full-Duplex Radios". In: *IEEE Transactions on Wireless Communications* 16.7 (2017), pp. 4304–4316. ISSN: 1536-1276. DOI: `10.1109/TWC.2017.2696938`.

[Nak60] M. Nakagami. "The m-distribution-A general formula of intensity distribution of rapid fading". In: *Statistical Method of Radio Propagation* (1960).

[Nav+05] R. Navid, T. H. Lee, and R. W. Dutton. "Minimum achievable phase noise of RC oscillators". In: *IEEE Journal of Solid-State Circuits* 40.3 (2005), pp. 630–637. ISSN: 0018-9200. DOI: `10.1109/JSSC.2005.843591`.

[Pah+02] K. Pahlavan, X. Li, and J. P. Makela. "Indoor geolocation science and technology". In: *IEEE Communications Magazine* 40.2 (2002), pp. 112–118. ISSN: 0163-6804. DOI: `10.1109/35.983917`.

[PP02] A. Papoulis and S. U. Pillai. *Probability, random variables, and stochastic processes*. Tata McGraw-Hill Education, 2002.

[PW07] P. C. Pinto and M. Z. Win. "Spectral characterization of wireless networks". In: *IEEE Wireless Communications* 14.6 (2007), pp. 27–31. ISSN: 1536-1284. DOI: `10.1109/MWC.2007.4407224`.

[PW10] P. C. Pinto and M. Z. Win. "Communication in a Poisson Field of Interferers–Part I: Interference Distribution and Error Probability". In: *IEEE Transactions on Wireless Communications* 9.7 (2010), pp. 2176–2186. ISSN: 1536-1276. DOI: `10.1109/TWC.2010.07.060438`.

[Pin+09] P. C. Pinto, A. Giorgetti, M. Z. Win, and M. Chiani. "A stochastic geometry approach to coexistence in heterogeneous wireless networks". In: *IEEE Journal on Selected Areas in Communications* 27.7 (2009), pp. 1268–1282. ISSN: 0733-8716. DOI: `10.1109/JSAC.2009.090922`.

[PS07] J. G. Proakis and M. Salehi. *Digital Communications*. 5th. McGraw-Hill, 2007.

[Pur+09] P. Pursula, M. Kiviranta, and H. Seppa. "UHF RFID Reader With Reflected Power Canceller". In: *IEEE Microwave and Wireless Components Letters* 19.1 (2009), pp. 48–50. ISSN: 1531-1309. DOI: `10.1109/LMWC.2008.2008607`.

[Rab+11] A. Rabbachin, T. Q. S. Quek, H. Shin, and M. Z. Win. "Cognitive Network Interference". In: *IEEE Journal on Selected Areas in Communications* 29.2 (2011), pp. 480–493. ISSN: 0733-8716. DOI: `10.1109/JSAC.2011.110219`.

[Rap01] T. Rappaport. *Wireless Communications: Principles and Practice*. 2nd. Upper Saddle River, NJ, USA: Prentice Hall PTR, 2001. ISBN: 0130422320.

[Rib+18] A. Ribeiro, L. Irio, L. Oliveira, and R. Oliveira. "The impact of phase-noise on the communication system receivers". In: *2018 International Young Engineers Forum (YEF-ECE)*. 2018, pp. 55–60. DOI: `10.1109/YEF-ECE.2018.8368939`.

[Rii+11] T. Riihonen, S. Werner, and R. Wichman. “Mitigation of Loopback Self-Interference in Full-Duplex MIMO Relays”. In: *IEEE Transactions on Signal Processing* 59.12 (2011), pp. 5983–5993. ISSN: 1053-587X. DOI: :10.1109/TSP.2011.2164910.

[Sah+12] A. Sahai, G. Patel, C. Dick, and A. Sabharwal. “Understanding the impact of phase noise on active cancellation in wireless full-duplex”. In: *Proc. Asilomar Conf. Signals, Syst. Comput.* 2012, pp. 29–33. DOI: 10.1109/ACSSC.2012.6488952.

[Sah+13] A. Sahai, G. Patel, C. Dick, and A. Sabharwal. “On the Impact of Phase Noise on Active Cancelation in Wireless Full-Duplex”. In: *IEEE Transactions on Vehicular Technology* 62.9 (2013), pp. 4494–4510. ISSN: 0018-9545. DOI: 10.1109/TVT.2013.2266359.

[Sak+14] M. Sakai, H. Lin, and K. Yamashita. “Adaptive cancellation of self-interference in full-duplex wireless with transmitter IQ imbalance”. In: *Proc. IEEE GLOBECOM*. 2014, pp. 3220–3224. DOI: 10.1109/GLOCOM.2014.7037302.

[Sam+17] L. Samara, M. Mokhtar, O. Özdemir, R. Hamila, and T. Khattab. “Residual Self-Interference Analysis for Full-Duplex OFDM Transceivers Under Phase Noise and I/Q Imbalance”. In: *IEEE Transactions on Communications* 21.2 (2017), pp. 314–317. ISSN: 1089-7798. DOI: 10.1109/LCOMM.2016.2620431.

[Sho+17] A. Shojaeifard, K. Wong, M. D. Renzo, G. Zheng, K. A. Hamdi, and J. Tang. “Self-Interference in Full-Duplex Multi-User MIMO Channels”. In: *IEEE Transactions on Communications* 21.4 (2017), pp. 841–844. ISSN: 1089-7798. DOI: 10.1109/LCOMM.2016.2647709.

[SA05] M. K. Simon and M.-S. Alouini. *Digital Communication over Fading Channels*. Vol. 95. John Wiley & Sons, 2005.

[SS90] E. S. Sousa and J. A. Silvester. “Optimum transmission ranges in a direct-sequence spread-spectrum multihop packet radio network”. In: *IEEE Journal on Selected Areas in Communications* 8.5 (1990), pp. 762–771. ISSN: 0733-8716. DOI: 10.1109/49.56383.

[SH07] S. Srinivasa and M. Haenggi. “Modeling interference in finite uniformly random networks”. In: *International Workshop on Information Theory for Sensor Networks (WITS’07)*. 2007, pp. 1–12.

[Syr+14] V. Syrjala, M. Valkama, L. Anttila, T. Riihonen, and D. Korpi. “Analysis of Oscillator Phase-Noise Effects on Self-Interference Cancellation in Full-Duplex OFDM Radio Transceivers”. In: *IEEE Transactions on Wireless Communications* 13.6 (2014), pp. 2977–2990. ISSN: 1536-1276. DOI: 10.1109/TWC.2014.041014.131171.

[TM14] C. Thorpe and L. Murphy. “A Survey of Adaptive Carrier Sensing Mechanisms for IEEE 802.11 Wireless Networks”. In: *IEEE Communications Surveys Tutorials* 16.3 (2014), pp. 1266–1293. ISSN: 1553-877X. DOI: `10.1109/SURV.2014.031814.00177`.

[Vu+09] M. Vu, N. Devroye, and V. Tarokh. “On the primary exclusive region of cognitive networks”. In: *IEEE Transactions on Wireless Communications* 8.7 (2009), pp. 3380–3385. ISSN: 1536-1276. DOI: `10.1109/TWC.2009.080454`.

[Wan+15] L. Wang, F. Tian, T. Svensson, D. Feng, M. Song, and S. Li. “Exploiting full duplex for device-to-device communications in heterogeneous networks”. In: *IEEE Communications Magazine* 53.5 (2015), pp. 146–152. ISSN: 0163-6804. DOI: `10.1109/MCOM.2015.7105653`.

[Win+09] M. Z. Win, P. C. Pinto, and L. A. Shepp. “A Mathematical Theory of Network Interference and Its Applications”. In: *Proceedings of the IEEE* 97.2 (2009), pp. 205–230. ISSN: 0018-9219. DOI: `10.1109/JPROC.2008.2008764`.

[Wul+00] D. Wulich, N. Dinur, and A. Glinowiecki. “Level clipped high-order OFDM”. In: *IEEE Transactions on Communications* 48.6 (2000), pp. 928–930. ISSN: 0090-6778. DOI: `10.1109/26.848551`.

[XZ14] X. Xie and X. Zhang. “Does full-duplex double the capacity of wireless networks?” In: *Proc. IEEE INFOCOM*. Toronto, ON, Canada, 2014, pp. 253–261. DOI: `10.1109/INFOCOM.2014.6847946`.

[YP03] X. Yang and A. P. Petropulu. “Co-channel interference modeling and analysis in a Poisson field of interferers in wireless communications”. In: *IEEE Transactions on Signal Processing* 51.1 (2003), pp. 64–76. ISSN: 1053-587X. DOI: `10.1109/TSP.2002.806591`.

[Yar+08] S. Yarkan, A. Maaref, K. H. Teo, and H. Arslan. “Impact of Mobility on the Behavior of Interference in Cellular Wireless Networks”. In: *IEEE GLOBECOM 2008 - 2008 IEEE Global Telecommunications Conference*. 2008, pp. 1–5. DOI: `10.1109/GLOCOM.2008.ECP.457`.

[Zha+13] X. Zhang, L. Wu, Y. Zhang, and D. K. Sung. “Interference dynamics in MANETs with a random direction node mobility model”. In: *2013 IEEE Wireless Communications and Networking Conference (WCNC)*. 2013, pp. 3788–3793. DOI: `10.1109/WCNC.2013.6555178`.

[Zha+15] Z. Zhang, X. Chai, K. Long, A. V. Vasilakos, and L. Hanzo. “Full duplex techniques for 5G networks: self-interference cancellation, protocol design, and relay selection”. In: *IEEE Communications Magazine* 53.5 (2015), pp. 128–137. ISSN: 0163-6804. DOI: `10.1109/MCOM.2015.7105651`.

APPENDIX A

POISSON APPROXIMATION

This appendix identifies the conditions required to use the Poisson distribution to approximate the number of nodes located within an annulus l.

We start considering an annulus $l \in \{1,...,L\}$ with area $A_l = \pi\left((R_o^l)^2 - (R_i^l)^2\right)$, where n mobile nodes can be located. The number of nodes located within the annulus l is represented by the random variable X_l. P_l represents the probability of a node being located within the annulus. The Poisson Theorem (PT) in [PP02, p. 113] states that the Poisson distribution may be used as an approximation of the Binomial distribution, when $P_l \to 0$ and $n \to \infty$, such that the mean value $\lambda_l A_l = nP_l$ remains constant.

Representing the probability of having k nodes located in the annulus l through the Binomial distribution,

$$P(X_l = k) = \binom{n}{k} P_l^k (1 - P_l)^{n-k}, \tag{A.1}$$

it can be rewritten as

$$P(X_l = k) = \frac{n!}{(n-k)!k!} P_l^k (1 - P_l)^{n-k}. \tag{A.2}$$

As $n \to \infty$, we know that

$$\frac{n!}{(n-k)!k!} = \frac{n(n-1)...(n-k-1)}{k!} \approx \frac{n^k}{k!}. \tag{A.3}$$

Assuming that the average number of nodes located in the annulus is given by $\lambda_l A_l = nP_l$, and replacing (A.3) in (A.1), we have

$$P(X_l = k) = \frac{(\lambda_l A_l)^k}{k!} (1 - P_l)^{\frac{(\lambda_l A_l)}{P_l} - k}. \tag{A.4}$$

According to PT conditions, $P_l \to 0$. Knowing that

$$\lim_{P_l \to 0} (1 - P_l)^{\frac{1}{P_l}} = e^{-1},$$

(A.4) can be rewritten as follows,

$$P(X_l = k) = \frac{(\lambda_l A_l)^k}{k!} e^{-(\lambda_l A_l)}. \tag{A.5}$$

Assuming the PT, the Binomial distribution describing the number of nodes within the annulus area may be approximated by the Poisson distribution in (A.5) (with $\lambda_l A_l = nP_l$). We highlight that in the limit conditions (i.e., $n \rightarrow \infty$ and $P_l \rightarrow 0$), the Poisson distribution can be derived from the binomial one. However, in practical scenarios, the PT conditions must be observed in an approximated way. In our work we have considered a fixed number of nodes (n), and the division of the simulation area in multiple annuli benefits the condition $P_l \rightarrow 0$.